ABSTRACT

Title of Dissertation: Image Reconstruction for Hyperpolarized Carbon-13
Metabolic Magnetic Resonance Imaging with Iterative
Methods

Minjie Zhu, Doctor of Philosophy, 2024

Dissertation directed by: Professor Behtash Babadi
Department of Electrical and Computer Engineering

Magnetic resonance imaging (MRI) with hyperpolarized carbon-13 (13C) agents is an emerging in vivo medical imaging technique. 13C MRI gives a series of images that show the evolution of the injected substrate and its metabolic products in the imaging volume, which leads to various medical applications including monitoring tumor progression and post-treatment response in both animal models and clinical trials. This dissertation focuses on the application of novel iterative image reconstruction methods for 13C MRI that aim to improve image quality and temporal resolution.

One of the challenges for the existing 13C MRI reconstruction method is the difficulty in quantification of lower intensity metabolites due to noise and overlapping peaks in the aliased spectrum. In the first part of the dissertation, a model-based iterative reconstruction method is proposed to overcome such difficulty. The proposed method utilizes prior knowledge of the properties of the metabolites in the imaging volume, including off-resonance frequency, T2* decay constants, and the image acquisition trajectory in spatial and frequency domain. Metabolic images are reconstructed through solving the linear equation between acquired signal and images with least square error estimation. The reconstruction results on in vivo imaging data sets demonstrate that the proposed method can separate two overlapped peaks in an aliased spectrum while the conventional method fails.

Another challenge for 13C MRI is to reconstruct metabolic images from under-sampled acquisitions. Due to the short lifetime of the injected substrate and the physical limitation of the MRI scanner, only a few temporal frames can be acquired for 13C MRI with one injection. Under-sampling in the image acquisition can provide more frames, but certain reconstruction methods are required to remove the artifacts from direct reconstruction on the under-sampled data. In the second part of the dissertation, a customized low-rank plus sparse (L+S) reconstruction method is proposed to produce artifact-free images from under-sampled data. Digital phantom simulations are performed to evaluate the optimal reconstruction parameters. Simulation with digital phantom and in vivo mouse imaging on 2D and 3D dynamic imaging data demonstrate the effectiveness in acceleration without introducing image artifacts using the proposed reconstruction method.

In the third part of the dissertation, we present a preclinical application of 13C MRI to study brain metabolism and identify the source of metabolic products based on the metabolic images derived. In vivo metabolic imaging with different flow-suppression levels was performed on rats in the brain region. Results show that metabolic product, lactate, has no significant dependence on the level of suppression while the substrate pyruvate is strongly dependent. This supports our hypothesis that lactate seen in metabolic images is generated in the brain. Additional high-resolution metabolic imaging was performed to show different signal distributions for pyruvate and lactate clearly. Our proposed L+S reconstruction method was applied to the dynamic image data to reduce the background noise. The derived dynamic images show distinct dynamics for pyruvate and lactate, further supporting our hypothesis.

IMAGE RECONSTRUCTION FOR HYPERPOLARIZED CARBON-13 METABOLIC MAGNETIC RESONANCE IMAGING WITH ITERATIVE METHODS

by

Minjie Zhu

Dissertation submitted to the Faculty of the Graduate School of the
University of Maryland, College Park, in partial fulfillment
of the requirements for the degree of
Doctor of Philosophy
2024

Advisory Committee:
Professor Behtash Babadi, Chair
Professor Dirk Mayer
Professor Jonathan Simon
Professor Gang Qu
Professor Luiz Pessoa

Acknowledgements

I would like to express my sincere gratitude to Professor Dirk Mayer for the guidance and encouragement on my Ph.D. study during the past seven years. He brought me into the field of hyperpolarized carbon-13 metabolic magnetic resonance imaging. Without his patient and meticulous mentorship, I would not be able to accomplish my achievements today.

In addition, I would like to thank Professor Behtash Babadi, for serving the role as academic advisor and dissertation committee chair. I would also like to thank Professor Jonathan Simon, Professor Gang Qu and Professor Luiz Pessoa for the time and efforts as my dissertation committee members. My sincere gratitude and condolence to two great mentors during my Ph.D. study, Professor Christopher Davis and Professor Rao Gullapalli, who passed away in 2023.

Moreover, I would like to express my appreciation for the help, support, and companionship I have been receiving from lab members at CMIT: Dr. Maninder Singh, Dr. Aditya Jhajharia, Mr. Joshua Rogers and Dr. Abubakr Eldirdiri. I have had a great time working with them.

Lastly, I would like to thank my family, especially my mother, Zhiling Zhu, for her love and encouragement, which made me go through the most difficult time during my Ph.D. study.

Table of Contents

Chapter 1 : Introduction

Magnetic resonance imaging (MRI) is a prevalent non-invasive medical imaging modality. It has been widely applied to a wide variety of medical diagnostics and scientific studies including cancer, neurological disease, cardiovascular disease etc. Majority of the current MRI studies use MR signal from proton nucleus (^{1}H), which provides high signal-to-noise ratio (SNR) due to the high abundance of ^{1}H nuclei in vivo.

Hyperpolarized ^{13}C MRI is an emerging metabolic imaging modality that uses MR signal from carbon-13 nucleus (^{13}C), an isotope with 1.1% natural abundance. It involves injection of ^{13}C labelled imaging substrates into the imaging subjects to monitor specific enzyme-catalyzed biochemical reactions and quantify metabolic conversion of key metabolites in biological tissues through the ^{13}C labelling[1–4]. By far, [1-^{13}C]pyruvate is the most well studied and commonly used ^{13}C imaging substrates. Unlike ^{1}H MRI, ^{13}C MRI has limited raw MR signal due to the low gyromagnetic ratio (25% of ^{1}H) and low concentration of the injected imaging substrates (<0.1 mol/L), proposing a technical challenge to perform in vivo ^{13}C imaging. MR signal can be enhanced through hyperpolarization of the imaging substrates, a process that changes the ratio of spins contributing to MR signal. An emerging hyperpolarization method named as dissolution dynamic nuclear polarization (dDNP) has been demonstrated to increase MR signal from ^{13}C nucleus by 10,000 folds or more. The enhanced MR signal through hyperpolarization has limited lifetime, irreversibly decaying to thermal equilibrium level on the order of tens of seconds. As a result, hyperpolarized ^{13}C imaging must be performed within several minutes, necessitating the development of accelerated imaging methods. In addition, the reconstructed metabolic images must include multiple metabolites differentiated based on their chemical shift, further exacerbating the challenges of fast imaging and require improved image reconstruction methods for quantification of metabolites with low SNR.

This dissertation focuses on the application of novel image reconstruction methods for hyperpolarized ^{13}C metabolic imaging. Given the constraints including relatively short imaging time and low MR signal, the overall goals of the research are to improve image quality and accelerate image acquisition to achieve higher temporal resolution for dynamic imaging.

Chapter 2 outlines the background information for this dissertation, describing the existing methods for hyperpolarized ^{13}C imaging and pointing out the imaging considerations that necessitate the novel methods. Chapter 3, 4 and 5 present two iterative reconstruction frameworks. The model-based iterative reconstruction framework in Chapter 3 gives better quantification of low intensity metabolite and reduces the image artifacts for metabolites with overlapping peaks in an aliased spectrum. The L+S reconstruction framework in Chapter 4 and 5 accelerates image acquisition through exploiting the low rank and sparse properties of dynamic imaging. Chapter 6 presents a preclinical application of hyperpolarized ^{13}C imaging to study brain metabolism and identify the source of metabolic products based on the metabolic images derived.

Chapter 2 : Background

This chapter reviews the relevant background of MRI and hyperpolarized ^{13}C metabolic imaging.

2. 1 Fundamentals of MRI and spectroscopy

2. 1. 1 Nuclear spins

Nuclear spins

Nuclei with odd number of protons and/or neutrons, such as ^{1}H and ^{13}C, possess a nuclear spin angular momentum, each possessing a microscopic magnetic field $\vec{\mu}$. Without external magnetic field, these spins are randomly oriented and the macroscopic magnetization $\vec{M}$ is zero[6], as shown in Figure 2-1 (a).

Spins in main field B_0

With static external magnetic field $\overrightarrow{B_0}$, these spins are aligned in parallel(lower energy state) or anti-parallel (higher energy state) in the direction of $\overrightarrow{B_0}$ (by convention, the z-direction) [Figure 2-1 (b)]. Thermal energy gives rise to a small fractional difference between the population of parallel spins (n_+) and the population of anti-parallel spins (n_-), with the ratio dependent on ΔE, the energy difference between the two spin states[7]:

$$\frac{\mathrm{n}_-}{\mathrm{n}_+} = \mathrm{e}^{-\Delta E/kT} [Eq. 2.1].$$

k is Boltzmann constant and T is absolute temperature of the environment. The fractional difference between the spin states creates a non-zero collective magnetization $\vec{M}$. Such magnetization exhibits resonance at Larmor frequency $\omega = \gamma B_0$, with γ as the gyromagnetic ratio, a constant dependent on the type of nuclei.

Polarization

Magnitude of $\vec{M}$ is proportional to the difference of parallel and anti-parallel spins normalized by the total number of spins, characterized by polarization P. At room temperature (T), the thermal equilibrium for polarization is low (approximately $9.9 \cdot 10^{-6}$ for ^{1}H and $2.5 \cdot 10^{-6}$ for ^{13}C). Without extra process, MR imaging of ^{1}H nuclei is easily achieved due to the abundance of proton-containing molecules (mostly water) in biological tissues. However, it is not achievable for MR imaging of metabolites labelled with ^{13}C nuclei at thermal equilibrium level due to their relatively low concentration in vivo.

Dissolution dynamic nuclear polarization (dDNP) is a method to enhance polarization level of ^{13}C labelled metabolites by 10,000-fold or more compared with the thermal equilibrium level [Figure 2-1 (c)]. This amplified hyperpolarized signal has limited lifetime, decaying to the thermal equilibrium with a spin-lattice relaxation constant T_1. A large group of ^{13}C labeled substrates including [1-^{13}C]pyruvate have T_1 values ranging up to 80 seconds, providing a feasible time window for imaging of metabolic conversions in vivo[2,5].

The dDNP process is carried out externally in a specialized instrument, the polarizer, prior to ^{13}C imaging applications. In the first step of dDNP, the metabolite to be polarized and used for imaging, often referred as substrate compound, is mixed with electron paramagnetic agent (EPA), serving as the source of unpaired electrons. A buffer solution with dissolved ethylene-diamine-tetraacetic acid (EDTA) is prepared as well for dissolution of the substrate. In the second step. mixture is packaged in a vial compatible with the polarizer and is subsequently inserted into the polarizer. The amount of mixture and buffer is calculated so that the corresponding substrate solution is at designated concentration. In the third step, the vial is submerged into the liquid helium in the sample cup of the polarizer, where the local temperature is around 1 Kelvin, and the surrounding magnetic field is around 5 Tesla. At that low temperature, polarization of electrons is close to 100%. The mixture is irradiated by a microwave source so that the polarization of the electrons can be gradually transferred to the ^{13}C nuclei in substrate, demonstrated in Figure 2-1(d). Typically, it takes more than two hours for the transfer process to achieve maximal polarization of the ^{13}C substrate, up to 50%. In the last step, vial is lifted out of the sample cup and heated buffer solution close to 100°C is rapidly discharged into the vial to produce the polarized substrate solution for the ^{13}C imaging application right afterwards. A schematic of the GE SpinLab polarizer[8] (Research Circle Technology, Niskayuna, NY), the polarizer we used for the imaging experiments in Chapter 4-6, is provided in Figure 2-1(e).

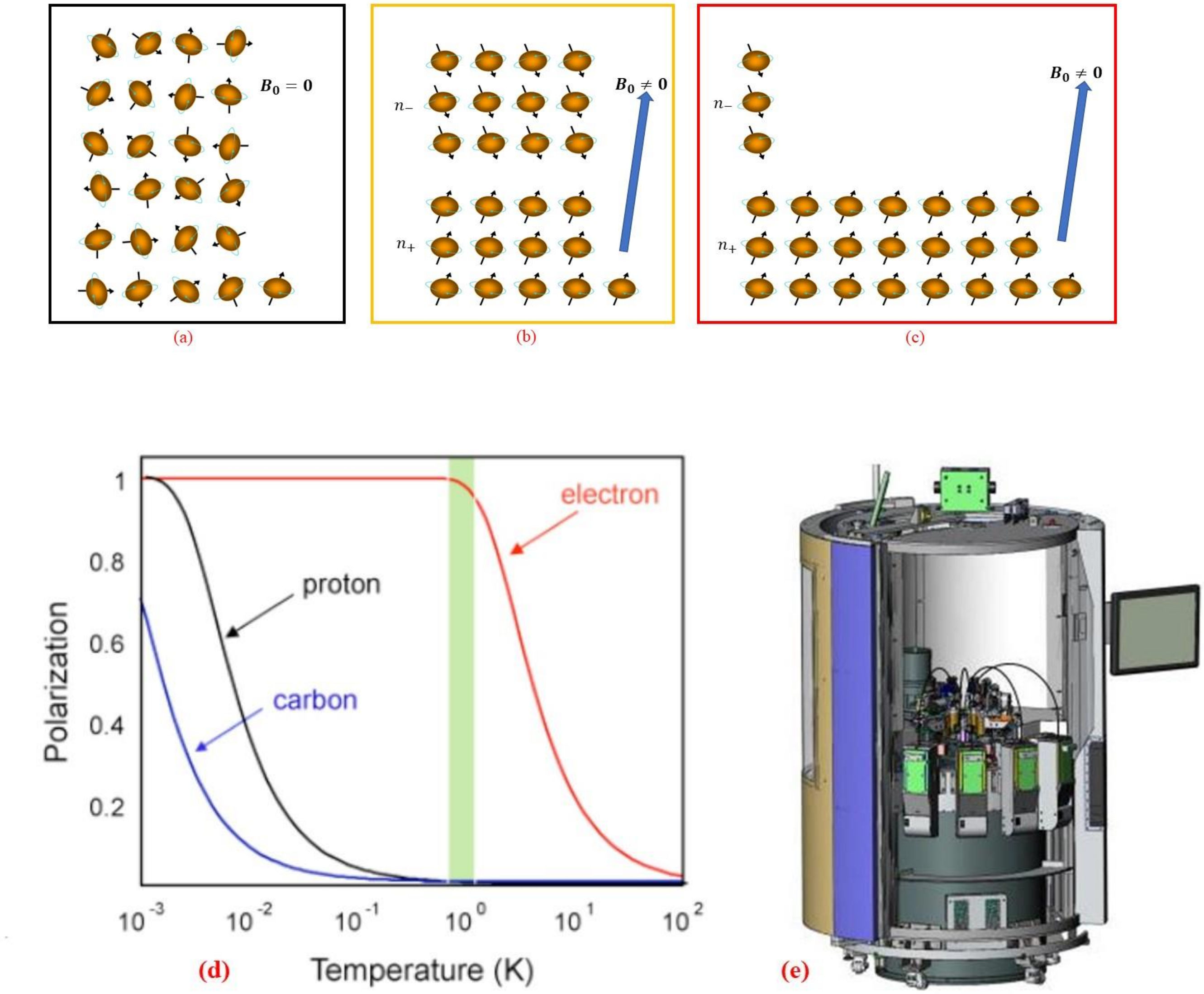

Figure 2-1 **(a)** spins without B_0 **(b)** spins with B_0 in thermal equilibrium state **(c)** Spins with B_0 in hyperpolarized state **(d)** Illustration of polarization for electrons, proton and carbon as a function of temperature. Green shaded area indicates the temperature range where polarization transfer is most efficient **(e)** Schematic of the SpinLab polarizer

Excitation with radiofrequency field B_1

An oscillating magnetic field B_1 can transfer $\vec{M}$ from longitudinal axis (z axis) into the transverse plane (xy plane) as M_{xy} [Figure 2-2 (b)]. B_1 is induced by a specially designed radio frequency(RF) pulse tuned to a narrow bandwidth centered at the resonant frequency of the spins. M_{xy} precesses in the x-y plane at the resonance frequency and exponentially decays with relaxation constant T_2 as a consequence of spin-spin interactions at the atomic or molecular levels. T_2 is typically in the range of 30-100 milliseconds for ^{13}C metabolites[9] [Figure 2-2 (c)]. In real scenario, small variations in B_0 hastes the decay of $\mathrm{M_{xy}}$. The combined effects are reflected by the effective transverse magnetization decay constant T_2^*. The rotating magnetization $\mathrm{M_{xy}}$ induce electromotive force in the receive coils, forming the free induction decay (FID) as the raw MR signal[6,7]:

$$\mathrm{M_{xy}(t)} = M_0 \cdot e^{-t/T_2}\ e^{-j\omega t} [Eq. 2.2]$$

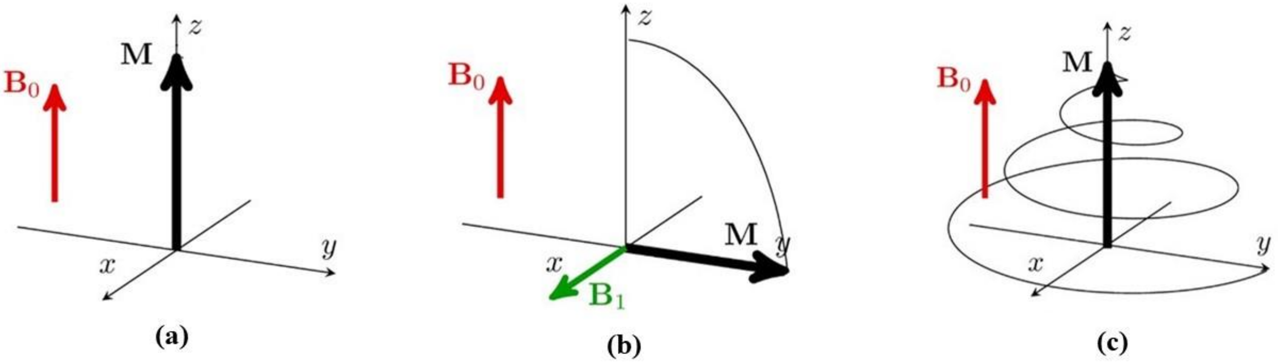

Figure 2-2 **(a)** Magnetization with B_0 **(b)** Magnetization after excitation with B_1 **(c)** Relaxation of $\mathrm{M_{xy}}$ with exponential decay. Image adapted from Martin Uecker[10]

Spatial encoding with gradient field *G*

The static field $\overrightarrow{B_0}$ is superimposed by another magnetic field $\vec{G}$ created by the three gradient coils. $\vec{G}$ has the same direction as $\overrightarrow{B_0}$ but its magnetic field strength varies linearly in space, with linearity G_x, G_y, G_z controlled by the electric current fed into the gradient coils. The magnetic field experienced by the spins at spatial location $r = (x, y, z)$ is $\vec{B}(r) = \vec{z}(B_0 + G_x x + G_y y + G_z z)$. Therefore, the frequency of the spins becomes a function of their spatial location, and this frequency changes instantaneously when the field strength $\vec{B}(r)$ changes. By applying specific gradient waveforms $G(t)$ on the three axes, spatial information can be encoded into phase of $\mathrm{M_{xy}}$ after certain accumulation of differences in the frequency. The set of RF and gradient waveforms applied in certain time order is generally named as pulse sequence.

2. 1. 2 2D imaging and k-space

2D MR image $m(x, y)$ represents the amplitude distribution of the spins in a plane perpendicular to the z axis. The orientation of $x, y\ and\ z$ axis with respect to the physical orientation of the imaging object/MR scanner can arbitrary. By convention, xy represents the 2D imaging plane and z is the axis perpendicular to xy plane . A typical 2D MR imaging pulse sequence is characterized by the following steps:

1) We apply the specific $B_1$and G_z at the same time so that only the spins within the selected slice are excited and flipped into the xy plane, commonly referred as slice-selective excitation.
2) The excited spins with transverse magnetization $\mathrm{M_{xy}}$ precess and generates the FID. We apply certain waveform of $G_x(t)$ and $G_y(t)$ to acquire the spatially dependent information, which fills some part of the raw data to be reconstructed into image $m(x, y)$ later.
3) $\mathrm{M_{xy}}$ decays and remaining transverse magnetization is destroyed by a spoiler gradient. We repeat the previous two steps to acquire next part of the information needed for image reconstruction.

Signal equation

In ideal conditions, the exact magnetization of the spins at location (x, y) after time t of the gradient waveform being applied is:

$$M_{xy}(x, y, \mathrm{t}) = M_0(x, y)e^{-t/T_2}\ \ e^{-j\omega_0 t} \cdot \exp\left(-j\gamma \int_0^t [x \cdot G_x(\tau) + y \cdot G_y(\tau)]\, d\tau\right)[Eq. 2.3]$$

$M_0(x, y)$ represents the initial magnetization after the excitation, directly proportional to $m(x, y)$ without considering other scaling effects. The acquired MR signal $S(t)$ is derived from the contributions of all M_{xy} excited, given by:

$$S(t) = \iint M_{xy}(x, y, \mathrm{t})dxdy = \iint m(x, y)e^{-t/T_2}\ \ e^{-j\omega_0 t} \cdot \exp\left(-j\gamma \int_0^t [x \cdot G_x(\tau) + y \cdot G_y(\tau)]\, d\tau\right)dxdy\ [Eq. 2.4]$$

After demodulating $S(t)$, the carrier frequency $e^{-j\omega_0 t}$ is dropped. T_2 is assumed to be spatially uniform and $S(t)$ is acquired in a period shorter than T_2 so that the weighting due to T_2 decay is negligible at this stage[6].

$$S(t) = \iint m(x,y) \cdot \exp\left(-j\gamma \int_0^t xG_x(\tau)d\tau\right) \cdot \exp\left(-j\gamma \int_0^t yG_y(\tau)d\tau\right) [Eq. 2.5]$$

The received signal $S(t)$ contains information about the spatial distribution of $m(x,y)$ captured in the 2D frequency domain, commonly referred as k-space in MRI. $S(t)$ is sampled along a k-space trajectory $k(t) = [k_x(t), k_y(t)]$ defined by the time integral of the gradient waveform $G_x(t)$ and $G_y(t)$

$$k_x(t) = \frac{\gamma}{2\pi}\int_0^t G_x(\tau)d\tau \qquad k_y(t) = \frac{\gamma}{2\pi}\int_0^t G_y(\tau)d\tau \, [Eq. 2.6]$$

Eventually, $S(t)$ represents the 2D Fourier transform of $m(x,y)$ sampled along a trajectory $[k_x(t), k_y(t)]$

$$S(t) = \iint m(x,y)e^{-j2\pi[k_x(t)x+k_y(t)y]}dxdy = \mathcal{F}_{2D}\{m(x,y)\} \, [Eq. 2.7]$$

Cartesian k-space trajectory.

MR image $m(x,y)$ can be properly reconstructed if the corresponding k-space is sufficiently sampled. The most common trajectory for 2D imaging is rectangular sampling on a Cartesian grid. Simply speaking, data are sampled equidistantly in the 2D k-space, as Figure2-3(d). Hence, image can be directly reconstructed from $S(t)$ with 2D discrete Fourier transform (DFT). In the sequence diagram, for each excitation, a trapezoid with stepwise increment in amplitude is applied on $G_y(t)$, while two trapezoids with different polarity are applied on $G_x(t)$. One line of the k-space is acquired for each readout, and multiple excitations are required to cover the full k-space, somewhat inefficient in terms of acquisition speed. Based on the functional relationship from the Fourier theory, the image spatial resolution δ_x, δ_y and field-of-view (FOV) is related to the k-space sampling periods $\Delta_{k_x}, \Delta_{k_y}$, the widths of the coverage k_{xmax}, k_{ymax}, the ADC sampling interval Δ_t, duration of the trapezoid applied on the gradient coils τ_x, τ_y, and corresponding amplitudes G_{xr}, G_{yi}, G_{yp} as following:

$$\delta_x = \frac{1}{2k_{xmax}} = \frac{2\pi}{\gamma G_{xr}\tau_x}, \; \delta_y = \frac{1}{2k_{ymax}} = \frac{2\pi}{\gamma G_{yp}\tau_y} \; [Eq. 2.8]$$

$$FOV_x = \frac{1}{\Delta_{k_x}} = \frac{2\pi}{\gamma G_{xr}\Delta_t}, \; FOV_y = \frac{1}{\Delta_{k_y}} = \frac{2\pi}{\gamma G_{yi}\tau_y} [Eq. 2.9]$$

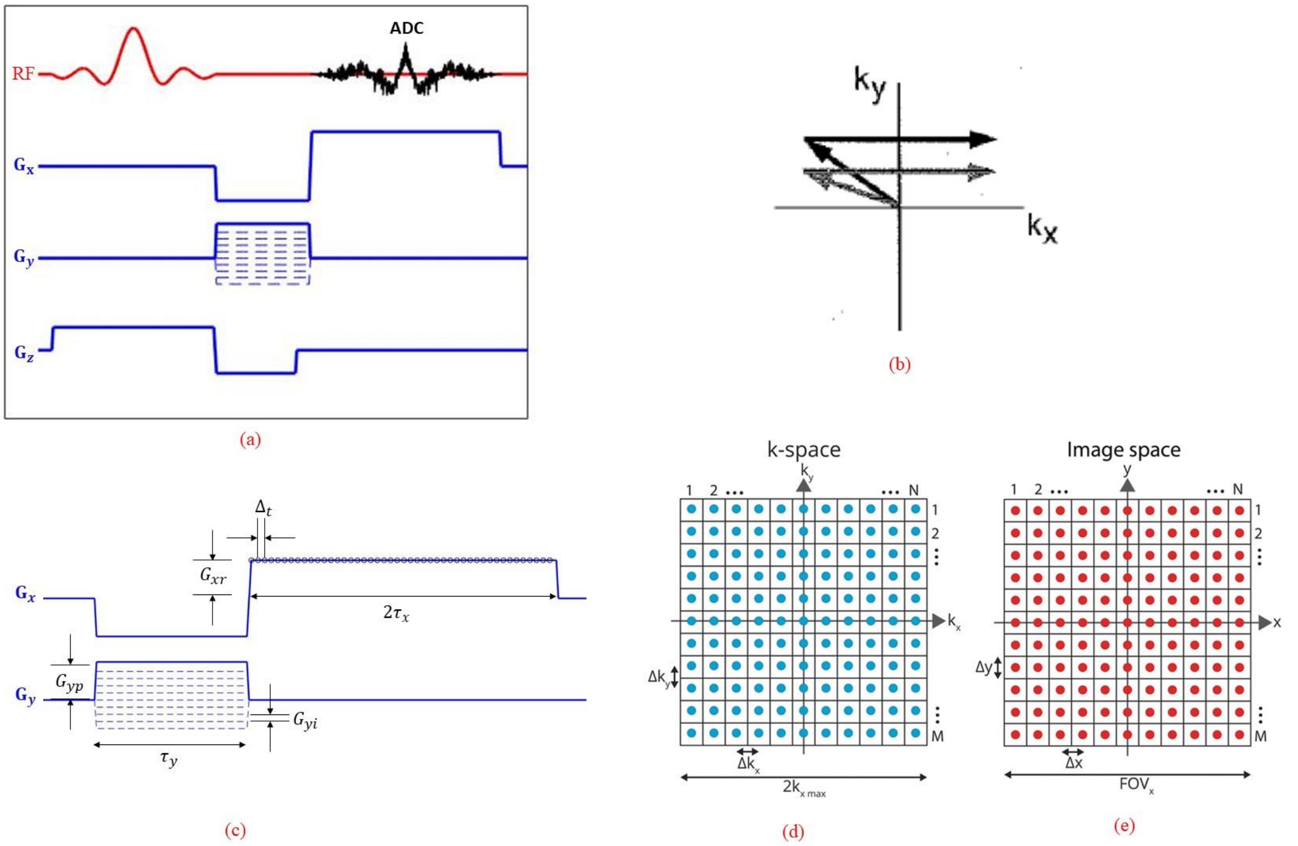

(a) (b) (c) (d) (e)

Figure 2-3 **(a)** Sequence diagram for 2D imaging with Cartesian k-space trajectory. **(b)** Progression of the k-space trajectory. **(c, d and e)** Quantitative relationship between gradient waveform, k-space and image space.

Spiral k-space trajectory

The spiral trajectory travels the 2D k-space from the origin to the edge in spiral shape. In the sequence diagram, sinusoidal waveforms with increasing amplitudes are applied on $G_x(t)$ and $G_y(t)$ simultaneously after excitation. This potentially allows complete acquisition of a fully sampled 2D k-space in a single excitation/readout but may require a rather long duration of $G(t)$, undesirable if it takes more than multiples of T_2 when the signal decays below noise level. In many applications, the alternative way is to split the single spiral into a series of less densely sampled spirals (interleaves) that can be covered using shorter gradient waveform. The k-space sampling periods $\Delta_{k_x}, \Delta_{k_y}$ for spiral trajectory is the distance between adjacent spiral arms, while the coverage k_{xmax}, k_{ymax} is defined similar to the Cartesian case. $m(x, y)$ is reconstructed from spirally sampled k-space via non-uniform discrete Fourier transform (NDFT) with the given information of $k(t)$ [11,12]. The non-uniform discrete Fourier transform can be carried out through several tools, including NUFFT[12], gridding[13] and solving the linear equation with conjugate gradient (CG)[14].

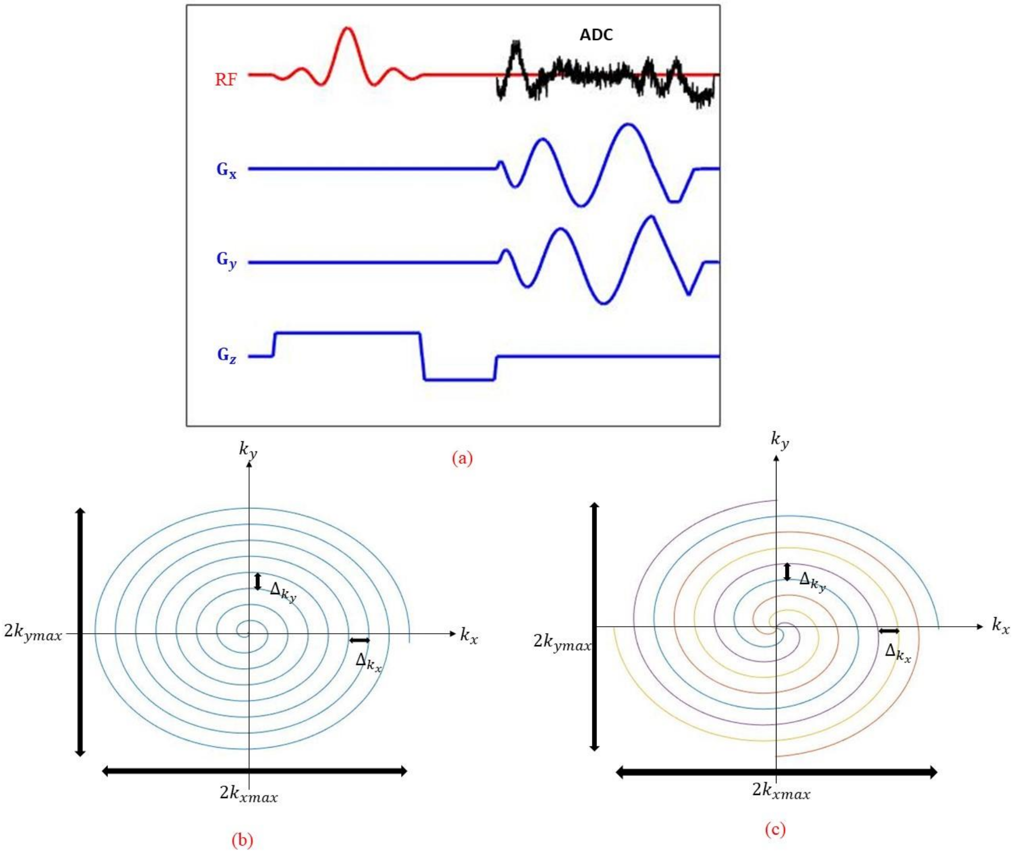

Figure 2-4 **(a)** Sequence diagram for 2D imaging with spiral k-space trajectory. **(b)** Spiral k-space trajectory with one interleaf. **(c)** Spiral k-space trajectory with four interleaves.

2. 1. 3 Chemical shift and spectroscopic imaging

Chemical shift

Signal equation presented above assumed that the resonance frequency ω would be the same for all nuclei with the same gyromagnetic ratio. However, a nucleus may have a small displacement of the resonance frequency due to the shielding created by the surrounding electrons in response to the main magnetic field B_0 [6,7].

$$f = \frac{\omega}{2\pi} = \frac{\gamma}{2\pi} B_0(1+\sigma) = f_0 + \Delta f [Eq. 2.10]$$

This shift in resonance, termed as chemical shift, is specific to the chemical environment and is independent of external magnetic field strength. The shift value σ is specified in terms of parts per million. For example, $\sigma = 183.3$ ppm for the ^{13}C nuclei in [1-^{13}C]lactate and $\sigma = 171.0$ ppm for the ^{13}C nuclei in [1-^{13}C]pyruvate[15]. The 12.3 ppm chemical shift difference between the two metabolites corresponds to a frequency shift of $\Delta f = 391\ Hz$ at $B_0 = 3$ Telsa. Such difference forms the basis for NMR spectroscopy.

Spectroscopy

Assume that a sample with a mixture of M species of metabolites, each having spin density m_i, respective chemical shift frequency Δf_i and decay constant $T_{2,i}^*$. FID signal $S(t)$ acquired by exciting the sample (without any spatial encoding gradient) would be:

$$S(t) = \sum_i m_i e^{-j2\pi\Delta f_i t - t/T_{2,i}^*} \, [Eq. 2.11]$$

The 1D Fourier transform of $S(t)$ forms the NMR spectrum(example as Figure 2-7(a)). The location of each peak in the spectrum represents the chemical shift of the corresponding metabolite, whereas the area under the curve (AUC) represents its spin density.

Chemical Shift Imaging

In chemical shift imaging (CSI), a 3rd dimension is added to the 2D image $m(x, y)$ representing the dependence on the chemical shift frequency Δf relative to the center frequency $f_0 = 2\pi\gamma B_0$. The result image matrix is $m(x, y, f)$, also referred as map of spectra (a spectrum at each (x, y) location). The signal equation including the chemical shift becomes:

$$S(t) = \iiint m(x, y, f) e^{-j2\pi[k_x(t)x + k_y(t)y + ft] - t/T_2^*} df dx dy [Eq. 2.12]$$

Similarly, $S(t)$ represents the 3D Fourier transform of $m(x, y, f)$ sampled along a trajectory $[k_x(t), k_y(t), k_f(t)]$. Here, the trajectory of the 3rd dimension in the extended 3D k-space is $k_f(t) = t$, proceeding linearly in time without any gradient control. $m(x, y, f)$ can be successfully reconstructed given that the 3D k-space is sufficiently filled.

From $m(x, y, f)$, images for each individual metabolite $\rho_i(x, y)$ can be generated by integrating the area under the curve (AUC) on the spectrum at each (x, y) location, referred as peak integral.

Phase-encoded Chemical Shift Imaging

The most straightforward way to fill the 3D k-space is phase-encoded CSI[16,17]. After the selective excitation, phase-encoding waveforms are applied on G_x and G_y to reach corresponding (k_x, k_y) location, followed by data readout without gradient waveform[Figure 2-5(a)]. Each readout gives information along a line parallel to the k_f axis. A fully sampled Cartesian 3D k-space for an N-by-N image in xy plane requires N^2 of these lines [Figure 2-5(b)], necessitating N^2 excitations/measurements, usually time consuming.

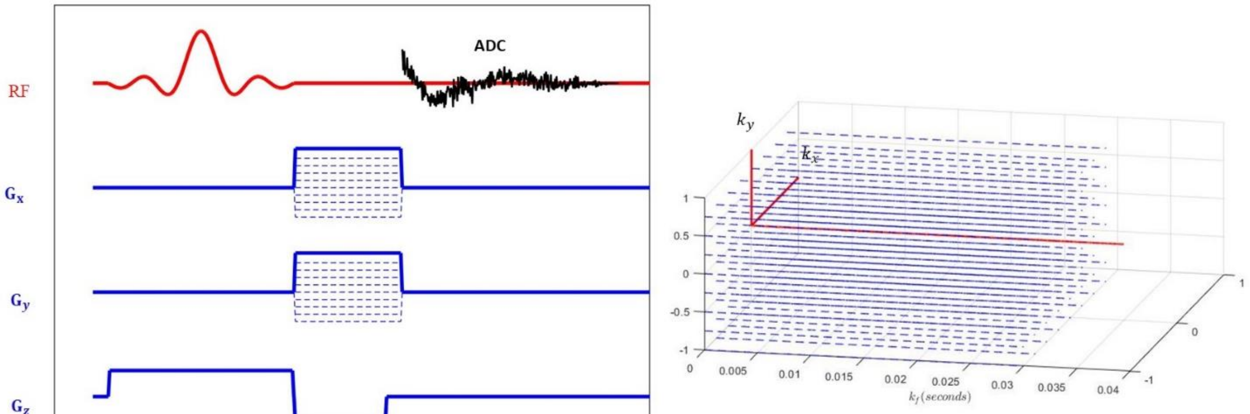

(a)

(b)

Figure 2-5 **(a)** Sequence diagram for phase-encoded CSI **(b)** Cartesian 3D k-space trajectory for phase-encoded CSI.

Spiral Chemical Shift Imaging

Spiral Chemical Shift Imaging (spCSI) utilizes the spiral k-space trajectory in 2D imaging and covers the k_f dimension by repeating the spiral trajectory for N_e times, with a rewinder waveform that sends the k-space trajectory back to origin for each repetition[18] [Figure 2-6]. The nominal FOV in the f axis for $m(x, y, f)$, the spectral width (SW), is determined by the inverse of the time between consecutive spirals: $FOV_f = SW = \frac{1}{\Delta TE}$. Whereas the resolution in the f axis is the inverse of the total readout time: $\delta_f = \frac{1}{N_e * \Delta TE}$.

To include all the peaks for a group of metabolites to be imaged without aliasing, the spectral width should be larger than the maximum frequency shift among all the metabolites. In the most prevalent metabolic imaging with hyperpolarized [1-^{13}C]pyruvate, the injected pyruvate will produce 5 resonances spread over 24 ppm, equivalently a bandwidth around 800Hz at $B_0 = 3$ Tesla, as in Figure 2-7 (a). If such spectrum is fully sampled for the spCSI, it requires $\Delta TE < 1.25ms$. Due to the hardware limitations in gradient coils, it is often not achievable for $G(t)$ to cover the prescribed k-space within such short time. As mentioned in the spiral trajectory in 2D imaging, an interleaved spiral k-space trajectory can shorten ΔTE, but requires multiple excitations.

Conversely, if SW is chosen to be smaller than the full spectral bandwidth (spectral under-sampling), spectral aliasing happens and peaks outside the acquisition bandwidth are aliased into respective positions by multiples of SW. Since only a few metabolites exist in the ^{13}C spectrum and through proper choice of ΔTE, these metabolite peaks can be separated from the under-sampled spectrum, thus reducing the number of interleaves required[19]. Figure 2-7 (b) shows an example of a favorable under-sampled ^{13}C spectrum with $\Delta TE = 3.57ms$, or $SW = 280Hz$.

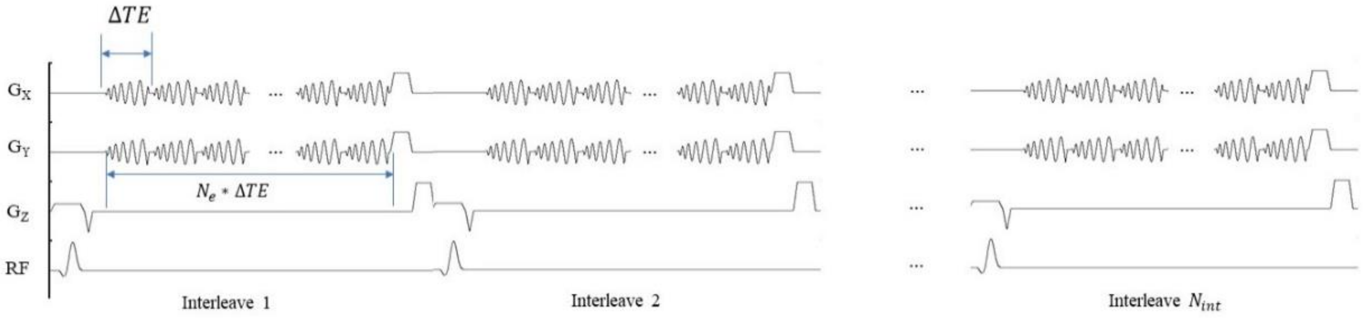

Figure 2-6 Sequence diagram for spCSI with multiple interleaves.

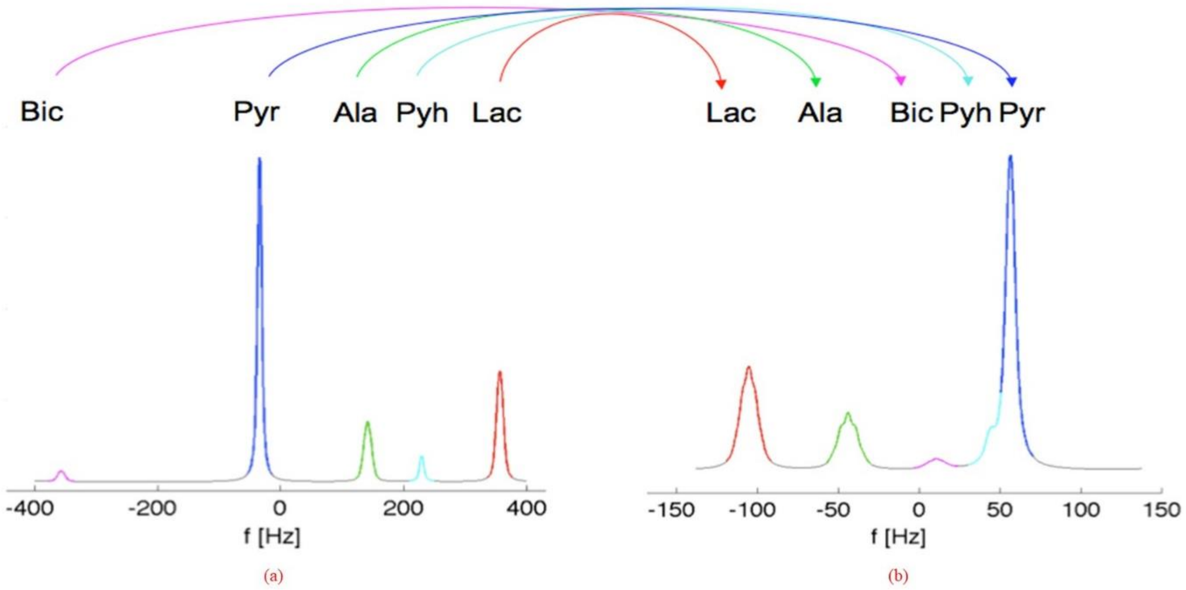

Figure 2-7 **(a)** Fully sampled ^{13}C spectrum for pyruvate (Pyr), lactate (Lac), alanine (Ala), bicarbonate (Bic) and pyruvate hydrate (Pyh), $SW \geq 800\ Hz$ **(b)** Under-sampled ^{13}C spectrum, $SW = 280\ Hz$

Image reconstruction for spCSI

Conventional image reconstruction for the metabolic images $\rho_i(x, y)$ from the spCSI data $S(t)$, referred as CSI reconstruction, takes several steps[20]. Figure 2-8 shows the simplified CSI reconstruction process. In the 1st step of reconstruction, a 1D Fourier transform is performed along time axis t for each sample on the k-space trajectory to form the spectrum. In the case of spectral under-sampling, proper phase correction needs to be applied so that the aliased peaks are correctly represented in the spectral band without aliasing[20]. Following that, NDFT is performed for each spectral bin in the k_{xy} plane to get the spatial information $m(x, y, f)$. In the end, $\rho_i(x, y)$ are generated by integrating the AUC of the respective metabolic peak in the map of spectra.

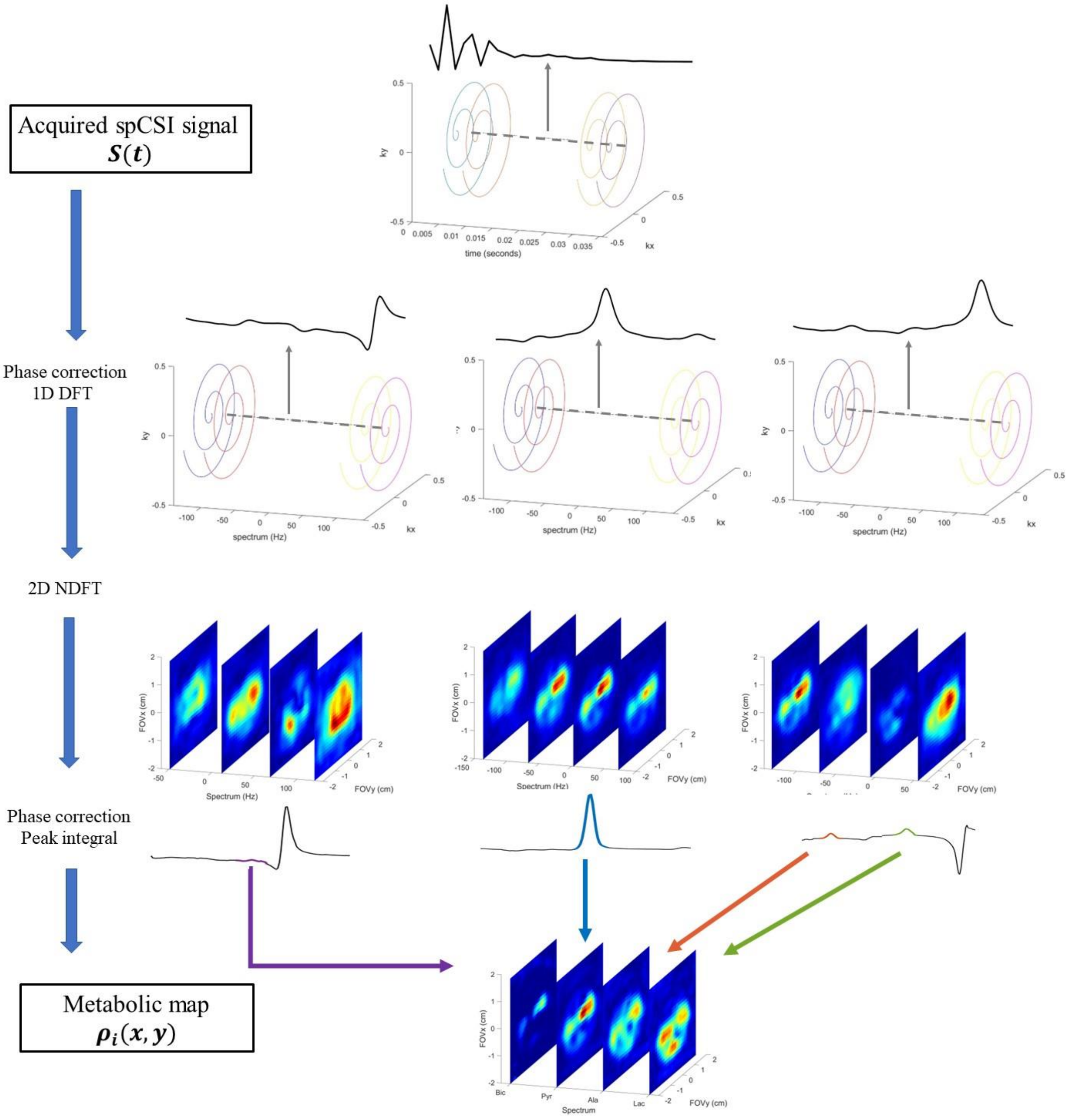

Figure 2-8 Simplified image reconstruction scheme for spiral chemical shift imaging.

2. 2 Fundamentals of hyperpolarized ^{13}C MRI

This section introduces the application of hyperpolarized ^{13}C MRI in recent studies.

2. 2. 1 [1-^{13}C]pyruvate as a metabolic imaging probe

[1-^{13}C]pyruvate is the most widely used ^{13}C metabolic imaging probe because of its key role in multiple cell energy metabolic pathways. Depending on the intracellular environment, the injected [1-^{13}C]pyruvate, often referred as substrate, may undergo three metabolic pathways[21], shown in Figure 2-9. Under anaerobic glycolysis, pyruvate (Pyr) is primarily converted into lactate (Lac) with lactate dehydrogenase (LDH) enzyme. Pyruvate can also be converted into alanine (Ala) if catalyzed by alanine transaminase (ALT) for protein synthesis. Pyruvate transported into mitochondria is converted into carbon dioxide catalyzed by pyruvate dehydrogenase (PDH) along with acetyl-CoA production in the TCA cycle. The carbon dioxide reaches chemical equilibrium with bicarbonate (Bic) with rapid exchange driven by the carbonic anhydrase (CA). Both carbon dioxide and bicarbonate are detectable on the NMR spectrum but are susceptible to noise due to its low concentration. Regardless of the environment, the pyruvate in solution exists the chemical balance with pyruvate hydrate (pyr-H_2O, or Pyh). The chemical equilibrium of pyruvate and pyruvate hydrate depends on the in vivo pH value.

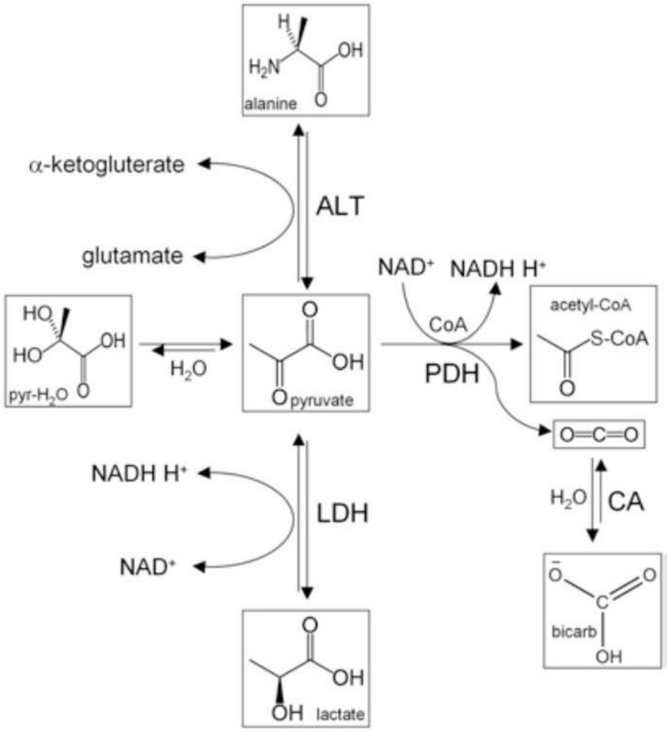

Figure 2-9 Metabolic pathways of pyruvate in cells, adapted from *Chapter 4, Dynamic Hyperpolarized Nuclear Magnetic Resonance*[21]

Monitoring the ratio of the substrate and the product of the above metabolic conversions gives information regarding the cell environment. It has been shown that cancer cells have significantly different metabolism to support proliferation compared with normal cells. One of the most notable characteristics of tumor cells is the Warburg effect[22,23], described in Figure 2-10. In normal and differentiated tissues with sufficient oxygen supply, pyruvate is primarily metabolized via oxidative phosphorylation to generate adenosine triphosphate (ATP). However, in proliferative tissues and tumors, even in the presence of oxygen, pyruvate is preferentially metabolized via aerobic glycolysis. The apparent effect on the metabolic images is the significant higher lactate intensity in the voxels of the tumor cells compared with that of the normal cells[3,24]. Last but not the least, numerous substrates other than [1-^{13}C]pyruvate are also shown to be effective in tracing various metabolic pathways through the hyperpolarized ^{13}C MRI.

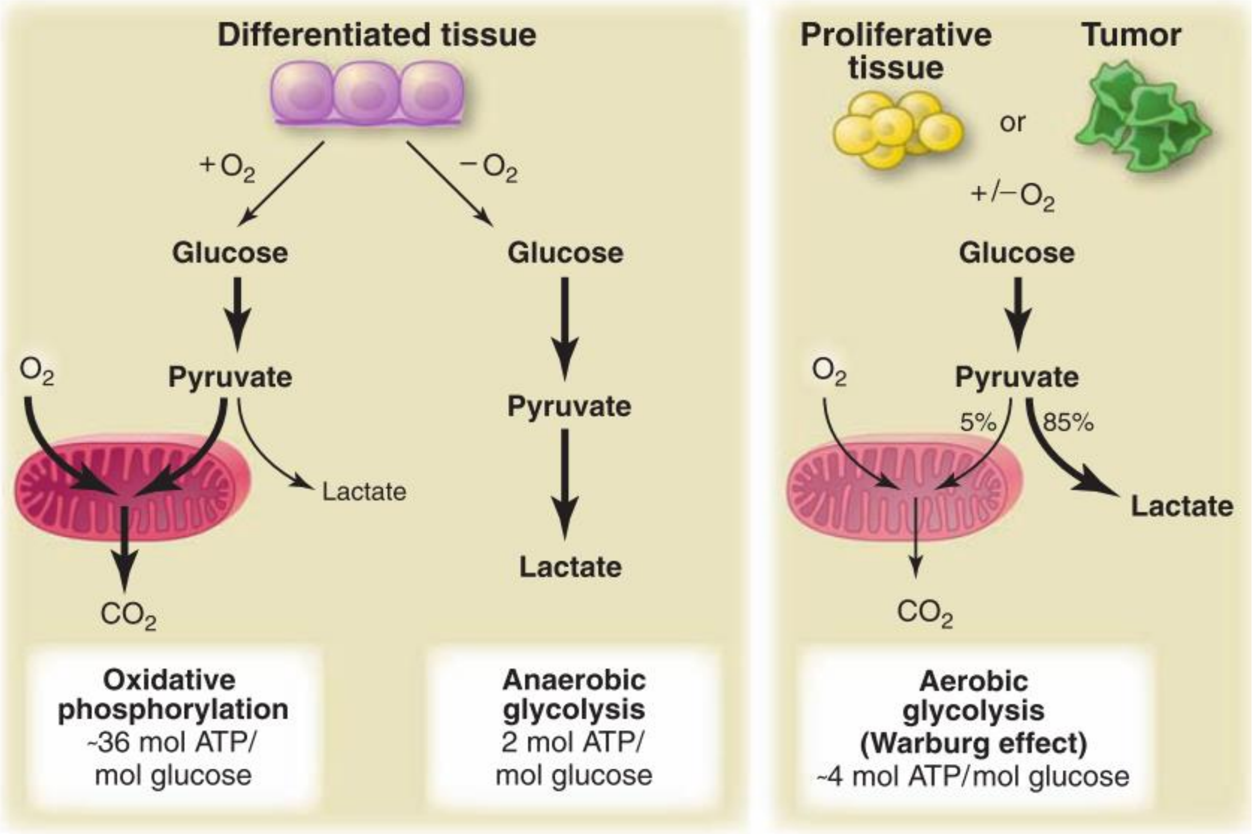

Figure 2-10 Preference of metabolic conversions for normal tissue and tumor (Warburg effect), adapted from Heiden et al[23]

2. 2. 2 Dynamic metabolic imaging with hyperpolarized [1-13C]pyruvate

The metabolic conversion of pyruvate into its products introduced above usually happens continuously after injection of the pyruvate substrate, with distinctive dynamic patterns for different metabolites as well as in different tissues. In many applications, it is desired to capture such dynamic evolvement of metabolic conversion, which helps to build kinetic models of the related metabolic pathways in vivo. To achieve dynamic metabolic imaging, the same spCSI sequence is carried out repeatedly to form a series of metabolic images. The resulting image data would become a 4D matrix $m(x, y, f, T)$ with the 4th dimension as time points. Figure 2-11 illustrates the dynamic metabolic imaging of rat brain with hyperpolarized [1-^{13}C]pyruvate injection[25].

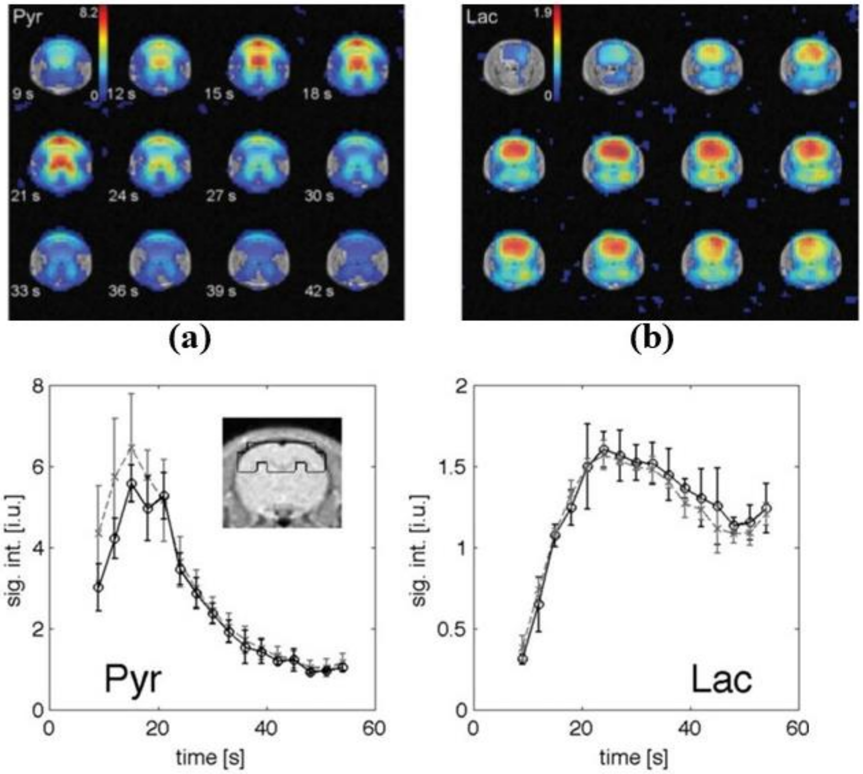

(a) (b)

(c) (d)

Figure 2-11 Rat brain metabolic imaging with hyperpolarized [1-^{13}C]pyruvate injection, adapted from Mayer et al[25]. **(a)** Pyruvate metabolic maps **(b)** Lactate metabolic maps **(c)** Dynamics of mean pyruvate intensity in the brain region (indicated by the circled area in the proton MRI on top right), curve in solid ⊙ represents data from a single animal averaged over 3 injections and curve in dashed × represents data averaged over 3 animals with 3 injections each **(d)** Dynamics of mean lactate intensity in the brain region for the respective data

2. 3 Motivation for research

Difficulty in quantifying metabolites with partially overlapped peaks

As mentioned in Section 2.1.3, spCSI data with spectral under-sampling will be aliased according to the spectral width applied. In certain applications, the aliased peak will partially overlap with another peak in the spectrum, making the quantification of both metabolites difficult in the process of peak integral. A reconstruction method to bypass the peak integral process that generates the metabolic maps directly from acquired spCSI data is desired for such applications.

Insufficient temporal resolution for dynamic imaging

Due to hardware limitations, the acquisition time for one fully sampled spCSI data is rather long, typically 3 seconds for 2D imaging and 12 seconds for 3D imaging. Higher temporal resolution for dynamic imaging is desired for quantification of the metabolite kinetics. Image acceleration can be achieved through under-sampling the k-space acquired during one time point. A reconstruction method to recover the original image from the under-sampled data is necessary for effective image acceleration.

Chapter 3 : Improving Hyperpolarized 13C Spiral Chemical Shift Imaging Using Model-Based Iterative Reconstruction and Prior Knowledge

The following chapter is partially adapted from: "Improving Hyperpolarized 13C Spiral Chemical Shift Imaging Using Model-Based Iterative Reconstruction and Prior Knowledge." Proceeding of International Society of Magnetic Resonance in Medicine, 2019.

3. 1 Introduction

One problem in the reconstruction of metabolic images is the artifacts due to the aliased spectrum where aliased peaks partially overlap. An alternative strategy to determine the metabolic maps $\rho_i(x,y)$ is model-based image reconstruction[26] using the prior knowledge of chemical shift values, k-space trajectory and T_2^*. The model-based image reconstruction formulates the reconstruction problem as a linear equation and solve for the optimized solution of the metabolic maps $\rho_i(x,y)$ directly, without intermediate result $m(x,y,f)$, i.e. no integration of AUC from the map of spectra. It also allows improved reconstruction results by exploiting more prior knowledge, which could not be easily incorporated into CSI reconstruction.

3. 2 Methods

From $[Eq. 2.12]$, reducing the third dimension of $m(x,y,f)$ into M species of metabolic components $\rho_i(x,y)$ with chemical shift frequency Δf_i, the signal equation is expressed as

$$S(t) = \sum_{i}^{M} \iint \rho_i(x,y) e^{-j2\pi[k_x(t)x+k_y(t)y+\Delta f_i t]-t/T_{2,i}^*} dxdy \; [Eq. 3.1]$$

The correspondence between acquired signal $S(t)$ and metabolic maps $\rho_i(x,y)$ can be represented in matrix form as

$$S(t) = E \cdot \rho_i(x,y) + \epsilon \; [Eq. 3.2]$$

E is the encoding matrix comprising all known parameters (i.e., $k_x(t), k_y(t), \Delta f_i, T^*_{2,i}$) that translates the forward signal equation, ϵ is additive noise. The reconstruction of spin density $\rho_i(x, y)$ can be treated as solving linear equations, where ρ_i is the unknown to be solved and the noise ϵ is the error to be minimized.

$$\hat{\rho} = argmin \; \|y - E \; \cdot \rho\|_2^2 \; [Eq. 3.3]$$

The closed-form solution for the minimization is given by:

$$\hat{\rho} = (E^H E)^{-1} E^H \rho = E^+ \rho \; [Eq. 3.4]$$

E^H is the conjugate transpose of E and E^+ is the Moore-Penrose pseudo inverse of E. In practice, the dimension of ρ and E is very large and computing E^+ is costly. A common approach to get the minimization solution is through conjugate gradient method[14]. Such method can reduce the computation complexity by looking for the optimal solution with a converging cost function.

3. 3 Results and discussions

3. 3. 1 Application of model-based reconstruction on in-vivo data

The model-based iterative reconstruction was applied for a dataset acquired from in vivo ^{13}C spCSI of rat kidney with four metabolites in the aliased spectrum, shown in Figure 3-1(b). Bicarbonate is a low SNR metabolite which only comprises approximately 1.5% percent of the hyperpolarized spins. Quantification of the bicarbonate peak requires significant amount of manual correction in the peak integral process since the bicarbonate peak is adjacent to a high pyruvate peak in the under-sampled spectrum and is susceptible to noise due to its low SNR. The model-based reconstruction provides an alternative way to derive the metabolic maps directly. Metabolic maps reconstructed with conventional CSI reconstruction and model-based iterative reconstruction are displayed in Figure 3-1(c, d). Little difference is observed from the two reconstruction methods for pyruvate image. A small amount of difference is found for lactate and alanine maps. For the bicarbonate map, the model-based reconstruction gives a result that matches the anatomical structure from the ^{1}H MRI overlay, with a much higher total amount than in the result from CSI reconstruction. The reconstruction result can be improved by incorporating more prior knowledge with closer estimation of the signal equation relating the acquired data and the distribution of metabolites.

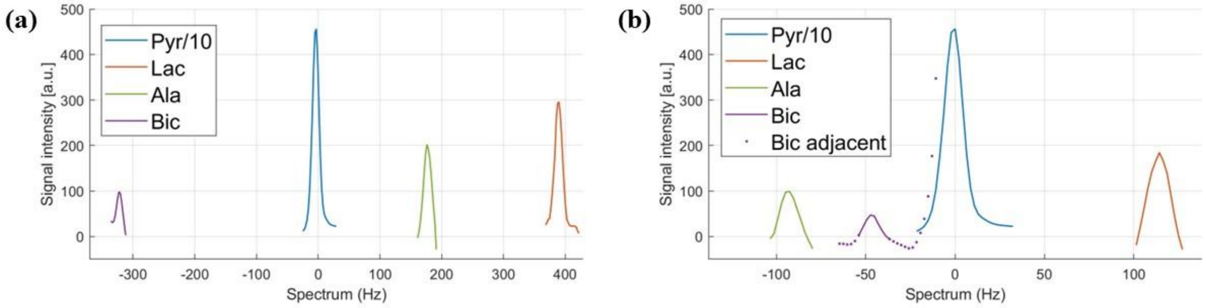

Fully sampled spectrum
spectral width > 800 Hz

Under-sampled spectrum
spectral width = 276 Hz

(c) CSI reconstruction

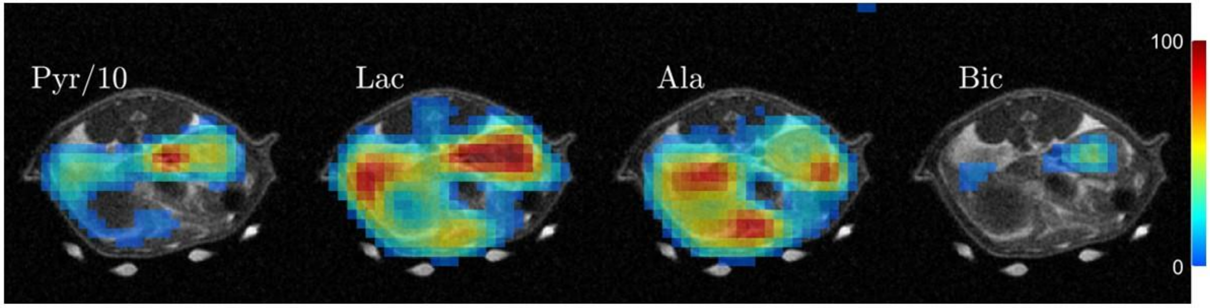

(d) Model-based iterative reconstruction

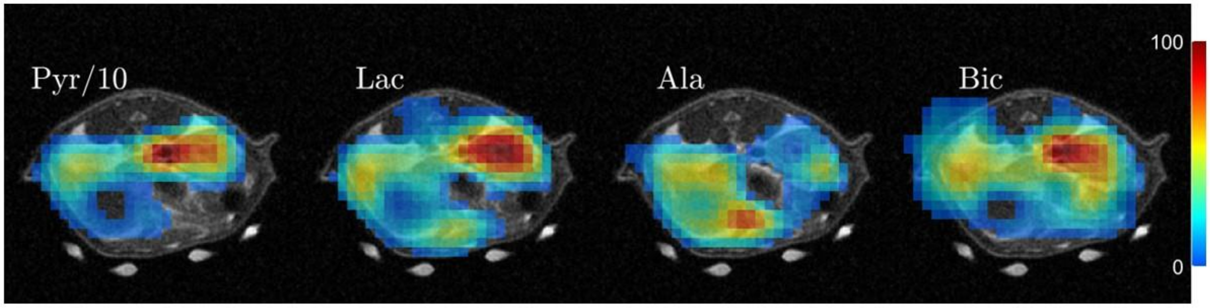

Figure 3-1 CSI and iterative reconstruction results for in vivo ^{13}C imaging of rat kidney. **(a)** spectrum of metabolites at fully sampled spectral width. **(b)** spectrum at under-sampled spectral width, with bicarbonate peak being a low intensity and adjacent to the high intensity pyruvate peak. **(c)** metabolic images reconstructed with CSI reconstruction overlayed on ^{1}H MRI. Pyruvate image intensity is scaled down by 10 for visualization using the same colormap with lactate, alanine, and bicarbonate. Image intensity larger than 20% of the max is displayed. **(d)** metabolic images reconstructed with model based iterative reconstruction with prior knowledge, displayed in the same specification as in (c).

The model-based reconstruction was also applied for a dataset acquired from in vivo ^{13}C spCSI of rat liver, shown in Figure 3-2. In the imaging slice, a phantom with circular cross section containing ^{13}C urea (Δf = 240Hz relative to pyruvate) was present during the image acquisition. SW of the spCSI acquisition was 274Hz. Hence, the urea peak was partially overlapped with pyruvate peak in the under-sampled spectrum in Figure 3-2(b). An image artifact at the position of the urea phantom was seen in the pyruvate map with CSI reconstruction, shown in Figure 3-2(c). Metabolic maps from model-based iterative reconstruction can successfully remove the image artifact, shown in Figure 3-2(d).

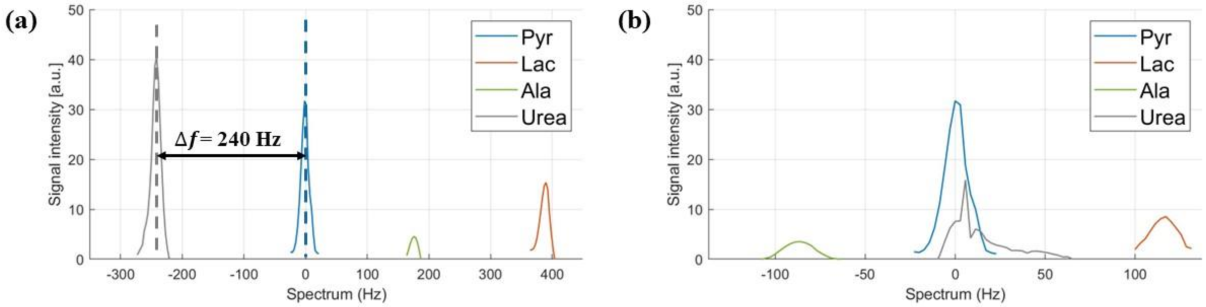

Fully sampled spectrum
spectral width > 720 Hz

Under-sampled spectrum
spectral width = 274 Hz

(c) CSI reconstruction

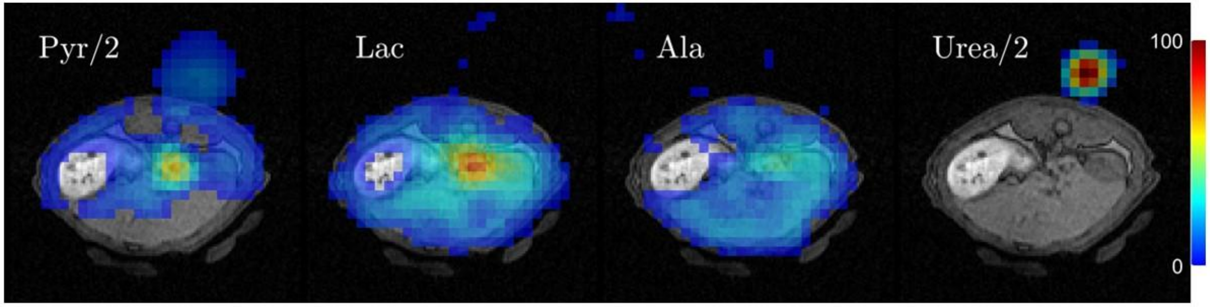

(d) Model-based iterative reconstruction

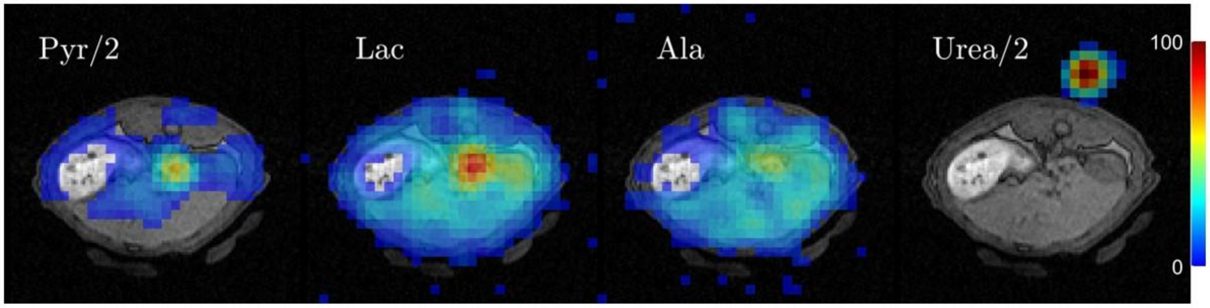

Figure 3-2 CSI and iterative reconstruction results for in vivo ^{13}C imaging of rat liver. **(a)** spectrum of metabolites at fully sampled spectral width. **(b)** Spectrum at under-sampled spectral width, with urea peak partially overlapped with pyruvate peak. **(c)** Metabolic images reconstructed with CSI reconstruction overlayed on ^{1}H MRI. Pyruvate and urea image intensity is scaled down by 2 for visualization using the same colormap with lactate and alanine. Image

intensity larger than 12% of the max is displayed. **(d)** metabolic images reconstructed with model-based iterative reconstruction with prior knowledge, displayed in the same specification as in (c).

3. 3. 2 Correction of reconstructed images using prior knowledge of $\mathrm{B_0}$

System imperfection and other factors may affect the data acquisition of MR signal, which drives the signal equation away from ideal condition. As discussed in 3.3.1, incorporating more prior knowledge can improve the accuracy of model-based iterative reconstruction. In Chapter 2, we assume that the $\mathrm{B_0}$ field is homogenous throughout the imaging volume. However, in reality $\mathrm{B_0}$ is inhomogeneous, represented as $B_0(r) = B_0 + \Delta B(r)$. Consequently, the signal equation is modified as:

$$S(t) = \iiint m(x, y, f) e^{-j2\pi[k_x(t)x + k_y(t)y + ft] - t/T_2^*} e^{-j2\pi\gamma\Delta B(x,y)t} df dx dy \; [Eq. 3.5]$$

The extra off resonance $\gamma\Delta B(x, y)$ will bring artifacts to the reconstructed image for model-based reconstruction if the encoding matrix E does not include such information[28]. Acquired signal is simulated for a uniformly distributed 2D disc phantom, under an inhomogeneous $\mathrm{B_0}$ field displayed in the top image of Figure 3-3(d). Without using the prior knowledge of $\mathrm{B_0}$, significant image artifacts are recognized in the reconstructed image via iterative reconstruction, as in Figure 3-3(a). The $\mathrm{B_0}$ map is estimated by measuring the shift of the resonance peak in the map of spectra from CSI reconstruction for each voxel . The reconstruction results after taking the prior knowledge of the estimated $\mathrm{B_0}$ is shown in Figure 3-3(b), where image artifacts are significantly reduced. The reconstruction can be further improved by fitting the $\mathrm{B_0}$ map estimated from peak shift to a polynomial surface, shown in Figure 3-3(c). The reconstructed image is completely recovered to ground truth in Figure 3-3(d), if the original $\mathrm{B_0}$ map is given.

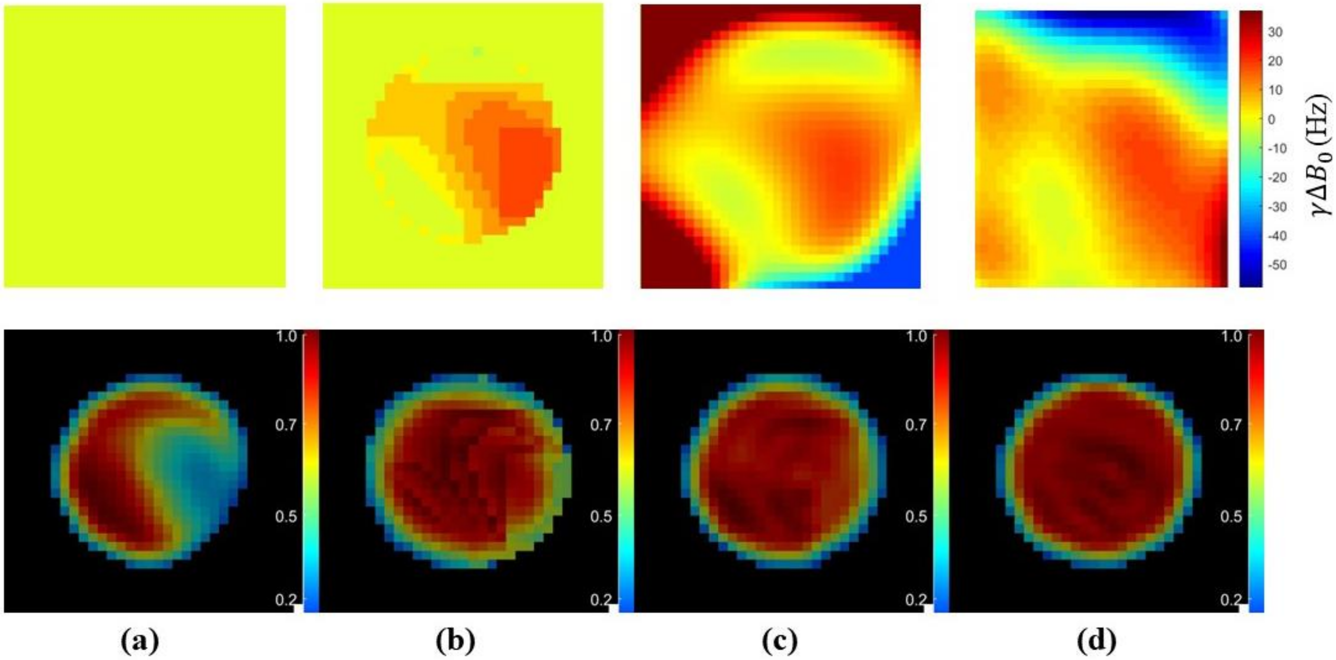

Figure 3-3 Reconstructed images of a digitally simulated uniform disc phantom via model-based iterative reconstruction, top row gives the B_0 map used in the model and bottom row displays the reconstruction result. **(a)** No knowledge of B_0 map **(b)** Knowledge of B_0 map estimated from peak shift **(c)** Knowledge of B_0 map estimated from peak shift, then fitted to a polynomial surface **(d)** Knowledge of the ground truth B_0 map

3. 4 Conclusions

With prior knowledge the model-based iterative reconstruction method can derive the metabolic images without performing the peak integral process, and effectively remove the artifacts from two partially overlapped peaks on the aliased spectrum. Simulation results for phantom with inhomogeneous B_0 map demonstrates the improvement of the reconstructed images by incorporating additional prior knowledge.

Chapter 4 : Accelerate Dynamic Hyperpolarized 13C using Low Rank Plus Sparse Reconstruction

The following chapter is partially adapted from: “Using Joint Spectral-Spatial Low Rank Plus Sparse (L+S) Reconstruction to accelerate dynamic Hyperpolarized 13C Spiral Chemical Shift Imaging In Vivo.” Proceeding of International Society of Magnetic Resonance in Medicine, 2022.

4. 1 Introduction

For dynamic metabolic imaging, the same image acquisition scheme is applied repeatedly over a period to gather dynamic change of the metabolic activities. While hyperpolarized ^{13}C substrates have limited lifetime for the enhanced polarization, we aim to acquire data with dimensions as large as possible (FOV, spatial/spectral resolution and time points). To achieve that, image acquisition of a single time frame should be completed in a period as short as possible. A desired strategy for image acceleration is to acquire only a portion of the fully sampled k-space per time point. The missing k-space data can be recovered via compressed sensing/low rank matrix completion if the following requirements are met: 1) The data is considered sparse in certain domains 2) The under-sampling pattern can create incoherent aliasing in the sparse-transform domain 3) A reconstruction algorithm that enforces both sparsity and data consistency[29].

An apparent feature of the dynamic metabolic images is that they look ‘similar’ to each other over the time course, as seen in Figure 2-11. The slowly changing behavior of the dynamic images can be viewed in two aspects: 1. the information along the time points are highly correlated; 2. they can be represented by a few non-zero values after transforming into certain domains (e.g., frequency domain or wavelet domain). Specifically, if we convert the dynamic images into a matrix M, where each column represents the dynamics of the same voxel at the same chemical shift frequency, M is considered low rank. At the same time, the transform of M into the frequency/wavelet domain, is considered sparse. These properties satisfy the sparsity requirement for compressed sensing/low rank matrix completion. The incoherent aliasing requirement is met if the under-sampling pattern is random for each time point. Data consistency enforcement is achieved using L_2-minimization on the under-sampled dataset. The process described here is generalized as low-rank plus sparse (L+S) reconstruction.

Otazo et al. showed the successful application of L+S reconstruction on randomly under-sampled 2D dynamic ^{1}H imaging datasets without significant loss of information compared with the result from a fully sampled dataset[29]. DeVience et al. adapts this method to dynamic ^{13}C metabolic imaging with low rank matrix completion only and the algorithm iterates on each element along the spectral dimension individually for spCSI data[30]. We adapt the L+S algorithm by operating the iterations on spatial and spectral dimension in a joint fashion, combining both low rank matrix completion and compressed sensing with sparsity. Additionally, a low rank and local sparse (LLS) reconstruction method is proposed, where the sparse matrix is divided into multiple blocks along the spectral dimension, and different thresholds are set for each block, thus retaining each frequency component's dynamic pattern.

4. 2 Methods

4. 2. 1 Low rank plus sparse reconstruction algorithm

The L+S reconstruction can be formulated as an optimization problem[29]:

$$\min_{L,S}\{\frac{1}{2}\|E*(L+S)-d_0\|_2^2+\lambda_L\|L\|_*+\lambda_S\|T*S\|_1\}\ [Eq. 4.1]$$

L and S are the output decomposed low rank and sparse matrices, $E*$ and $E'*$ are the forward NDFT operator, d_0 is the acquired under-sampled data. $T*$ and $T'*$ are the forward/inverse sparsity transform operator. $\|\cdot\|_2^2$ represents the L_2 norm, $\|\cdot\|_*$ represents the nuclear norm and $\|\cdot\|_1$ represents the L_1 norm. $\lambda_L$and λ_S act as tuning parameters controlling the contribution of the nuclear norm and L_1 norm terms.

The optimization problem is solved using iterative soft thresholding as described in Otazo et al.[29], shown in Figure 4-1. Soft thresholding operator $\wedge$ is defined as:

$$\wedge\{x,\lambda\}=\frac{x}{|x|}\cdot\max(|x|-\lambda,0)\quad [Eq. 4.2]$$

In the initialization, inverse NDFT operator transform the under-sampled data d_0 into 4D image space M_0. L_0 is initialized to be M_0 and S_0 is initialized to be a zero-matrix same dimension as M_0. In each iteration, singular value decomposition (SVD) on $M_n - S_n$ gives the singular value vector P and sparsity transform (principal component analysis in our study) on $M_n - L_n$ gives the sparsity space Λ. Soft thresholds λ_L and λ_S are applied on P and Λ, respectively. The recovered signal d_n is derived from forward NDFT transform of the sum of updated low rank image L_n and sparsity image S_n. Finally, M_n is updated by enforcing the data consistency between recovered signal d_n and d_0, where M_{res} represents the residual image from the inverse NDFT of the difference between d_n and d_0. In this study, multiplication of the encoding matrix serves as the forward NDFT operator, and inverse of the encoding matrix with conjugate gradient serves as the inverse NDFT operator, abbreviated as CG in the following context. Iteration stops when the update on L+S is sufficiently small. Throughout the iterations, a single threshold is set on the singular values of low rank matrix and another single threshold is set on the sparse-transformed matrix, presented as global low rank and sparsity (GLS)

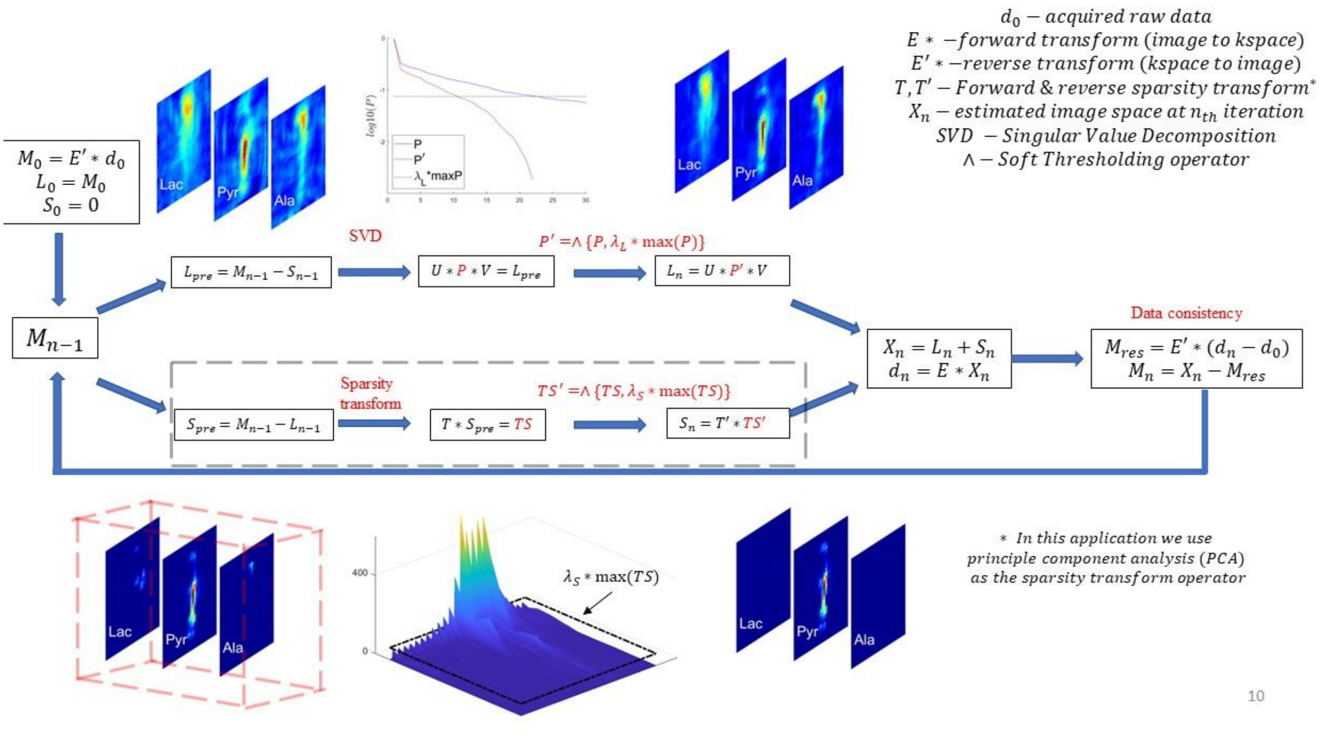

Figure 4-1 L+S algorithm with global low rank and sparsity (GLS). The process indicated in grey dashed lines represent the global sparsity soft thresholding.

4. 2. 2 Low rank plus local sparse reconstruction algorithm

Milshteyn et al. have demonstrated the application of local low rank plus sparse decomposition model for HP ^{13}C MRI with 2D bSSFP sequence (non-spectroscopic imaging)[31] , which has local low rank properties as neighboring tissues have similar spatiotemporal dynamics in a low rank manner, but not across the whole FOV. Spectroscopic imaging exhibits ‘local sparse’ property as neighboring spatial components have similar dynamics, but each frequency component may not share the same dynamics. The low rank plus local sparse (LLS) algorithm is formulated as:

$$\min_{L,S}\{\frac{1}{2}\|E(L+S)-d\|_2^2+\lambda_L\|L\|_*+\sum_{i=1}^{N_b}\lambda_{S_i}\|B_iTS\|_1\}[Eq.4.3]$$

B_i is an operator that selects an image block b and transform into the spatiotemporal matrix. In this study, we attempt the block size of 1 on spectral dimension F only. λ_{S_i} is the respective threshold for block i. Figure 4-2 shows the soft thresholding process with local sparsity that replaces the global sparsity indicated in dashed grey rectangle of Figure 4-1.

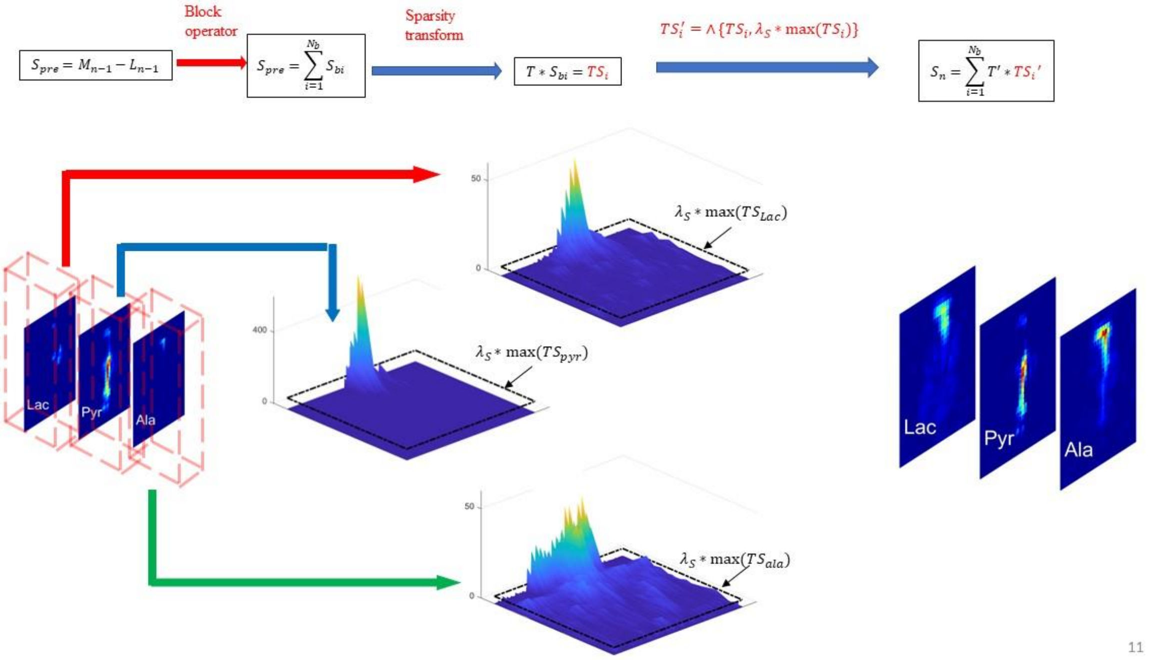

Figure 4-2 Soft thresholding process with local sparsity along the spectral dimension

4. 2. 3 Simulation with digital phantom

For testing the algorithm, we constructed a digital 2D spectroscopic imaging phantom comprising of 4 discs representing the vasculature, kidneys, and liver/body, and 3 spectral peaks (pyruvate, alanine, and lactate), each intensity characterized by the typical dynamic measurement in abdominal region of a mouse following hyperpolarized pyruvate injection. The pyruvate is the substrate metabolite with dominant signal intensity, while lactate and alanine are product metabolites with lower signal intensity. Ground truth (GT) of the phantom is displayed in Figure 4-3. Spiral trajectory with 24 interleaves, 30 x 30 matrix size, 24 echoes and 280 Hz spectral width was used for generating of the ground truth spCSI raw data. Random 8 out of the total 24 interleaves were selected to generate the under-sampled raw data. Random Gaussian noise was added to the under-sampled data on the same scale as in vivo imaging. Reconstruction on the under-sampled dataset with the inverse NDFT operator gives the image matrix M_0 at the initialization step of the L+S algorithm. We chose CG as the NDFT operator for this study as it guarantees convergence[32]. Peak integral of M_0 gives the corresponding dynamic images, denoted as CGR3, representing a 3-fold acceleration. From M_0, L+S reconstruction was performed for 50 iterations with GLS and LLS respectively. Peak integral of the derived $L_{50} + S_{50}$ gives the corresponding dynamic images. Regularization parameter λ_L is set to 0.075, while λ_S and λ_{Si} are set to 0.1, based on the empirical value and observation of the convergence speed. Difference images are compared between L+S results and ground truth. Dynamic curves characterizing the mean intensities in the selected regions of interest (ROIs) for each time point are compared for the three reconstruction methods. The overall performance of the reconstruction is assessed using normalized root mean squared error (nRMSE), according to the following formula[33]:

$$nRMSE = \frac{\sqrt{\sum_{x_i,yi,ti}^{N^2 * N_t} (x_{recon}(xi,yi,ti) - x_{GT}(xi,yi,ti))^2}}{\sqrt{\sum_{x_i,yi,ti}^{N^2 * N_t} (x_{GT}(xi,yi,ti))^2}} \qquad [Eq. 4.4]$$

x_{recon} (xi, yi, ti) is the image intensity at voxel $xi, yi,$ time point ti of the reconstructed dynamic images, x_{GT} is the ground truth dynamic images, N is the image matrix dimension and N_t is the total number of time points

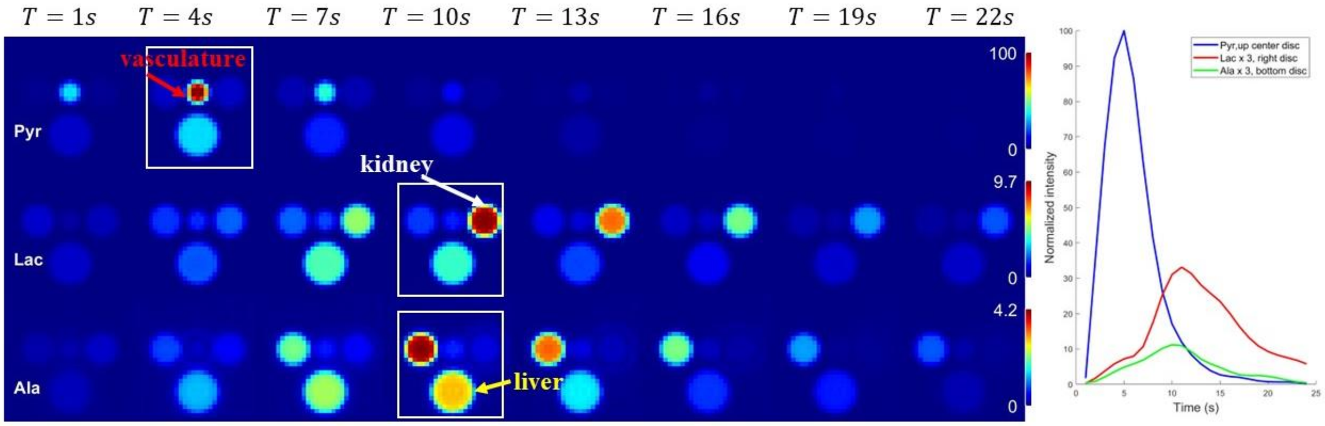

Figure 4-3, Ground truth of the dynamic phantom. Every 3 under-sampled time points starting at 0 seconds are displayed for each metabolite. Dynamic curves representing mean intensities in respective ROIs are plotted on the right.

4. 2. 4 In vivo mouse body imaging with true acceleration

For the in vivo imaging study aimed for true acceleration, we use the same spiral k-space with 24 interleaves as in simulation. The image acquisition scheme was carried out in such a way: one fully sampled block of 24 interleaves was carried out for every 3 second interval. The entire scan has 20 fully sampled blocks, or equivalently 24 x 20 = 480 excitations for a total scan time of 60 seconds. The order of the interleaves was randomly permuted for each block. Thus, dynamic images with 20 time points, 3 second temporal resolution can be reconstructed using the fully sampled blocks, whereas dynamic images with 60 time points, 1 second temporal resolution can be reconstructed using every 8 interleaves (3-fold under-sampled). Figure 4-4 illustrates the generation of dynamic images at two temporal resolutions using the same data acquired.

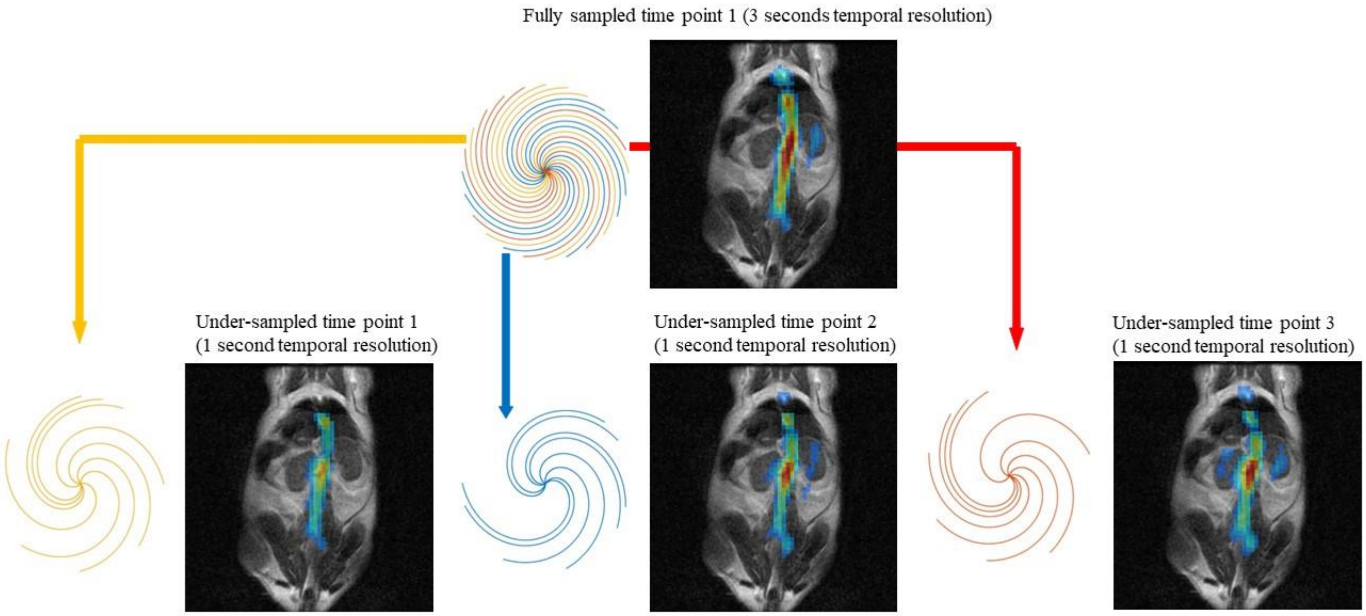

Figure 4-4 Illustration of pseudo-random under-sampling of the spiral k-space within one fully sampled block for in vivo mouse imaging with effective acceleration factor of 3.

In vivo 2D spCSI with the designed acquisition scheme was performed on a healthy mouse using clinical 3T GE MR scanner with a ^{1}H-^{13}C dual-tuned RF coil. The imaging slice has a slice thickness of 10 mm and set in coronal orientation covering the abdomen of the mouse body. The animal received a 1μmol/g dose of 125mM hyperpolarized pyruvate (approximately 0.23 mL) injected over 6 seconds through a tail vein catheter.

The acquired dataset was first reconstructed at 3 seconds temporal resolution via inverse NDFT operator with CG, followed by peak integral. The derived non-accelerated dynamic images, denoted as CGR1, served as a reference for the accelerated dynamic images. Similar to the simulation, accelerated dynamic images were acquired with CGR3, GLS and LLS, with λ_L, λ_S and λ_{Si} set to 0.075, 0.25 and 0.25 respectively. Choice of the thresholding parameter is based on the observation of effectiveness in artifact removal as well as evaluation of the data consistency at the end of iterations.

4. 3 Results

4. 3. 1 Digital simulation results

Figure 4-5 shows the results of the digital simulation using CGR3, GLS and LLS. CGR3 exhibits significant image artifacts from under-sampling. Both GLS and LLS largely eliminate the image artifacts. The LLS algorithm can capture the proper spatial information in frequency bins with lower intensities through the blocked soft thresholding, producing a better reconstruction result as seen in the difference image. Figure 4-6 shows dynamic curves of the ROI selected for each metabolite. The dynamic curve on the selected ROI and its difference with respect to the ground truth also show that LLS performs better in terms of replicating the dynamic pattern for lactate and alanine. Table 4.1 shows the nRMSE for the simulation results. CGR3 exhibits largest difference from the ground truth, with all three metabolites higher than 25%. Differences for the pyruvate images are on the same order of 3% for both GLS and LLS, verifying the similar performance of the two methods on metabolite with dominant signal intensity. LLS outperforms GLS for lactate and alanine, in accordance with the result in Figure 4-5 and Figure 4-6.

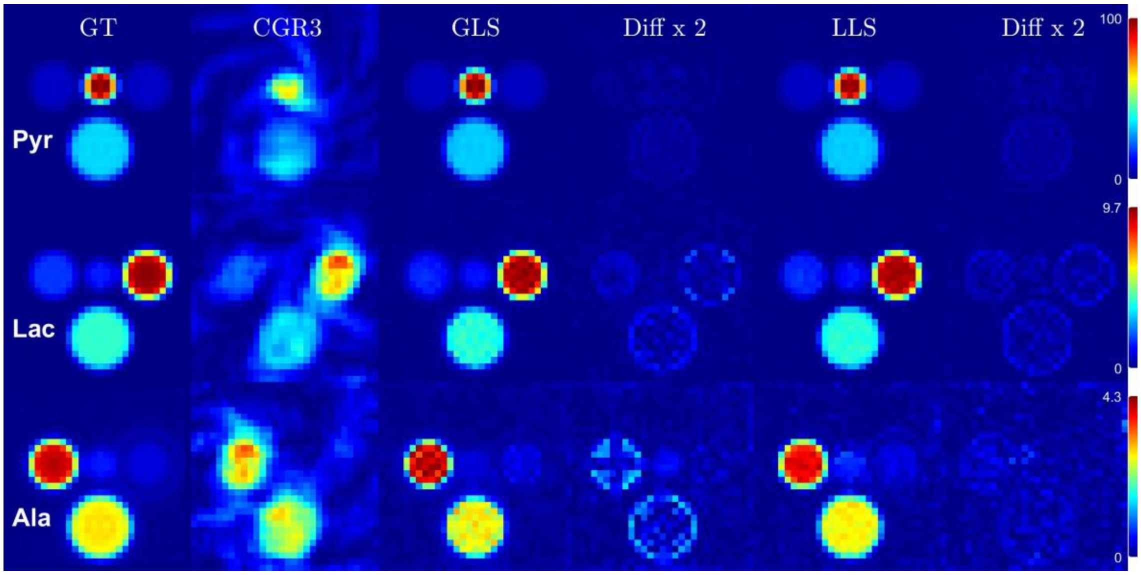

Figure 4-5, Result of simulation on digital phantom at the time points indicated by white squares in Figure 4-4. 1st column: ground truth image with fully sampled k-space; 2nd column: reconstructed image with inverse NDFT (CGR3); 3rd column: reconstructed image with GLS; 4th column: differences between GLS and ground truth; 5th column: reconstructed image with LLS (block size 1 on frequency dimension only); 6th column: differences between LLS and ground truth.

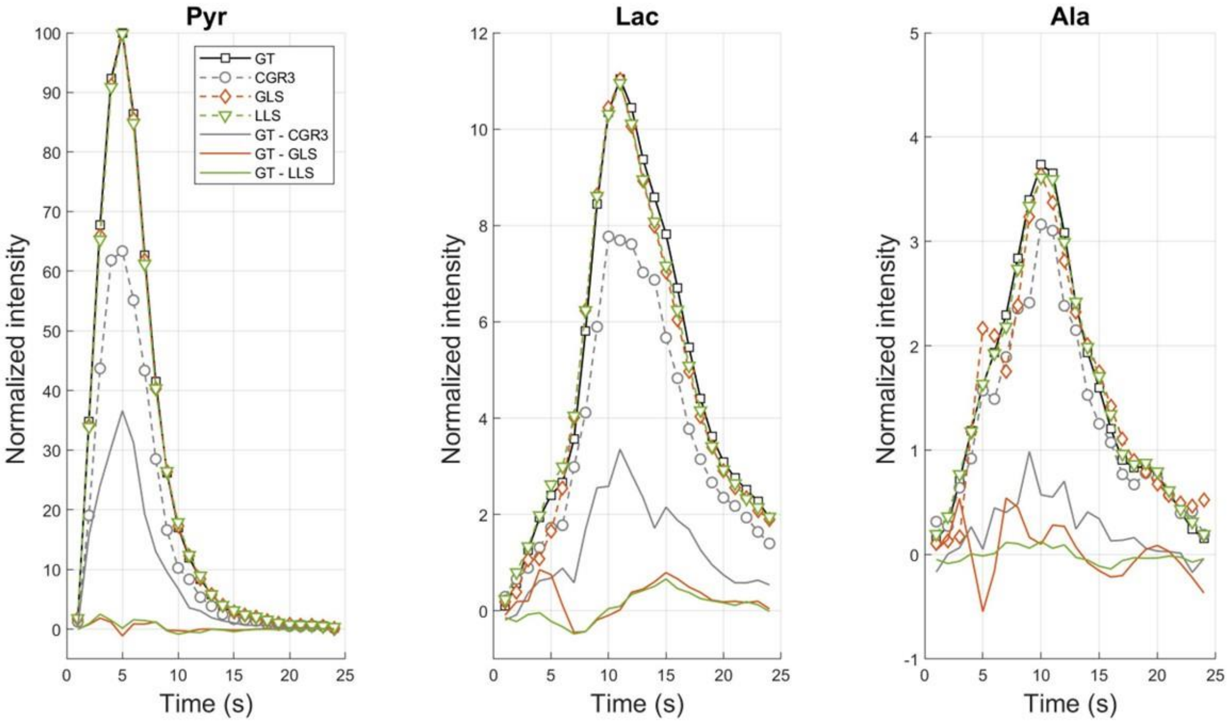

Figure 4-6, Dynamic curves representing mean intensities in the selected ROIs for the digital simulation results. Ground truth in solid black squares, CG in dashed grey circles, GLS in dashed red diamonds and LLS in dashed green triangles. The difference between ground truth and reconstructed results are plotted in solid curves below.

nRMSE	CGR3	GLS	LLS
Pyr	0.3776	0.0330	0.0357
Lac	0.3010	0.1186	0.0832
Ala	0.2803	0.1774	0.0855

Table 4.1 nRMSE measurement on the digital simulation results using three different reconstruction methods, directly from inverse NDFT (CGR3), global low rank plus sparse (GLS) and low rank plus local sparse (LLS)

4. 3. 2 In vivo imaging results

Reconstructed images of the fully sampled k-space at 3 seconds temporal resolution (CGR1) are displayed in the first row of Figure 4-7 (a-c). Reconstructed images of the under-sampled k-space at 1 second temporal resolution (effective acceleration of 3 folds) with CGR3, GLS and LLS are displayed in the second to forth row. Dynamic curves of the selected ROIs for three metabolites are plotted in the right. For pyruvate images, both GLS and LLS can properly remove the artifacts and restore the correct dynamic pattern. For lactate and alanine images, both methods can remove the artifacts, but GLS fails to capture the correct dynamic pattern in reference to CGR1. In GLS, sparsity threshold is set in proportion to the sparsity transform of the entire 4D spatial-spectral-temporal matrix, dominated by the pyruvate signal. Hence, image information of the lower intensity metabolites in the sparse domain cannot be properly separated from the components representing artifacts/noise, and the dynamic pattern is therefore affected by the dominant metabolite. In LLS, block operations downsize the sparsity domain in the soft thresholding process, facilitating the separation of image versus artifacts/noise. Consequently, as seen in Figure 4-7 (b, c, e, f), images and corresponding dynamic curves from LLS correctly represent the intensity of the products, which lasts for several seconds after the bolus arrival as expected.

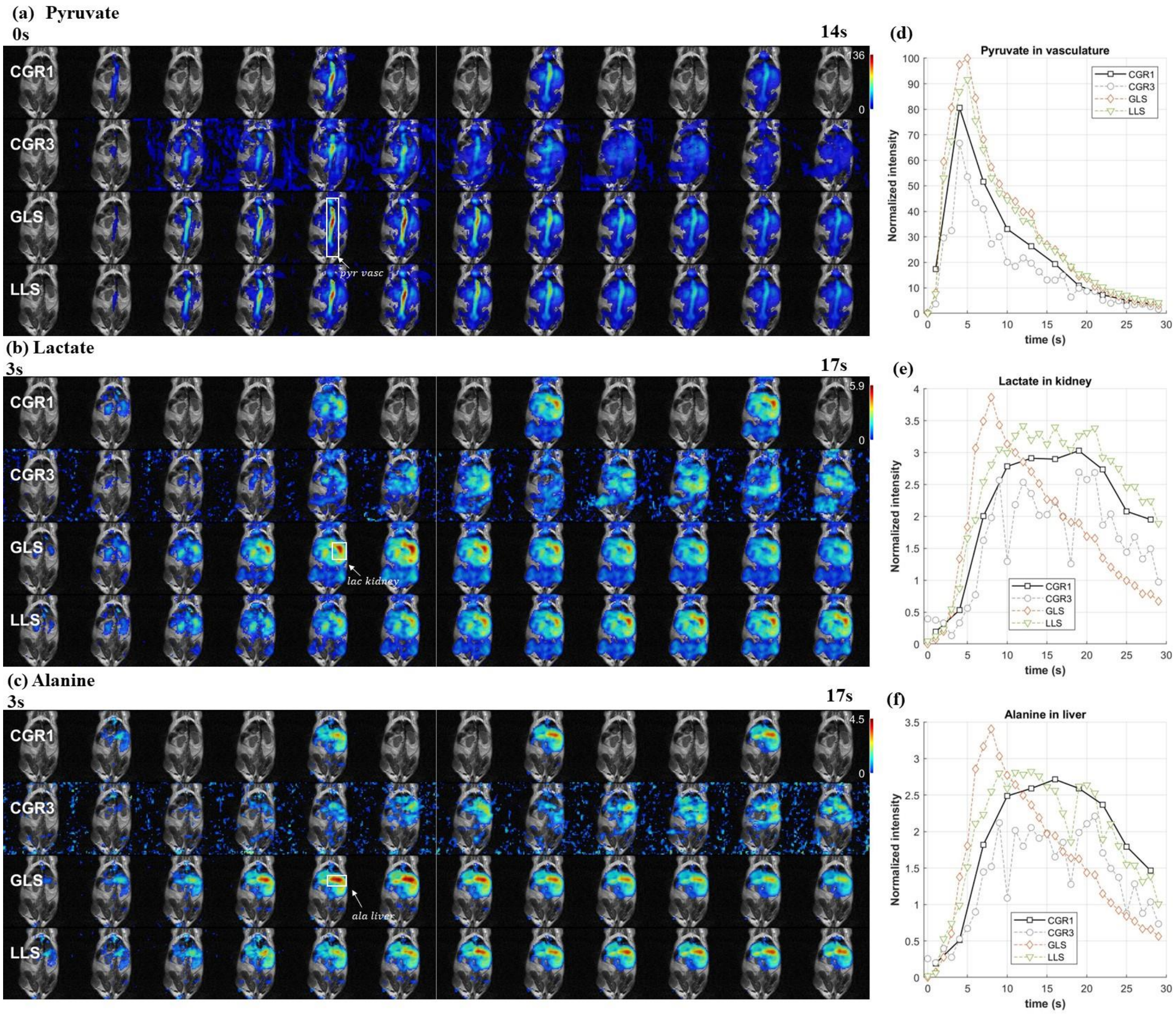

Figure 4-7 Dynamic images of the in vivo imaging data reconstructed from fully sampled k-space with inverse NDFT (1st row of a,b and c, CGR1, temporal resolution at 3 seconds/time point), from under sampled k-space with inverse NDFT (2nd row, CGR3, temporal resolution at 1 second/time point), from under sampled k-space with GLS(3rd row), and from under sampled k-space with LLS(4th row). **(a)** Pyruvate dynamic images starting at 0 second after the start of data acquisition. **(b)** Lactate dynamic images starting at 3 second after the start of data acquisition. **(c)** Alanine dynamic images starting at 3 seconds after the start of data acquisition. **(d-f)** Dynamic curves for the mean intensity in the ROI indicated by the white rectangle of each metabolite.

Since in vivo imaging with true acceleration cannot provide ground truth derived from fully sampled k-space, alternative way to assess the accuracy of the reconstruction is by averaging each adjacent three time points of the accelerated results to produce the dynamic image series with the same 3s temporal resolution as CGR1, shown in

Figure 4-8. For all three metabolites, 3-point-average of LLS highly resembles CGR1, with corresponding dynamic curves close to each other. For the two low intensity metabolites, 3-point-average of GLS mismatches CGR1, with attenuation in intensity towards the later time points, indicated by the red arrows. 3-point-average of LLS resembles CGR1, but with less background noise. This provides additional motivation to use LLS for background noise removal.

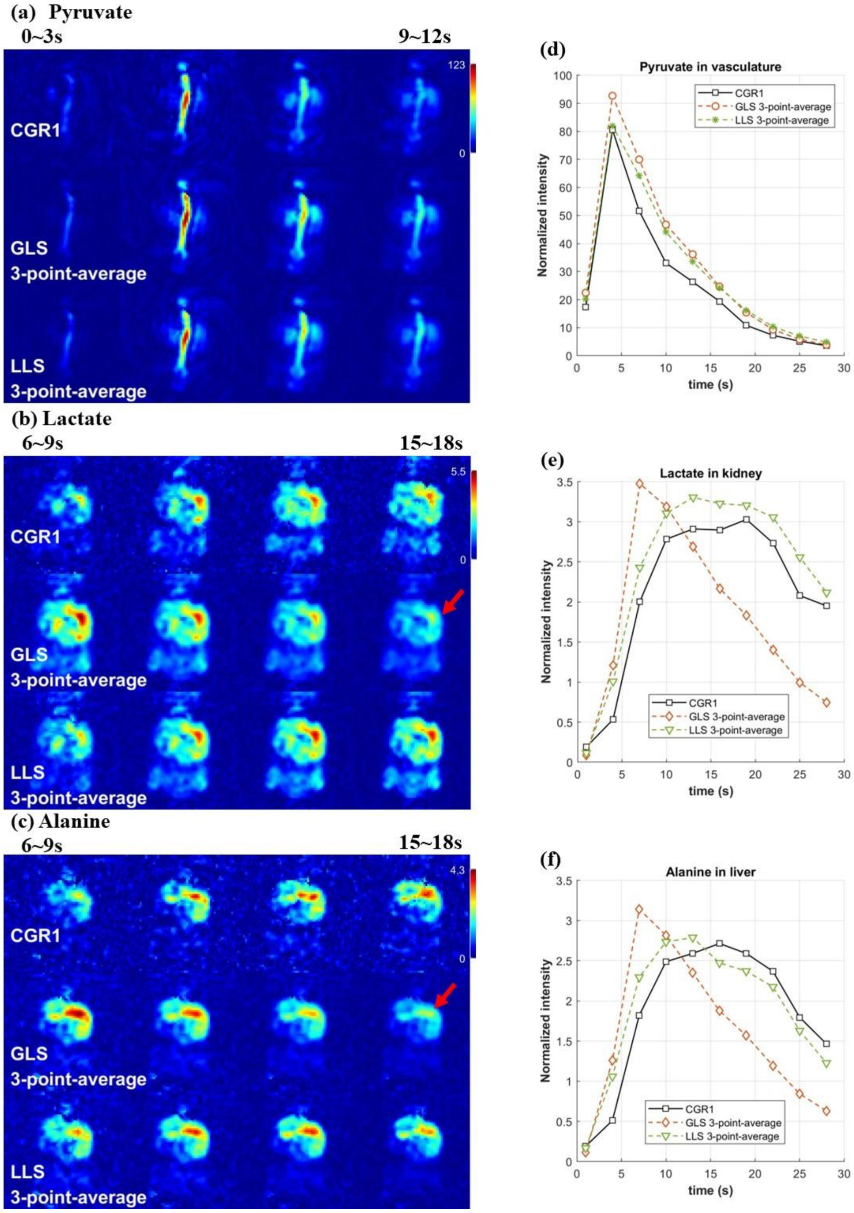

Figure 4-8, Dynamic images reconstructed at 3 seconds temporal resolution with inverse NDFT (1st row of a, b and c, CGR1), averaging adjacent 3 time points for GLS (2nd row), averaging adjacent 3 time points for LLS (3rd row). **(a)** pyruvate dynamic images with first time point covering data acquired during 0~3 seconds after start of data acquisition. **(b)** lactate dynamic images with first time point covering 6~9 seconds. **(c)** alanine dynamic images with first time point covering 6~9 seconds. **(d-f)** dynamic curves for the mean intensity in the ROI of the respective metabolite.

4. 4 Conclusion

In this study, we developed a low rank plus local sparse reconstruction algorithm to accelerate 2D hyperpolarized ^{13}C imaging with spCSI acquisition. Using local sparsity, the proposed method can successfully reconstruct under-sampled dynamic spCSI data without significant artifacts and properly restore the distinct dynamic pattern of lower intensity metabolites. Thus, effective imaging acceleration can be achieved.

Chapter 5 : Highly under-sampled 3D Dynamic Hyperpolarized 13C Spiral Chemical Shift Imaging using Low Rank Plus Local Sparse Reconstruction

5. 1 Introduction

3D Spiral Chemical Shift Imaging (3D spCSI) is an established metabolic imaging modality that covers additional spatial information along slice dimension[34]. Based on the 2D spCSI sequence, 3D spCSI acquires the fully sampled 4D k-space $[k_{xy}, k_z, k_f]$ by applying phase encoding (PE) along the z-direction for each spiral interleaf. Due to the limitation of the maximum gradient strength and/or slew rate (SR) on the MR scanner, the acquisition time for one fully sampled 3D spCSI time point is typically more than 10 seconds. As HP 13C agents have a limited lifetime of 1~2 minutes, it is rather challenging to perform dynamic 3D spCSI with such low temporal resolution. In previous chapter, we have developed L+S reconstruction for under-sampled 2D spCSI acquisitions with 3-fold effective acceleration. In addition, the adaptation of low rank plus local sparse (LLS) improves the accuracy of the accelerated images for the metabolic products - lactate and alanine, whose intensities are comparatively much lower than the injected substrate - pyruvate. In this study, we extend the LLS reconstruction to 3D spCSI with an effective acceleration of 4 folds. The study comprises a simulation with digital phantom and in vivo mouse body imaging with injection of hyperpolarized [1-^{13}C]pyruvate.

5. 2 Methods

Data acquisition

For both simulation and in vivo scan, the 3DspCSI uses an 8-interleave 2D spiral trajectory with 40 x 40 mm FOV, 2.5 x 2.5 mm^2 nominal in-plane resolution. 12 phase encoding steps are applied in slice direction with 48 mm zFOV. 75% under-sampling is performed by pseudo-randomly selecting 2 out of 8 interleaves per PE step. Thus, an under-sampled time point comprises 24 excitations, each followed by spiral readout of 18 echoes at a spectral width of 280Hz for encoding the spectral information, with a repetition time of 3 seconds, equivalent to a temporal resolution 20 frames/minute. The pseudo-random selection table of the interleaves satisfies the condition that each interleaf is played exactly once per PE step in a block formed by 4 adjacent under-sampled time points. This allows reconstructing the acquired data with fully sampled 4D k-space at original temporal resolution (12 seconds per time point, or 5 frames/minute). A multiband RF excitation pulse[35] was used for in vivo mouse imaging, which applied different flip angles for each metabolite (1° on Pyr and 4° on both Lac and Ala for each excitation). A total of 28 under-sampled time points were acquired. First 16 time points have adequate SNR and are used for image reconstruction.

Digital phantom simulation

A 3D dynamic phantom with cylinders representing the vasculature, kidneys, liver and heart in a mouse was created to simulate the signal acquired in a 3D spCSI mouse imaging. Ground truth (GT) of the phantom was derived from reconstructing the fully sampled 4D k-space for a total of 16 under-sampled time points. Under-sampled data were derived using the pattern described priorly. Random Gaussian noise was added to the under-sampled data on the same scale as in vivo imaging.

Experimental setup

In vivo imaging in a healthy mouse (mouse ID m12) was performed using clinical 3T GE MR scanner with a ^{1}H-^{13}C dual-tuned RF coil. A dose of 10 uL/g body weight of hyperpolarized pyruvate (~80 mM) was injected through a tail vein catheter. Samples were prepared using a GE SpinLab polarizer operating at 5 T and 0.9 K.

Image reconstruction

Similar to the method in Chapter 5, reconstruction on the under-sampled data with inverse NDFT operator gives the initial accelerated image data (CGR4). Reconstruction on full k-space gives the non-accelerated images (CGR1). Two types of configurations of the LLS reconstruction were tested for the simulation and applied to the in vivo data. For type 1 (Figure 5-1A), both slice and time dimension are concatenated to form the low rank/sparse dimension, whereas type 2 (Figure 5-1B), only the time dimension is used.

In both types, the iterative reconstruction went through 3 stages. Due to the high acceleration factor (R=4) and relatively low SNR of the acquired 3D spCSI dataset, setting a proper low rank and sparsity threshold is important to ensure the convergence of the LLS algorithm. In the first stage, global low rank reconstruction (sparsity matrix being zero) is applied, where artifacts from the dominant image components are significantly reduced. In stage 2, global low rank plus sparse reconstruction is applied with sparsity threshold set based on the derived low rank image from stage 1, further eliminating the artifacts. In stage 3, low rank plus local sparse is applied to the blocked Casorati matrices to recover the distinct dynamic patterns along the dimension being blocked. Type 1 uses a block size of 1 along spectral dimension, while type 2 uses a block size of 1 along both spectral and slice dimension.

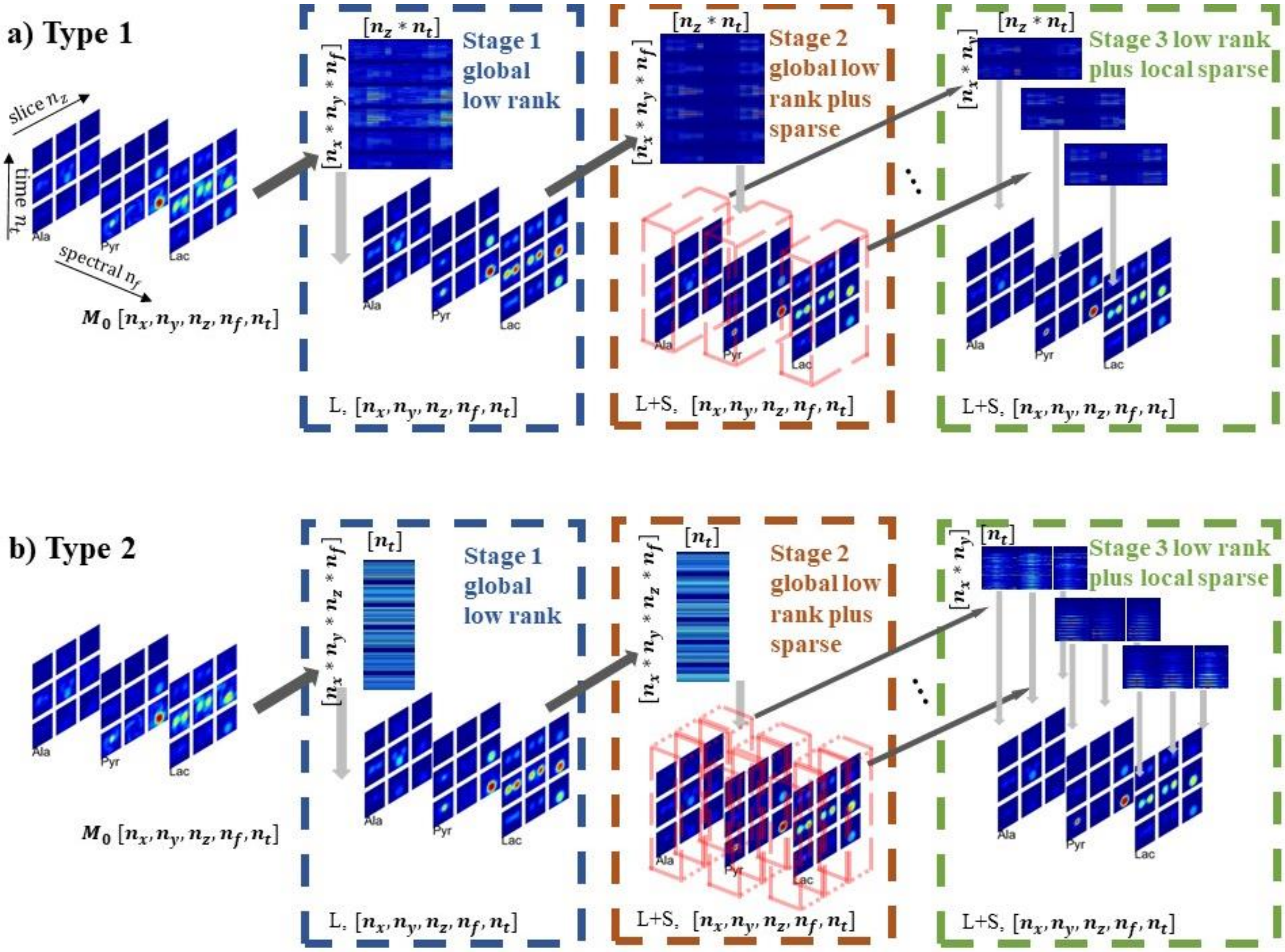

Figure 5-1, LLS Reconstruction algorithm for 3DspCSI with **(a)** configuration type 1 and **(b)** configuration type 2

5. 3 Results

5. 3. 1 Digital simulation results

Figure 5-2(a-d) presents ground truth of the digital phantom. Figure 5-2(e) shows the simulation results at the selected slices and time points. Before LLS iterations, the initial accelerated image CGR4 exhibits severe artifacts due to under-sampling. With highly under-sampled data (4 folds), inverse NDFT performs poorly in search for the image that corresponds to the under-sampled k-space. Therefore, reconstruction results for CGR4 present as blurred images with image intensity spread out in a large area outside the phantom.

Both types of LLS can successfully eliminate the artifacts and recover the ground truth images. Figure 5-3 shows the dynamic curves representing the mean intensities in the selected ROIs. Dynamic curves for CGR4 drop below the ground truth significantly, as their image intensity in the ROIs is redistributed to the area outside. LLS reconstruction iteratively derives the solution image with the constraints of low rank property and sparse property. In both types, the derived images fit closely to the ground truth.

Measurement of error with respect to the ground truth using nRMSE was repeated for the 3D simulation, listed in Table 5.1. Error for CGR4 is undoubtfully large, whereas both types of LLS reduce the error down to ~20%. 4 fold acceleration (75% under-sampled) is considered to be the highest acceleration factor achievable using L+S algorithm in previous studies[Mil, 127], while the reconstruction begins to breakdown considerably with more under-sampling.

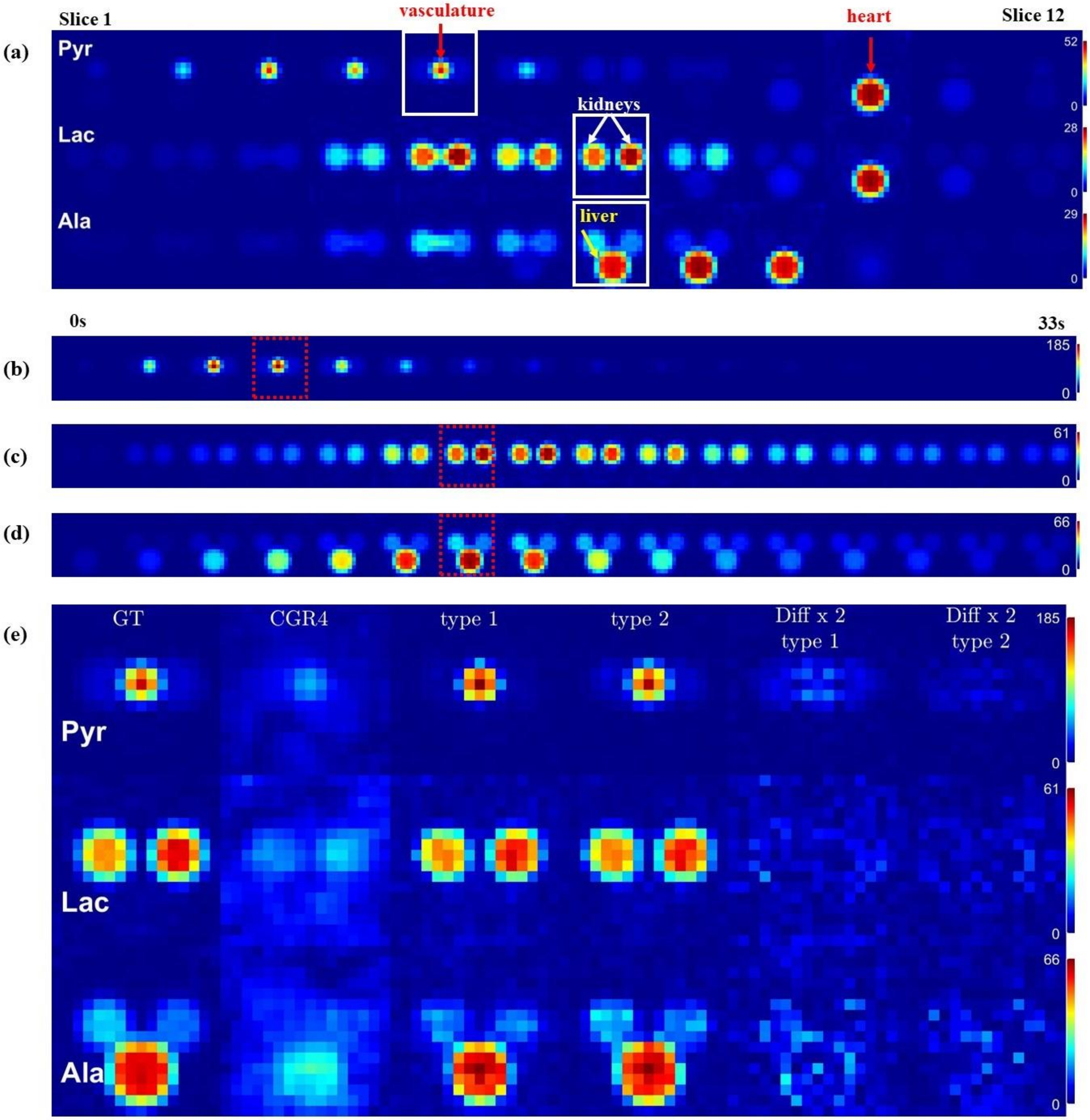

Figure 5-2, Simulation results from digital phantom with 3 metabolites (pyruvate, lactate, and alanine). **(a)** Time-averaged mean intensity of the ground truth (GT) in all slices for the three metabolites on each row. Arrows point out the regions of interest (ROIs) where dynamic information is evaluated. **(b-d)** Dynamic images for the three metabolites at selected slices (indicated by white squares in A) of the ground truth, with pyruvate at vasculature, lactate at kidneys and alanine at liver. **(e)** Reconstructed images with CGR4, type 1 LLS and type 2 LLS at the selected time point (indicated by red squares in b-d) of the corresponding slice when each metabolite reaches its peak intensity. The last two columns represent the difference between the reconstructed images and the ground truth.

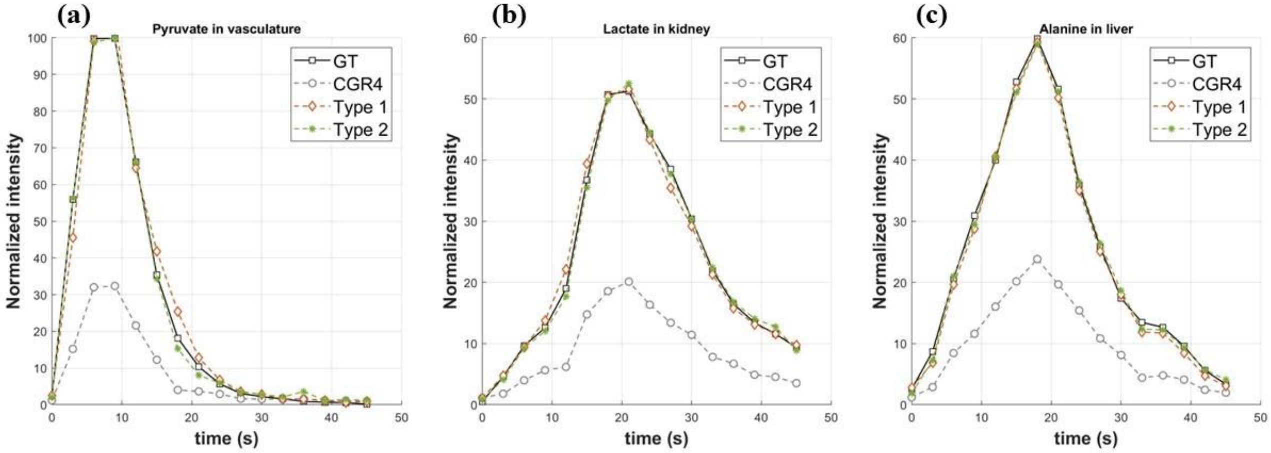

Figure 5-3 Dynamic curves representing mean intensities in the selected ROIs for **(a)** pyruvate **(b)** lactate **(c)** alanine. CGR4 (grey dotted) indicates the initial accelerated images via inverse NDFT. Type 1 LLS (red dotted) and Type 2 LLS (green dotted) fit closely to the ground truth (black solid)

nRMSE	CGR4	Type 1 LLS	Type 2 LLS
Pyr	0.7217	0.1925	0.1705
Lac	0.7141	0.1915	0.2014
Ala	0.7026	0.2393	0.2301

Table 5.1 nRMSE measurement on the digital simulation results using three different reconstruction methods, direct inverse NDFT (CGR4), low rank plus local sparse (LLS) with type 1 configuration and low rank plus local sparse with type 2 configuration.

5. 3. 2 In vivo imaging results

Figure 5-4(a) is the ^{1}H MRI that provides anatomical information in determining the ROI to characterize metabolite dynamics. Figure 5-4(b-d) are the time-averaged metabolic images displaying the spatial distribution of image intensity for each slice. One representative slice is selected for each metabolite for the analysis of dynamic information afterwards. The ROIs for vasculature, heart, kidneys and liver are determined based on the time-averaged images together with the ^{1}H MRI. Figure 5-4(e-g) displays the accelerated dynamic images reconstructed with CGR4 and two types of LLS. Artifacts seen in CGR4 are mostly eliminated through LLS. Dynamic curves for the mean intensity in the respective ROI are plotted on the right of the dynamic images. LLS provides more dynamic information that indicates the accurate time point each metabolite reaches its peak, which cannot be captured through the non-accelerated images, CGR1.

Evaluation for the accuracy of LLS reconstructions through comparing the average of 4 time points with corresponding CGR1 images is displayed in Figure 5-5. Since each fully sampled 3D spCSI takes 12 seconds, intensity of the metabolite can change significantly during one fully sampled time point. While k-space data on each spiral interleaf represent image at the instant when it is sampled, the full k-space combining these interleaves would not represent the k-space corresponding to the time-averaged image in that fully sampled time point. The combined full k-space would generate an image with swirl artifacts instead, with level of the artifacts proportional to the rapidness of the change during the sampling window. This phenomenon can be visualized in the CGR1 images for pyruvate (Figure 5-5a) versus lactate (Figure 5-5b) and alanine (Figure 5-5c), as the pyruvate intensity changes rapidly during the bolus arrival, while lactate and alanine gradually changes over time with exponential decay.

In type 1 LLS, vasculature pyruvate has an artifact component contaminated by the high image intensity in the heart slice, indicated by the red arrows. Alanine intensities in the two liver slices are also affected by each other. Since type1 LLS uses slice dimension as low rank/sparse dimension, the widely different spatial distribution of pyruvate in these slices cannot be properly separated in type 1 configuration. 4-point-average for type 2 LLS shares high resemblance to the CGR1 images.

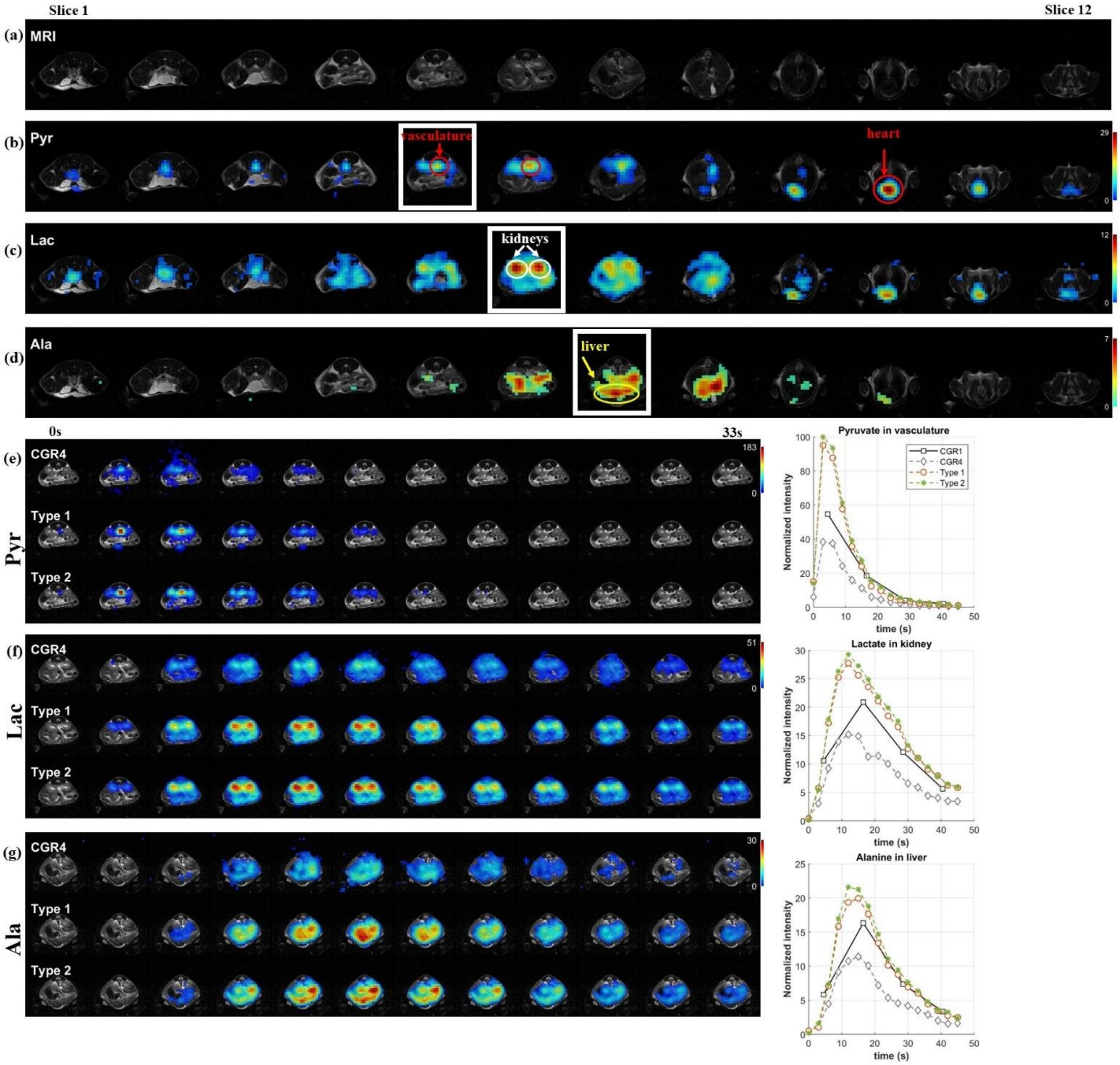

Figure 5-4, Reconstruction results for in vivo mouse imaging. **(a)** ^{1}H MRI for anatomical overlay. **(b-d)** Time-averaged metabolic maps in all slices from reconstruction on the fully sampled k-space. Arrows point out ROIs. **(e-g)** Accelerated dynamic images at the representative slice. For each metabolite, 12 under-sampled time points starting at 0 seconds after start of data acquisition are presented. Dynamic curves of the non-accelerated images (CGR1) and accelerated images (CGR4, type 1 LLS and type 2 LLS) are plotted on the right.

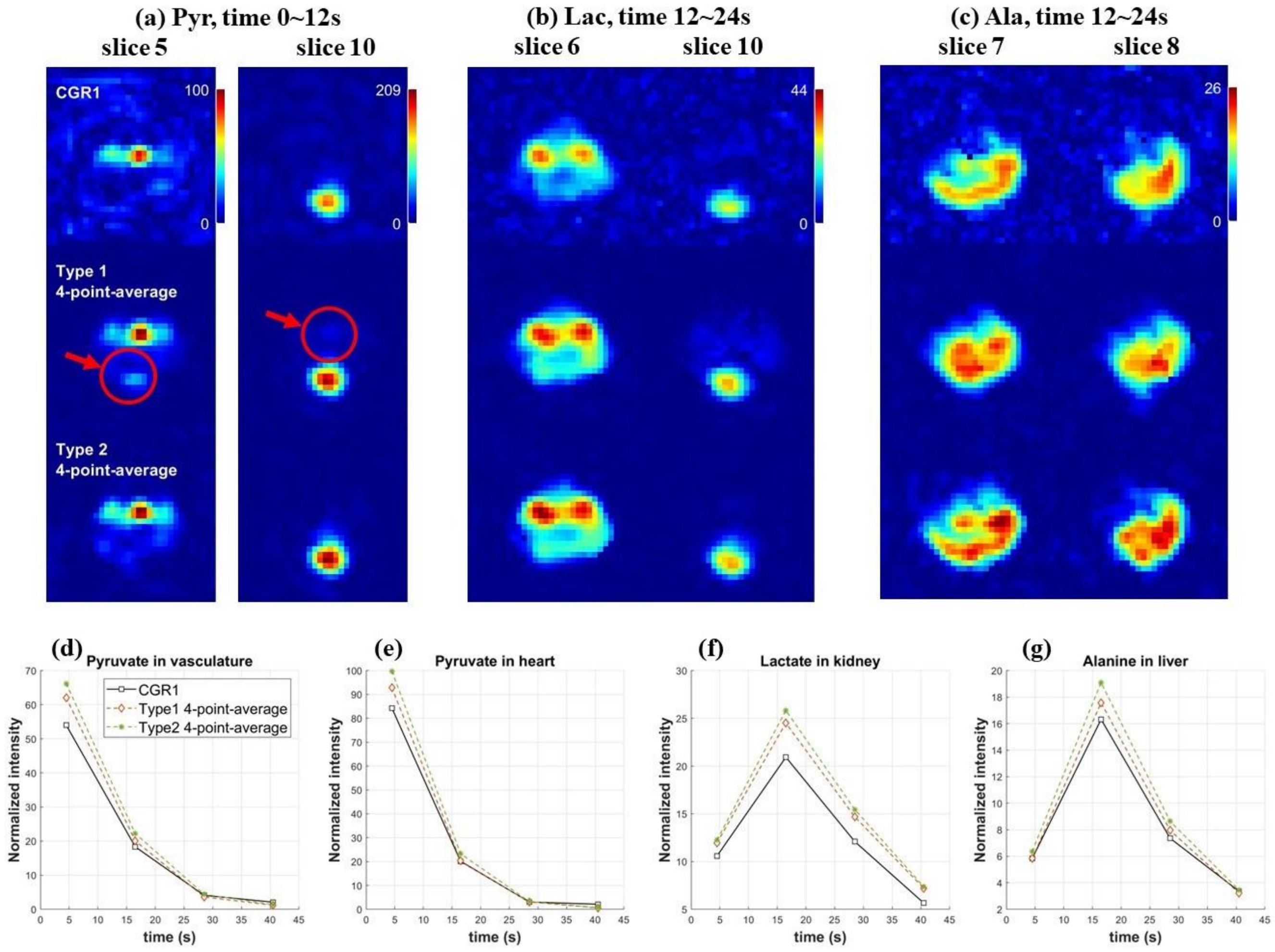

Figure 5-5, Non-accelerated (R=1) images from LLS reconstruction are generated through averaging 4 maps of spectra corresponding to a fully sampled block and compared to the CGR1 images to identify artifacts introduced during the LLS reconstruction. **(a)** Slice 5 (vasculature) and slice 10 (heart) of the pyruvate images. **(b)** Slice 6 (kidney) and slice 10 (heart) of the lactate images. **(c)** Slice 7 (liver) and slice 8 of the alanine images. **(d-g)** Dynamic curves for the non-accelerated images of the corresponding ROIs.

The progressive update for the three stages can be visualized in Figure 5-6. From stage 1 to stage 2, artifacts are significantly reduced for the output result L+S. From stage 2 to 3, minor corrections are made for some low intensity components. Correspondingly, intensity of the residual image M_{res} keeps decreasing, as the corresponding L+S image achieves better data consistency.

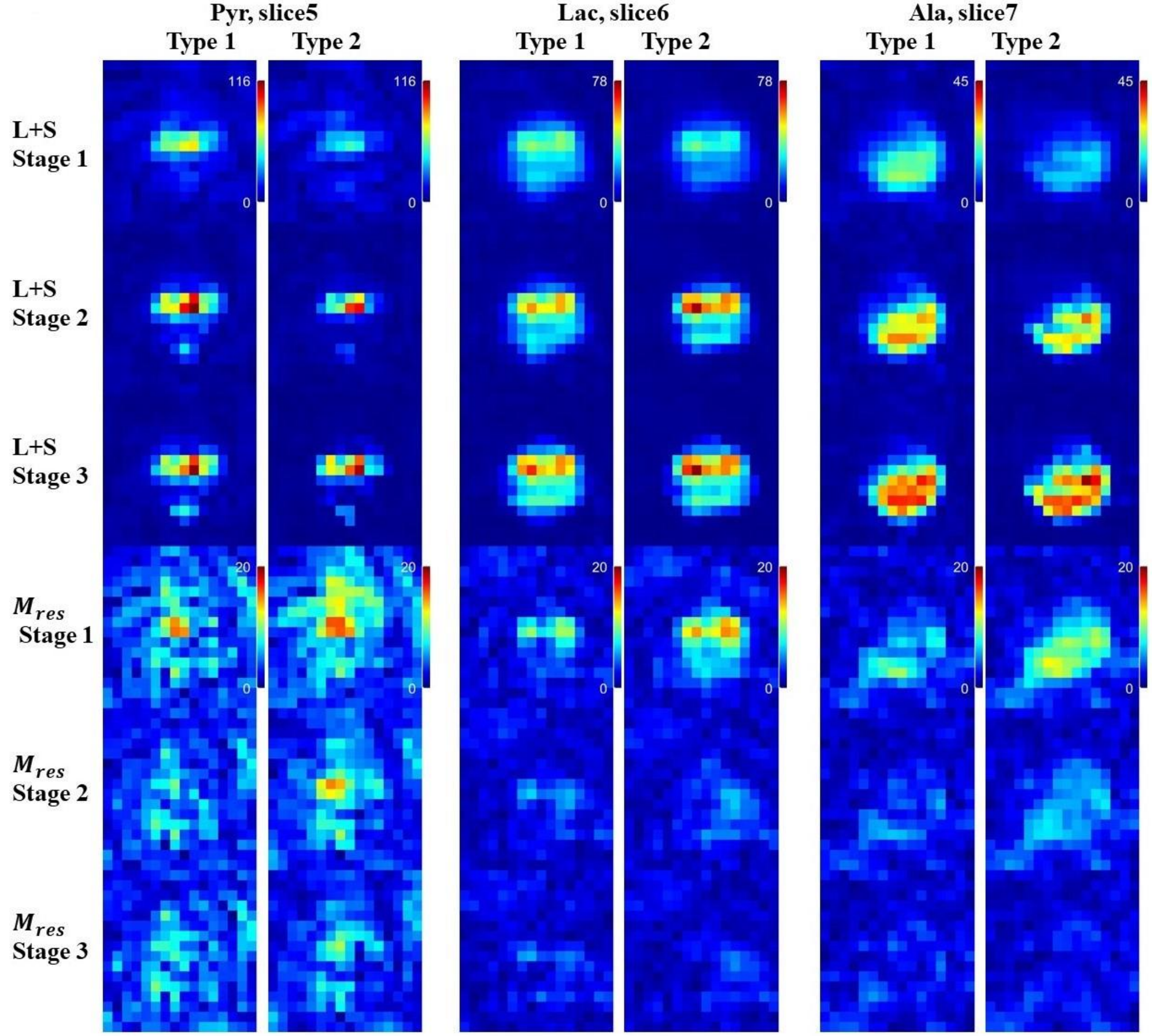

Figure 5-6 1st - 3rd row: Magnitude image of peak frequency bin in the map of spectra at selected slice and time point after each stage of LLS reconstruction. 4th – 6th row: Residual image of the corresponding frequency bin after each stage of LLS reconstruction.

The effectiveness of artifact removal is assessed by artifact-to-mean body signal ratio (ASR), defined by mean image intensity outside mouse body normalized to the mean image intensity inside the body (region determined through anatomical information from ^{1}H MRI). Figure 5-6(b) shows the ASR for the three metabolites measured for the accelerated image for a range of time points where there is sufficient SNR to quantify the mean body signal. The accelerated image at the entry of the iterative reconstruction, CGR4, produces artifacts between 40% to 100% of the body signal. Both types of LLS have much lower artifact magnitude between 5% to 30%, with type 2 performing slightly better than type 1. Measured ASR for the dynamic image joining all the time points is provided in Table 5.2. Reconstructed on the fully sampled k-space data, CGR1 result still suffers from severe swirl artifacts. Artifact magnitude for CGR4 remains high due to under-sampling. Both types of LLS significantly reduce the artifacts level by a factor of 5 approximately. Artifacts in pyruvate images is higher for LLS with type 1 configuration compared with type 2 configuration due to the artifact component seen in the location of heart in the vasculature slice, which is considered outside of the mouse body from the ^{1}H MRI overlay.

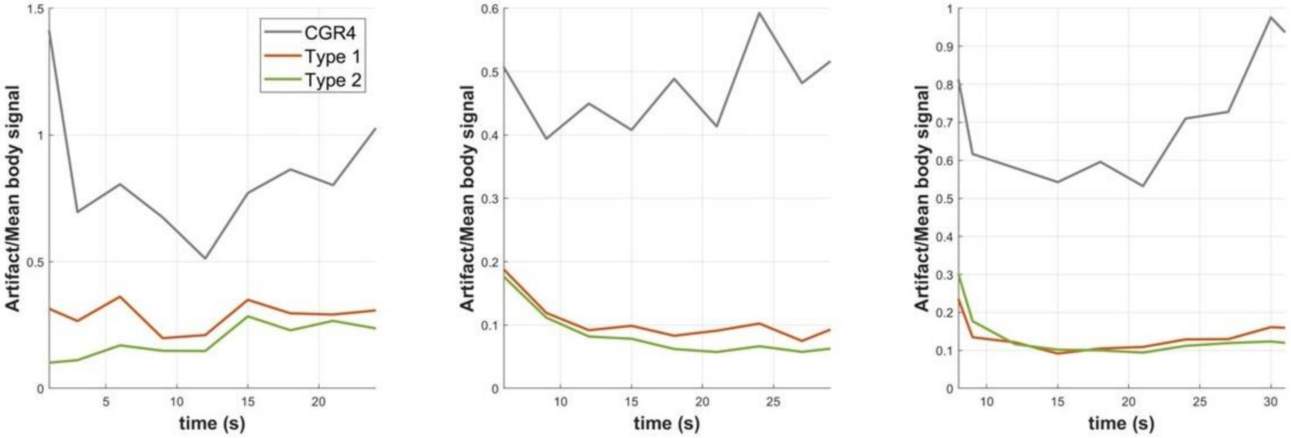

(a) pyruvate **(b) lactate** **(c) alanine**

Figure 5-7 Artifact-to-mean body signal ratio for **(a)** Pyruvate at slice 5 **(b)** Lactate at slice 6 **(c)** Alanine at slice 7. Ratios are plotted in selected time window where there is sufficient SNR to quantify the mean body signal.

Artifact/ mean body signal	CGR1	CGR4	Type 1 LLS	Type 2 LLS
Pyr	1.2723	0.8535	0.1619	0.1034
Lac	0.4929	0.5402	0.1084	0.0827
Ala	0.7891	0.8122	0.1613	0.1468

Table 5.2 Artifact-to-mean body signal ratio measured for the dynamic images of each metabolite at the selected slice over all time points.

5. 4 Conclusion

With highly under-sampled data acquisition and LLS reconstruction, temporal resolution of 3D spCSI is enhanced from 5 frames/minute to 20 frames/minute without sacrificing spatial/spectral resolution. Type 2 LLS is preferred over type 1 LLS for image data with distinct spatial distribution along slice dimension.

Chapter 6 : Investigating the Origin of the 13C Lactate Signal in the Anesthetized Healthy Rat Brain In Vivo after Hyperpolarized [1-13C]Pyruvate Injection

The following chapter is partially adapted from: "Investigating the origin of the 13C lactate signal in the anesthetized healthy rat brain in vivo after hyperpolarized [1-^{13}C]pyruvate injection." NMR in Biomedicine 37.3 (2024): e5073.

6. 1 Abstract

The goal of this study was to investigate the origin of brain lactate signal in the healthy anesthetized rat after injection of hyperpolarized (HP) [1-^{13}C]pyruvate (Pyr). Dynamic 2D spiral chemical shift imaging with flow-sensitizing gradients revealed reduction in both vascular and brain Pyr while no significant dependence on the level of flow suppression was detected for Lactate (Lac). These results support the hypothesis that the HP metabolites predominantly residing in different compartments in the brain, i.e., Pyr in the blood and Lac in the parenchyma. Data from high-resolution metabolic imaging of [1-^{13}C]Pyr further demonstrated that Lac detected in brain was not from contributions of vascular signal due to partial volume effects. These data do not support the hypothesis that Lac observed in the brain after Pyr injection was generated in other organs and then transported across the blood-brain barrier (BBB). Together the presented results provide further evidence that even in healthy anesthetized rats the transport of HP Pyr across the BBB is sufficiently fast to permit detection of its metabolic conversion to Lac within the brain.

6. 2 Introduction

Metabolic imaging of HP ^{13}C-Pyr has been applied in multiple rodent studies to investigate brain metabolism in healthy animals[25,36–39] and disease models such as brain tumor[40–45], traumatic brain injury[46,47], and neuroinflammation[48]. In these studies, conversion of the injected pyruvate into lactate (Lac) was used to provide information on glycolytic brain metabolism. However, a recent report by Miller et al. [49] concluded “that earlier reports of whole-brain metabolism in anaesthetized animals may be confounded by partial volume effects and not informative enough for translational studies" after the authors failed to observe HP ^{13}C-lactate in the brain of healthy rats nor in normal-appearing brain tissue of animals with brain tumor. The goal of this study was to further investigate the origin of the lactate signal in the anesthetized rat brain after injection of HP [1-^{13}C]pyruvate. Previous study by Hurd et al.[37] demonstrated that metabolite kinetics in dynamic metabolic imaging of HP [1-^{13}C]Pyr are consistent with Pyr-to-Lac conversion being limited by blood-brain barrier (BBB) transport. Consequently, Pyr and Lac predominantly would originate from different compartments within the brain, i.e., Pyr in the blood and Lac in the parenchyma. In this study, we used a dynamic 2D spiral chemical shift imaging sequence that was modified to include a bipolar gradient pulse prior to data acquisition to suppress signal components from flowing spins[50,51]. This approach has been successfully applied in abdominal and cardiac imaging of HP Pyr to suppress the large vascular signal of the injected substrate[52–54]. The method was used to test the hypothesis that signal from brain Lac will be less affected by flow suppression than Pyr. The experiments with flow suppression after HP [1-^{13}C]Pyr injection were complemented by high-resolution metabolic imaging as well as dynamic imaging with LLS reconstruction as described in Chapter 4.

6. 3 Methods

6. 3. 1 Animal handling and sample preparation

Five healthy male Wistar rats (240-284-g body weight) were included in the experiments. Animals were anesthetized with isoflurane (1.5-2% in 1-1.5-L/min O_2) during tail vein catheterization and throughout the imaging session. Samples consisting of ~60 mg [1-^{13}C]pyruvic acid and 15 mM trityl radical were hyperpolarized for at least 2.75 hours in a 5-T GE SpinLab as in previous study[47]. The pyruvic acid was then quickly dissolved in water and neutralized with sodium hydroxide to produce a target solution of 125-mM [1-^{13}C]Pyr with pH around 7 and a liquid-state polarization of 30-40% at the time of dissolution.

6. 3. 2 Hardware and acquisition parameters

The experiments were performed on a clinical 3T GE 750w MR scanner and a dual-tuned ^{1}H-^{13}C quadrature RF coil for both excitation and signal reception. The gradient system had a maximum amplitude of 33 mT/m and a slew rate of 120 mT/m/ms.

In order to add flow suppression, the existing dynamic 2D spCSI sequence[55] was modified by inserting a bipolar trapezoidal gradient of variable duration 2W between RF excitation and the spiral readout gradients (Figure 6-1). In the presence of the bipolar gradient along the x-axis, signal from flowing spins (assuming flow velocity in x-axis only) will be attenuated due to the phase accumulation according to the voxel-dependent velocity profile $v(x)$ by a factor

$$\alpha_{sup} = 1 - \int \exp\left(-i\gamma m_1 v(x)\right) dx \quad [Eq. 6.1]$$

Here, γ is the gyromagnetic ratio and m_1 is the first moment of the bipolar gradient. The amplitude of gradient was 30 mT/m along the *z* direction of the flow-suppression and 23.3 mT/m along x and y direction. In order to achieve different levels of flow suppression, each animal was scanned with W of 0 ms, 6 ms, and 9.568 ms (in the following referred as 9.6 ms) in randomized order. These durations correspond to first moments m_1 of 0 mT·ms^2/m, 773 mT·ms^2/m, and 2025 mT·ms^2/m along x-axis and y-axis, 0 mT·ms^2/m, 995 mT·ms^2/m, and 2607 mT·ms^2/m along z-axis, respectively. The suppression efficiency α_{sup} for the gradients used in this study as a function of flow velocity shown in Figure 6-2. The corresponding echo times (TEs), i.e., start of the spiral gradients and data acquisition, were 5.296 ms, 16.0 ms, and 23.136 ms. These TEs were chosen so that each dataset included data from 19 spiral gradient echoes starting at a TE of 23.136 ms. The remaining sequence parameters were: 40-mm field-of-view (FOV), 2.5×2.5-mm^2 nominal in-plane resolution, 8 spatial interleaves, 280-Hz spectral width (SW). For four animals the data were acquired using a constant 5.625° flip angle excitation for 16 data sets every 3 s starting 6 s after start of the pyruvate injection. For one animal (rat 2) the data acquisition started 9 seconds after start of the pyruvate injection acquiring six data sets every 3 s with a variable flip angle scheme[56] ending in 90° applied across the total 48 individual excitations. One animal (rat 5) underwent a second MRI session after one week to acquire metabolic imaging data at higher resolution without additional flow suppression (36-mm FOV, 24×24 matrix size, 24 spatial interleaves, 24 spiral echoes at a 264-Hz SW, TE = 2.5 ms, 3 s temporal resolution, 5.625° constant flip angle, 16 time points starting 15 s after start of injection. ^{1}H multi-slice 2D axial dual TE ^{1}H-FSE images were obtained for overlay of the metabolic images.

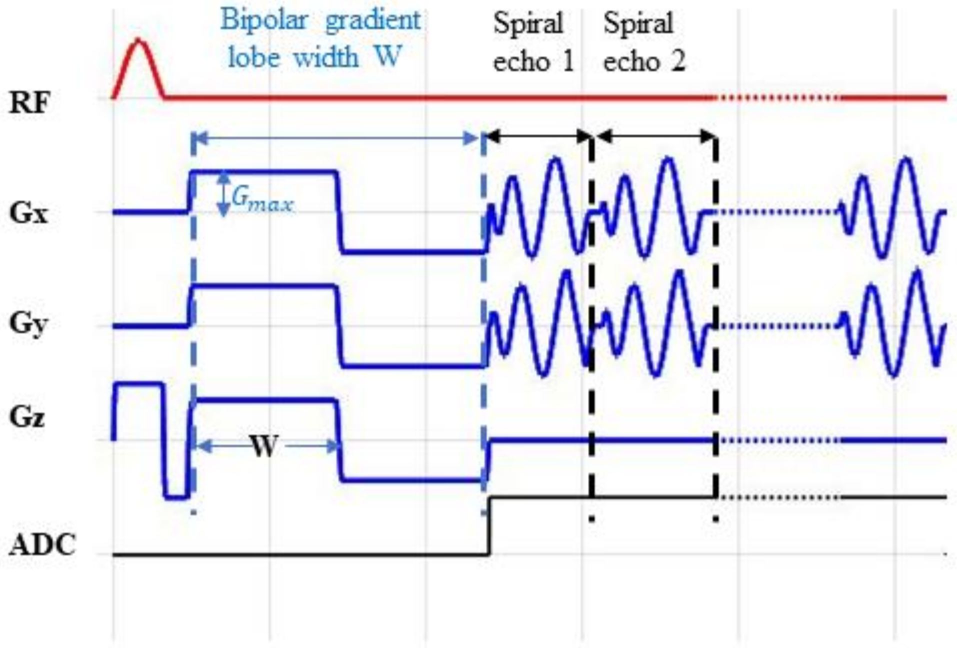

Figure 6-1, Schematic diagram of spiral chemical shift imaging sequence with addition of bipolar gradients for flow suppression.

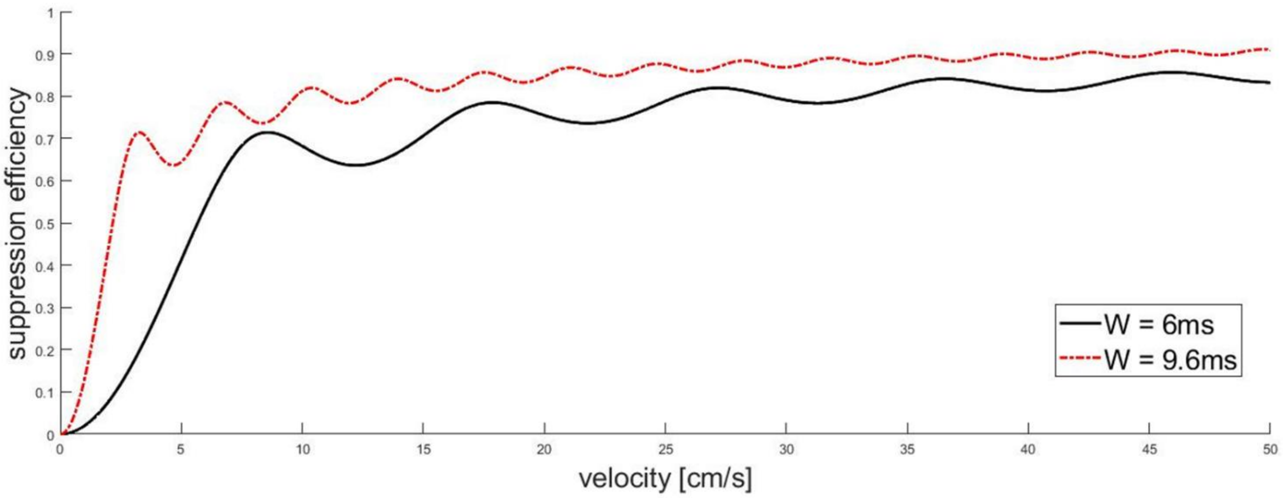

Figure 6-2, Suppression efficiency a function of peak blood velociy for bipolar gradients with the same duration and strength as applied in the in vivo experiments assuming a parabolic velocity profile across the vessel for flow only along the z-axis.

6. 3. 3 Data processing and statistical analysis

Time-averaged metabolic maps were reconstructed with CSI reconstruction as mentioned in Chapter 2. When comparing data sets with different levels of flow suppression, only the k-space data of the 19 echoes starting at TE of 23.136 ms were used in order to remove differences in T_2-weighting. For each experiment, three regions of interest (ROIs) – brain, vascular, and muscle – were drawn based on the metabolic maps and ^{1}H images. The muscle region was selected based the anatomical structure corresponding to mouse tongue and the observation of alanine signal from the metabolic maps.

The effects of flow-suppression were analyzed using a repeated measures analysis of variance (ANOVA) with the Greenhouse-Geisser correction for lack of sphericity. Follow-up between group differences were conducted with Tukey's honestly significant difference (HSD) test. For each dissolution, variations in the level of polarization and concentration of the final solution can affect the absolute signal intensity of pyruvate and its metabolic products, and hence, mask potential effects of flow attenuation. In order to remove the effect of differences in polarization, the analysis was repeated with each data set normalized to the respective muscle Ala. Additionally, the same ANOVA was applied to the concentration of the Pyr solution for each injection estimated from the amount of pyruvic acid in the sample vial and the total volume of the final solution. The statistical analysis was performed using the Real Statistics Resource Pack add-in to Microsoft Excel. Investigators were not blinded.

Dynamic 2D images from one of the animals scanned with W=0 (no flow suppression) were first reconstructed with CSI reconstruction. The same data is reconstructed with LLS iterative reconstruction at original temporal resolution to reduce the background noise for better visualization of the dynamic maps. The LLS reconstruction is conducted in a similar way as described in Chapter 4, with $\lambda_L = 0.075, \lambda_{Si} = 0.1$, 50 iterations, and block size 1 on frequency dimension.

6. 4 Results

Figure 6-3a shows the ^{1}H MRI indicating the slice location and position of ROIs in brain, vasculature, and tongue muscle. Metabolic maps of Pyr and Lac with different levels of flow suppression from a representative animal are shown in Figure 6-3b and 6-3c. The metabolic maps for Pyr clearly show the signal decrease in the vascular and, to a lesser degree, brain ROIs with increasing level of flow suppression. At the same time, no systematic decrease in brain Lac is discernable.

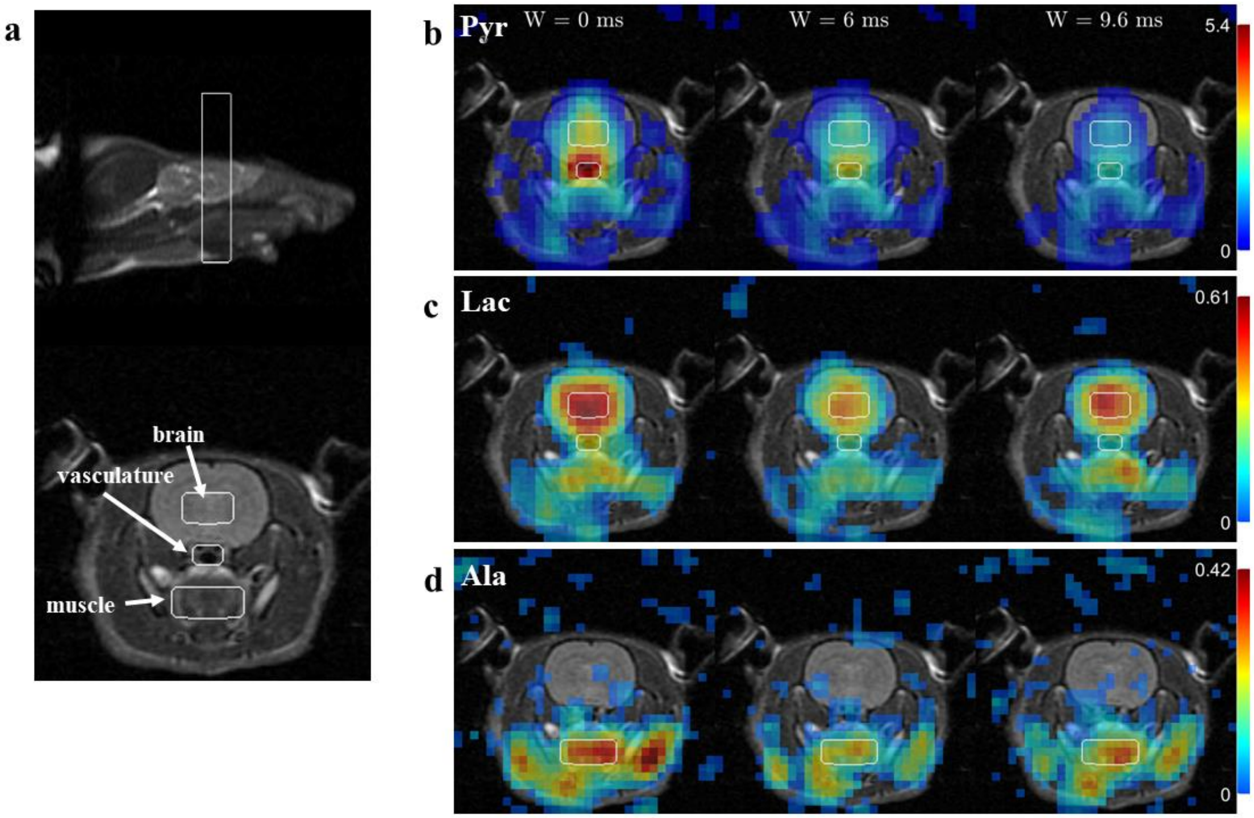

Figure 6-3 ^{1}H MRI and time-averaged metabolic maps at three levels of flow suppression (W = 0 ms, 6 ms, 9.6 ms) from a representative animal. **(a)** ^{1}H MRI indicating the slice location and ROIs in brain, vasculature, and tongue muscle. Metabolic maps of **(b)** Pyr (signal threshold of the metabolic maps 8%), **(c)** Lac (signal threshold 20%), and **(d)** Ala (signal threshold 20%). Pyr intensity in the vascular ROI decreased significantly with increasing level of flow suppression. Less variation was observed for brain Lac and muscle Ala.

The quantitative analysis for both Pyr and Lac from vascular and brain ROIs are shown in Fig 2. Vascular Pyr decreased from 4.0 ± 1.7 (mean ± standard deviation) at W=0 to 2.7 ± 0.6 at W=6 ms and to 1.6 ± 0.5 at W=9.6 ms. The ANOVA revealed a statistically significant difference of the Pyr intensity between at least two W values (F(1.52, 6.08)=7.13, p=0.0295). Follow-up tests showed significant differences between W=0 and W=9.6 ms (p=0.0134). However, only a trend for a similar dependence on flow suppression was found for Pyr in the brain ROI, which decreased from 2.1 ± 1.0 at W=0 to 1.6 ± 0.6 at W=6 ms and 1.0 ± 0.3 at W=9.6 ms (F(1.45, 5.80)=5.14, p=0.0583). No significant dependence on the level of flow suppression was detected for Lac in brain (0.5 ± 0.2 at W=0, 0.4 ± 0.1 at W=6 ms, 0.4 ± 0.1 at W=9.6 ms; F(1.48, 5.93)=0.32, p=0.6756) or vascular ROIs (0.43 ± 0.19 at W=0, 0.33 ±

0.09 at W=6 ms, 0.22 ± 0.05 at W=9.6 ms; F(1.57, 6.29)=3.8, p=0.0865). No difference in concentration of the injected Pyr solution was found (122 ± 15 mM at W=0, 115 ± 12 mM at W=6 ms, 131 ± 38 mM at W=9.6 ms; F(1.42, 5.69)=0.50, p=0.57).

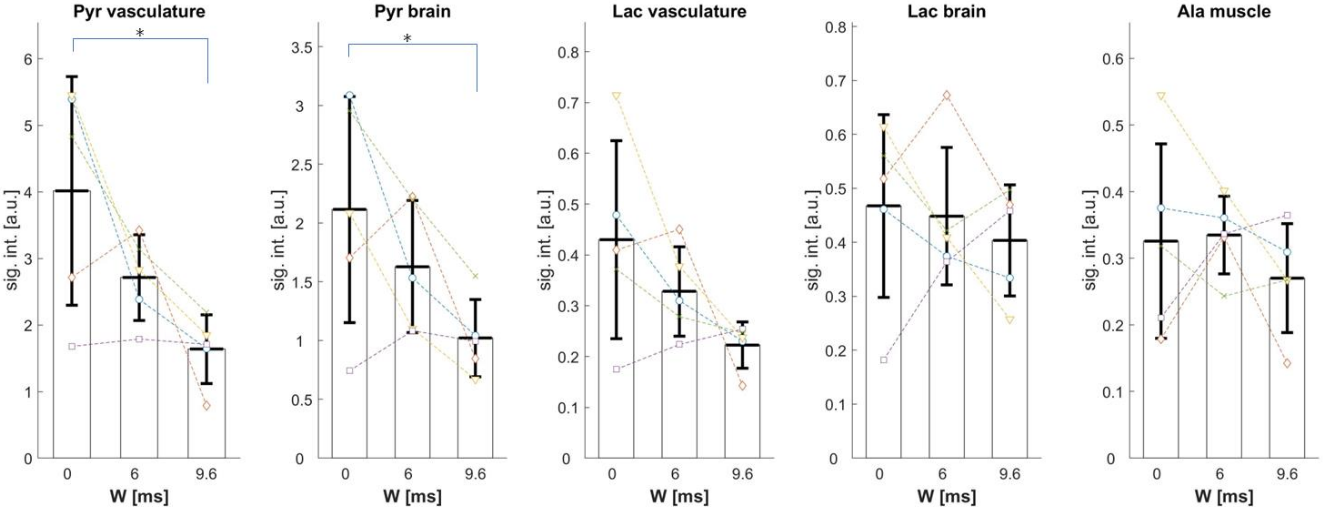

Figure 6-4 Mean and standard deviation (n=5) of time-averaged Pyr, Lac, and Ala in vascular, brain, and muscle ROIs. Signal intensities are in absolute units, i.e., without any normalization, with each metabolite on the same scale. Data points for each individual animal are shown in dashed lines. Pyr intensity in vasculature and brain was significantly lower with high flow-suppression (W = 9.6 ms) compared with no suppression (W = 0 ms). Differences in vascular and brain Lac as well as muscle Ala were not statistically significant for each pair of W values. *Indicates $p < 0.05$ for correlated samples.

Variation in substrate polarization could mask effects on the metabolite signal. As the SpinLab was designed for clinical applications, it does not provide a reliable measure of polarization for sample volumes as small as used in this preclinical study. Ala generated in the tongue muscle tissue can be considered stationary compared to signal in blood. As it did not show any dependence on flow suppression (0.3 ± 0.1 at W=0, 0.3 ± 0.05 at W=6 ms, 0.3 ± 0.1 at W=9.6 ms; F(1.60, 6.40)=0.74, p=0.4832) it was used as a normalization factor to remove effects of varying polarization. Metabolic maps after normalization to muscle Ala are shown in Figure 6-5 and statistical analysis results shown in Figure 6-6. In addition to vascular Pyr (12.5 ± 3.3 at W=0, 8.4 ± 3.1 at W=6 ms, to 6.1 ± 2.0 at W=9.6 ms; F(1.66, 6.64)=15.86, p=0.0036), brain Pyr also showed a significant effect of flow suppression (6.9 ± 3.0 at W=0, 5.2 ± 2.6 at W=6 ms, to 4.1 ± 1.7 at W=9.6 ms; F(1.76, 7.03)=8.46, p=0.0149). Follow-up tests showed significant differences between W=0 and W=6 ms (p=0.0181) as well as between W=0 and W=9.6 ms (p=0.0014) for vascular Pyr and between W=0 and W=9.6 ms (p=0.0087) for brain Pyr. As in the case of absolute metabolite intensities, no significant dependence on the level of flow suppression was detected for brain Lac (1.6 ± 0.8 at W=0, 1.4 ± 0.5 at W=6 ms, 1.7 ± 1.0 at W=9.6 ms; F(1.33, 5.33)=1.38, p=0.31). Although not statistically significant a trend of decreasing vascular Lac was observed (1.4 ± 0.5 at W=0, 1.0 ± 0.3 at W=6 ms, 0.9 ± 0.1 at W=9.6 ms; F(1.09, 4.37)=6.29, p=0.0598).

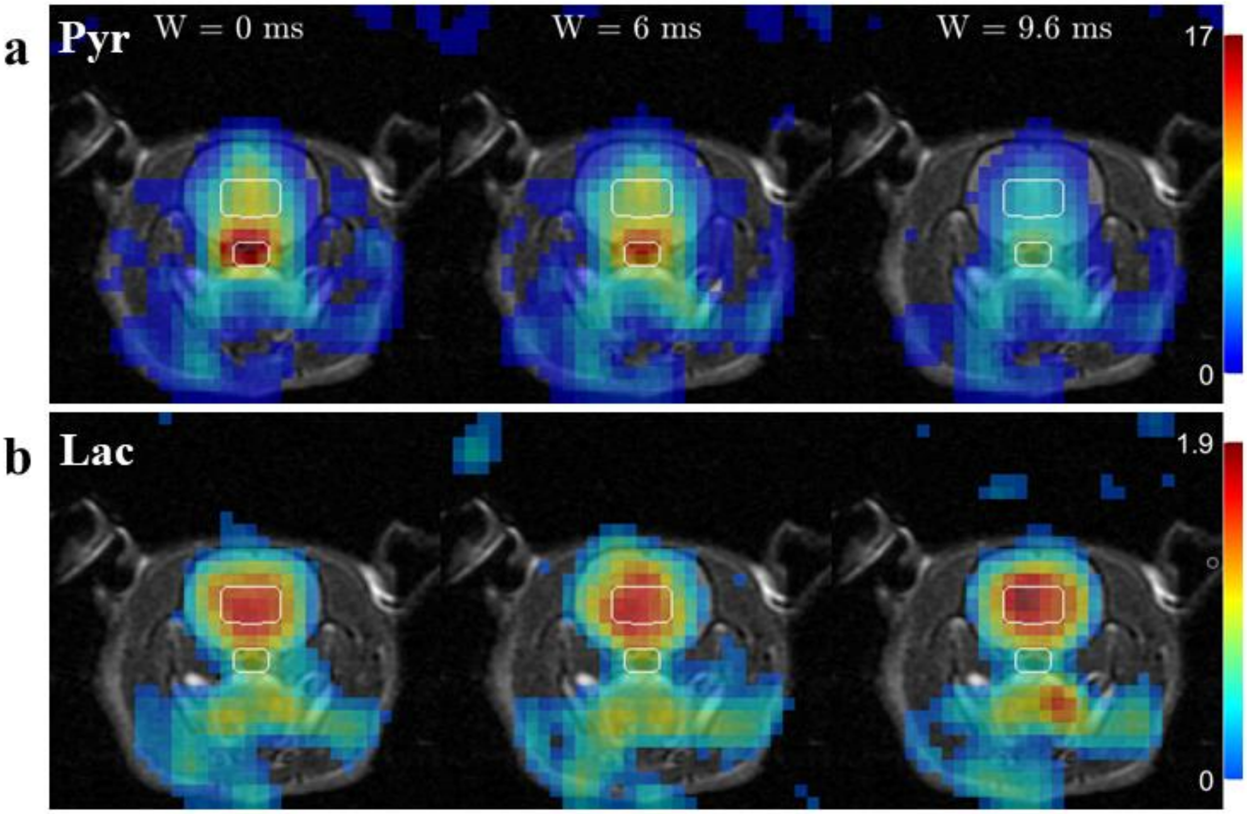

Figure 6-5 Time-averaged metabolic maps for **(a)** Pyr and **(b)** Lac from the animal shown in Fig. 1 after normalization to mean Ala intensity in muscle ROI. After normalization, the trend of decreasing vascular Pyr with increasing level of flow suppression was more pronounced, while even less variation in brain lactate can be observed among three levels of suppression.

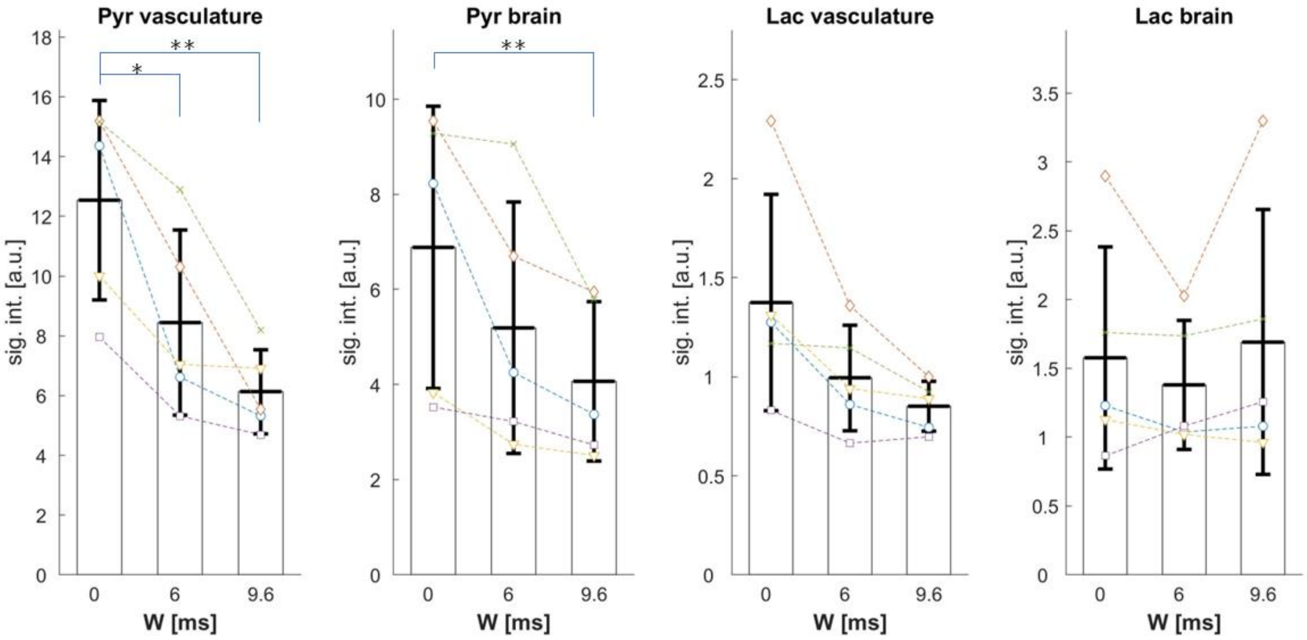

Figure 6-6 Mean and standard deviation (n=5) of time-averaged Pyr and Lac in vascular and brain ROIs. Signal intensity is normalized to the mean Ala intensity in muscle ROI for each imaging experiment. Data points for each individual subject are shown in dashed lines. Significant differences are found in vascular Pyr (W = 9.6 ms vs W = 0 ms and W = 6 ms vs W = 0 ms) as well as for brain Pyr vs (W = 9.6 ms vs W = 0 ms). Neither differences in vascular nor brain Lac were statistically significant for any pair of W values. *Indicates $p < 0.05$ and **indicates $p < 0.01$ for correlated samples.

From high resolution scan we obtained metabolic maps of Pyr and Lac as well as Lac-to-Pyr ratio acquired at the higher nominal in-plane resolution of 1.5 mm. Time-averaged Pyr and Lac images are shown in Figure 6-7(a) and 6-7(b). The high-resolution images show clearly different signal distributions for Pyr and Lac. The Pyr maps have the highest intensity in the vascular structures such as the arteries of the Circle of Willis and, to a lesser degree, the sagittal sinus. Only very little Pyr is detected in the brain. In contrast, while Lac is highest in the tongue it also shows high signal throughout the whole brain.

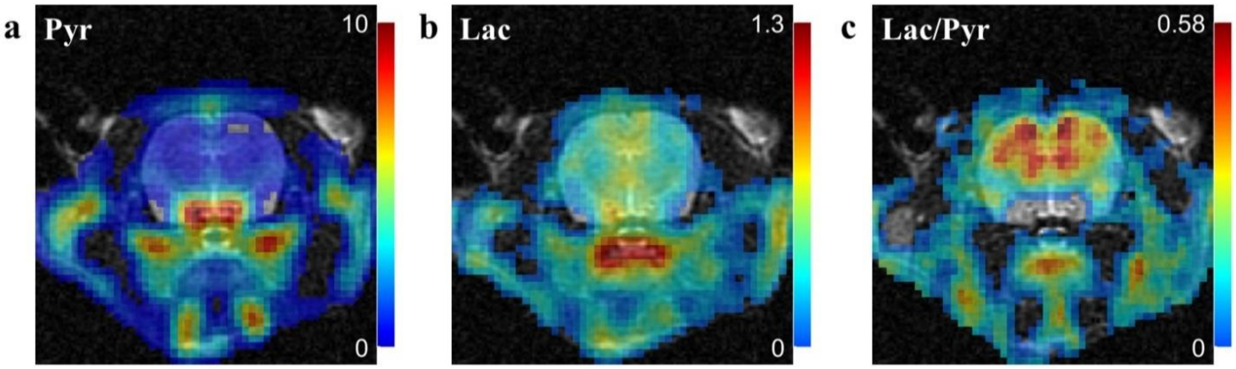

Figure 6-7 High-resolution 2D spCSI of healthy rat brain after a single [1-^{13}C]Pyr injection. Time-averaged metabolic maps of **(a)** Pyr (signal threshold 8%), **(b)** Lac (signal threshold 20%), and **(c)** Lac-to-Pyr ratio masked on an ROI with pyruvate intensity threshold of 12% and ratio threshold larger than 0.11. The highest Pyr signal was observed in the major vascular structures (Circle of Willis and sagittal sinus) whereas the high Lac signal was detected in the tongue muscle as well as in the brain. High Lac/Pyr ratio throughout the brain provides more evidence that the lactate signal is from the brain itself rather than due to partial volume effects from major vessels.

Dynamic images of the scan without flow-suppression are displayed in Figure 6-8. With LLS reconstruction, background noise is significantly reduced, facilitating the distinction in the dynamics between Pyr and Lac. Pyruvate in the vasculature reached peak intensity at earlier time points and then quickly decayed, while Lac in brain appeared approximately 3 s after the arrival of substrate Pyr bolus, and its intensity remained high for several time frames.

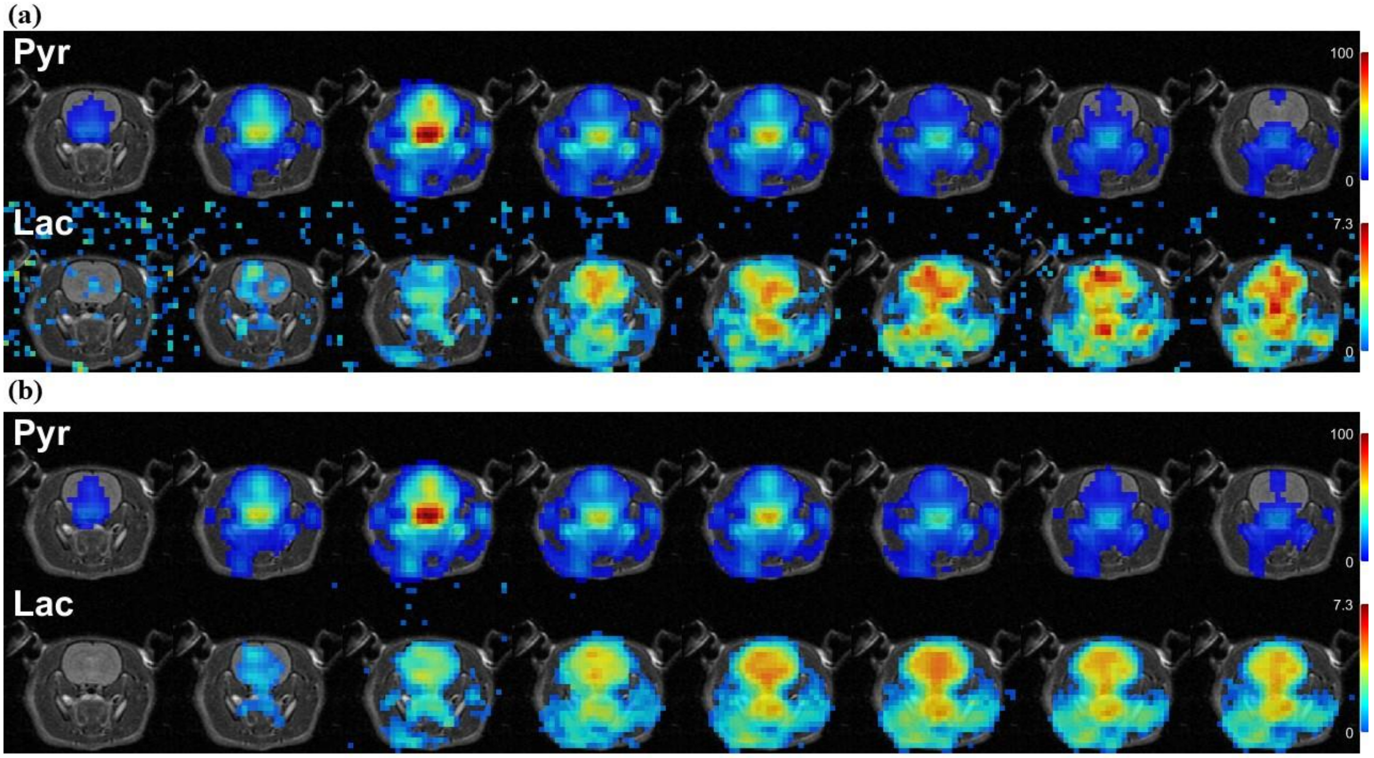

Figure 6-8 Dynamic images for scan without flow suppression at 3-s temporal resolution starting at 6s after start of injection **(a)** Using CSI reconstruction **(b)** Using LLS reconstruction without acceleration. With less interference from background noise, dynamic features can be clearly identified for the substrate pyruvate and the product lactate.

6. 5 Discussions

The presented data from the experiments with flow-sensitizing gradients demonstrate distinctively different signal behavior for Pyr and Lac in brain and vascular ROIs that cannot be caused by any systematic differences in the substrate concentration. Pyr in the vascular as well as in the brain ROI decreased with increase in flow suppression. The mean velocity of blood in the interior carotid arteries is on the order of 40 cm/s[56–58] while in the capillaries it is lower by two orders of magnitude[59,60]. Based on these estimates together with the suppression factor in Figure 6-2, metabolite signal in the arteries should be suppressed by 30-50%, consistent with our experimental results. Although, at least for the case of W = 9.6 ms, even in small vessels with velocities as low as 0.52 cm/s a suppression factor about 20% could be achieved. The fact that brain Pyr was also affected by flow suppression was most likely predominantly due to partial volume effects from vascular signal imaged at limited resolution, to be discussed below. However, it is also consistent with transport across the BBB being the rate-limiting step in the conversion of HP Pyr to Lac[37], i.e., any Pyr that has crossed the BBB is quickly converted to Lac, and Pyr signal detected in a brain ROI is predominantly from the blood pool, hence, more sensitive to flow-suppression gradients. In contrast, no change in brain Lac was detected with increasing levels of flow suppression. These results suggest that Lac and Pyr signals in brain predominantly reside in different compartments providing further evidence that the majority of the Lac in brain was a consequence of cerebral metabolism.

Comparison of the metabolic maps acquired at low and high in-plane resolution reveals significant partial volume effects for Pyr in the low-resolution image. High signal in vascular structures superior and posterior to the brain, which were better resolved in the high-resolution data, contributed to the signal in the brain ROI in the low-resolution image. At the same time, Lac has the same level for brain and vasculature in the high-resolution image, suggesting that brain Lac in low-resolution image is mostly not from the partial volume effects of the vascular structures superior and posterior to the brain.

Dynamic image with reduced background noise reveals the distinct dynamic patterns for Pyr in vasculature and Lac in brain. Signal of the substrate Pyr was highest in the vasculature and decayed quickly with little signal appearing in the brain. In contrast, high signal of the product Lac was detected in the brain and its intensity remained high for several time frames. Therefore, it is rather unlikely that the Lac observed in the brain after Pyr injection was generated in other organs such as the heart and then transported across the BBB into the brain.

6. 6 Conclusion

The presented results provide further evidence that even in healthy anesthetized rodents the transport of HP Pyr across the BBB is sufficiently fast to permit detection of its metabolic conversion within the brain when using appropriate acquisition protocols. Therefore, metabolic imaging of HP Pyr is a viable noninvasive tool to probe rodent brain pyruvate metabolism in preclinical studies.

Chapter 7 : Supplementary data

7. 1 Additional data for 2D spCSI with Low Rank Plus Sparse Reconstruction

A second imaging experiment similar to the procedures described in section 4.2.4. was performed on the same animal. The second 2D spCSI acquisition used the same k-space trajectory and random permutation of the interleaves as described in section 4.2.4., but it utilized a progressive flip angle RF excitation scheme with 10 fully sampled blocks, 240 excitations for a total scan time of 30 seconds. Flip angle θ_i at the i_{th} excitation follows the formula as:

$$\theta_i = \tan^{-1}(\frac{1}{\sqrt{240 - i}})$$

This aims to achieve a uniformed amount of transverse magnetization for all 240 excitations, under the assumption that the horizontal magnetization pool remains constant throughout the entire scan. Hence, the image intensity for each dynamic point would be at similar scale using the progressive flip angle scheme. In practice, the actual transverse magnetization pool may decrease for substrate metabolite (pyr), and increase for product metabolite (lac, ala) towards the later time points, as a result of the changes in magnetization pool due to metabolic conversion and perfusion into/out of the imaging volume.

The same image reconstruction methods (CGR1, CGR3, GLS and LLS with same $\lambda_L = 0.075, \lambda_S = 0.25$, $\lambda_{Si} = 0.25$, together with the corresponding 3-time point-average) were applied to the second imaging data set. Accelerated dynamic images are shown in Figure 7-1 (a-c). Dynamic curves for the three metabolites in the respective ROIs were characterized in the same fashion as in 4.3.2., shown in Figure 7-1 (d-f). GLS failed to represent the dynamic pattern for lactate and alanine (increasing intensities), distinct from the dominant pyruvate pattern (decreasing intensity). LLS can effectively recover the correct dynamic pattern and reduce the under-sampling artifacts at the same time.

(a) Pyruvate

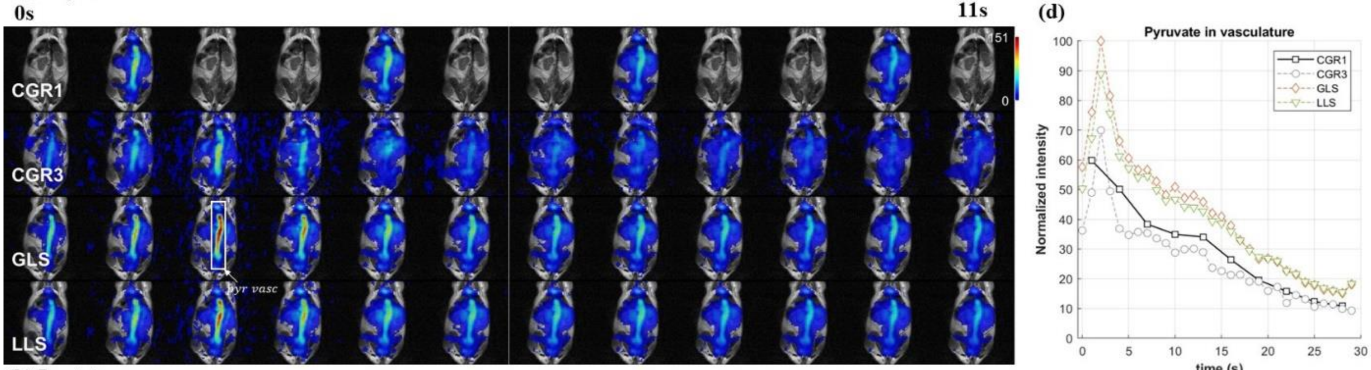

(b) Lactate

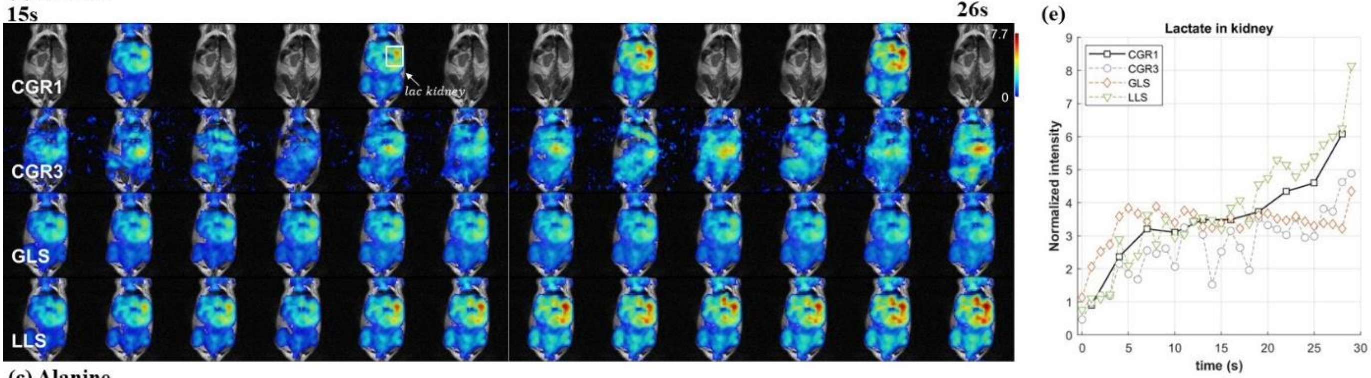

(c) Alanine

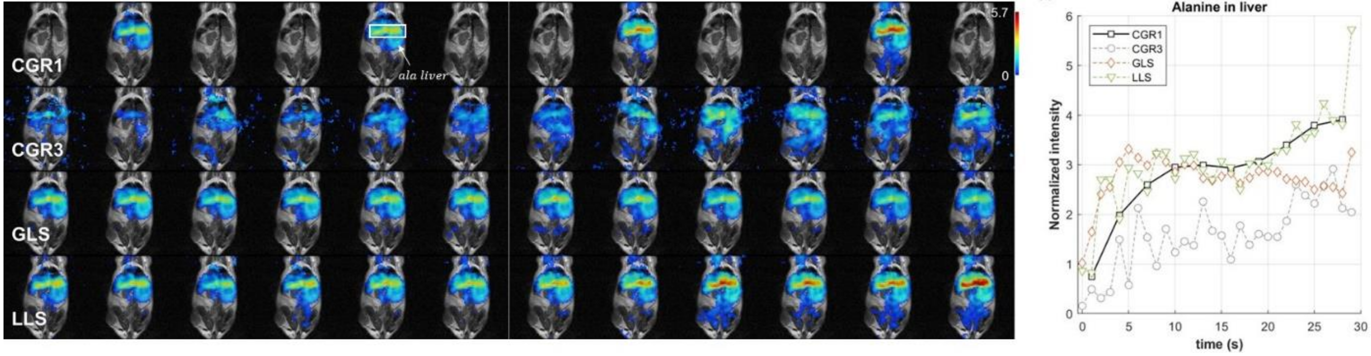

Figure 7-1 Dynamic images of the 2nd 2DspCSI. 1st row of a, b and c, CGR1; 2nd row, CGR3; 3rd row, GLS; 4th row, LLS. **(a)** Pyruvate, starting at 0 second after the start of data acquisition. **(b)** Lactate, starting at 15 seconds. **(c)** Alanine, starting at 15 seconds. **(d-f)** Dynamic curves for the mean intensity in the ROI indicated by the white rectangle of each metabolite.

3-time point-average images at the selected time points are shown in Figure 7-2 (a-c), with corresponding dynamic curves plotted in Figure 7-2 (d-f). The distortion of the lactate and alanine image intensity towards the later time points for GLS is represented in the same way as seen in the previous chapter. LLS images highly resemble CGR1 images, consistent with the results in Figure 4-8.

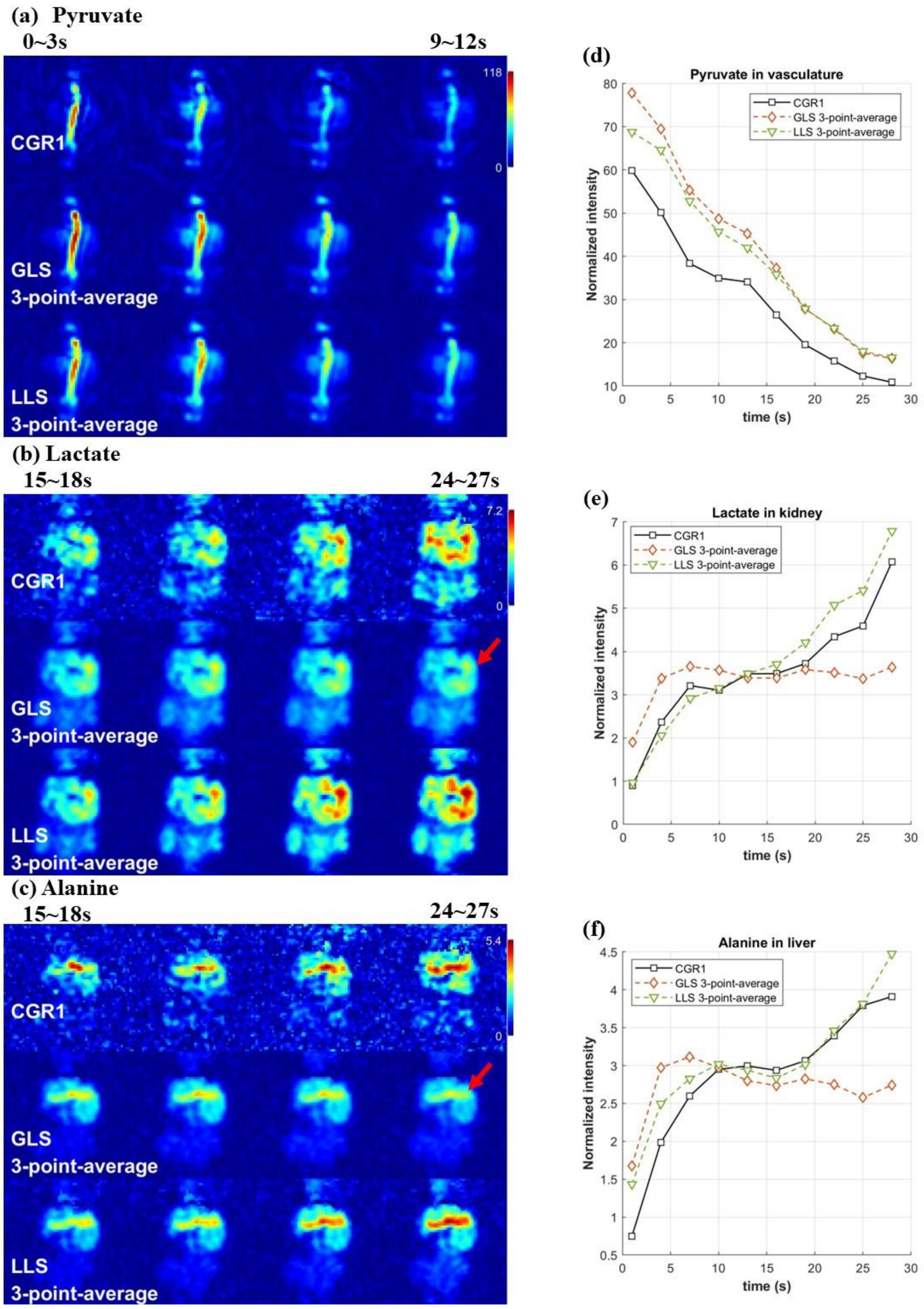

Figure 7-2, Dynamic images reconstructed at 3 seconds temporal resolution for the 2DspCSI acquisition with variable flip angle excitation. 1st row of a, b and c, CGR1; 2nd row, 3-time point-average for GLS; 3rd row, 3-time point-average for LLS. **(a)** Pyruvate, first time point covering data acquired during 0~3 seconds after start of data acquisition. **(b)** Lactate, first time point covering 15~18 seconds. **(c)** Alanine, first time point covering 15~18 seconds. **(d-f)** Dynamic curves for the mean intensity in the ROI of the respective metabolite.

7. 2 Additional data for 3D spCSI with Low Rank Plus Sparse Reconstruction

The same imaging experiment set-up and image reconstruction algorithm/parameters had been applied on three additional mice (mouse IDs m3, m4 and m5) as described in section 5.3.2 for mouse m12. Figure 7-3(b-d) depicts the time-averaged metabolic images with choice of the representative slices for mouse m3. Figure 7-3(e-g) displays the accelerated dynamic images reconstructed with CGR4 and two types of LLS, dynamic curves plotted on the right. Figure 7-4(a-c) displays the non-accelerated dynamic images with CGR1 and 4-time point-average of the two types of LLS, dynamic curves plotted below. Figure 7-5 plots the artifact to mean body signal ratio.

LLS reconstruction results for the additional three animals have similar performance as the results for animal m12 shown in section 5.3.2. In particular, the artifacts seen in the pyruvate vascular slice due to the contamination from the heart slice using Type 1 LLS dependents on the ratio of the heart pyruvate versus vascular pyruvate. The artifact is clearly detectable in m12 (Figure 5-5, $\text{heart:vascular} \cong 2:1$), m3 (Figure 7-4, $\text{heart:vascular} \cong 1.5:1$), and m5 (Figure 7-10, $\text{heart:vascular} \cong 2:1$) and but not observed in m4 (Figure 7-7, $\text{heart:vascular} \cong 1:1$).

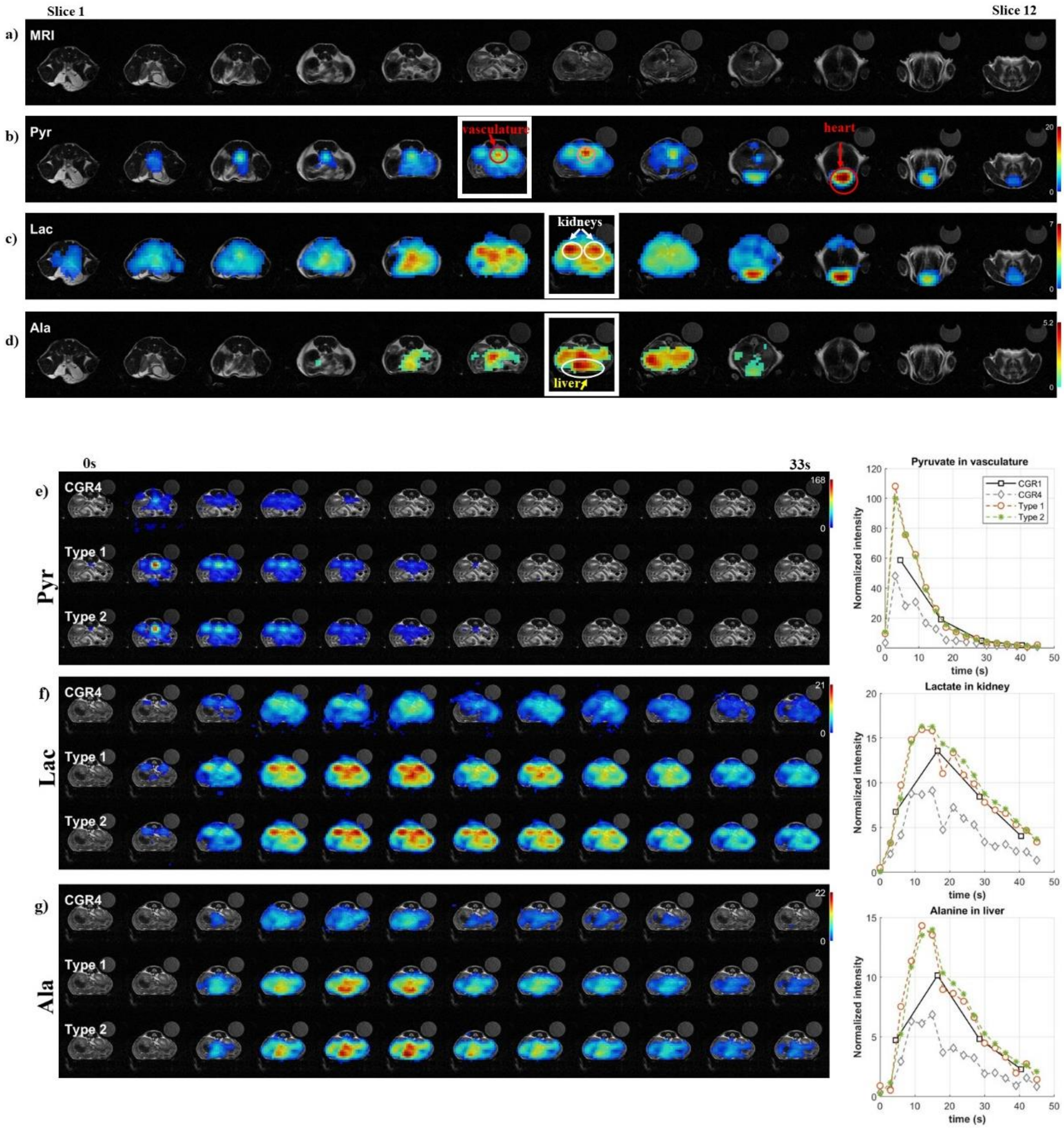

Figure 7-3, Reconstruction results for in vivo imaging of mouse m3. **(a)** ^{1}H MRI for anatomical overlay. **(b-d)** Time-averaged metabolic maps in all slices from reconstruction of the fully sampled k-space data. Arrows point out ROIs. **(e-g)** Accelerated dynamic images at the representative slice. For each metabolite, 12 under-sampled time points starting at 0 seconds after start of data acquisition are presented. Dynamic curves of the non-accelerated images (CGR1) and accelerated images (CGR4, type 1 LLS and type 2 LLS) are plotted on the right.

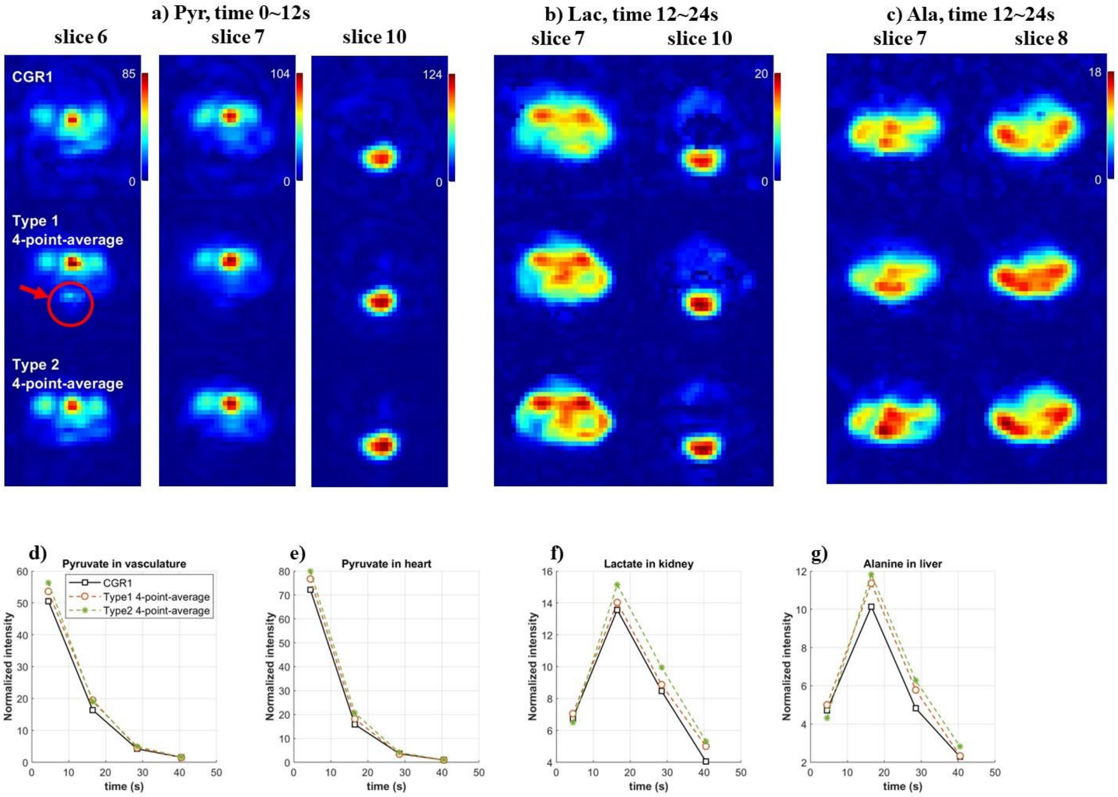

Figure 7-4, Non-accelerated (R=1) images for mouse m3. **(a)** Slices 6, 7 (vasculature) and slice 10 (heart) of the pyruvate images. **(b)** Slice 7 (kidney) and slice 10 (heart) of the lactate images. **(c)** Slice 7 (liver) and slice 8 of the alanine images. **(d-g)** Dynamic curves for the non-accelerated images of the corresponding ROIs.

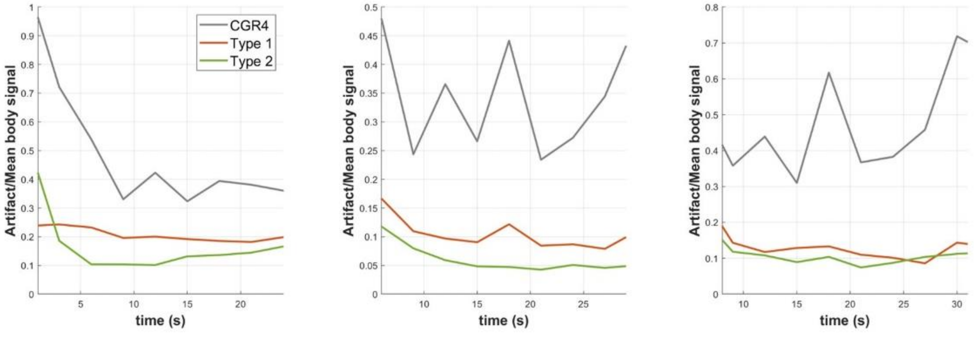

(a) pyruvate **(b) lactate** **(c) alanine**

Figure 7-5, Artifact-to-mean body signal ratio for the three metabolites in selected time window.

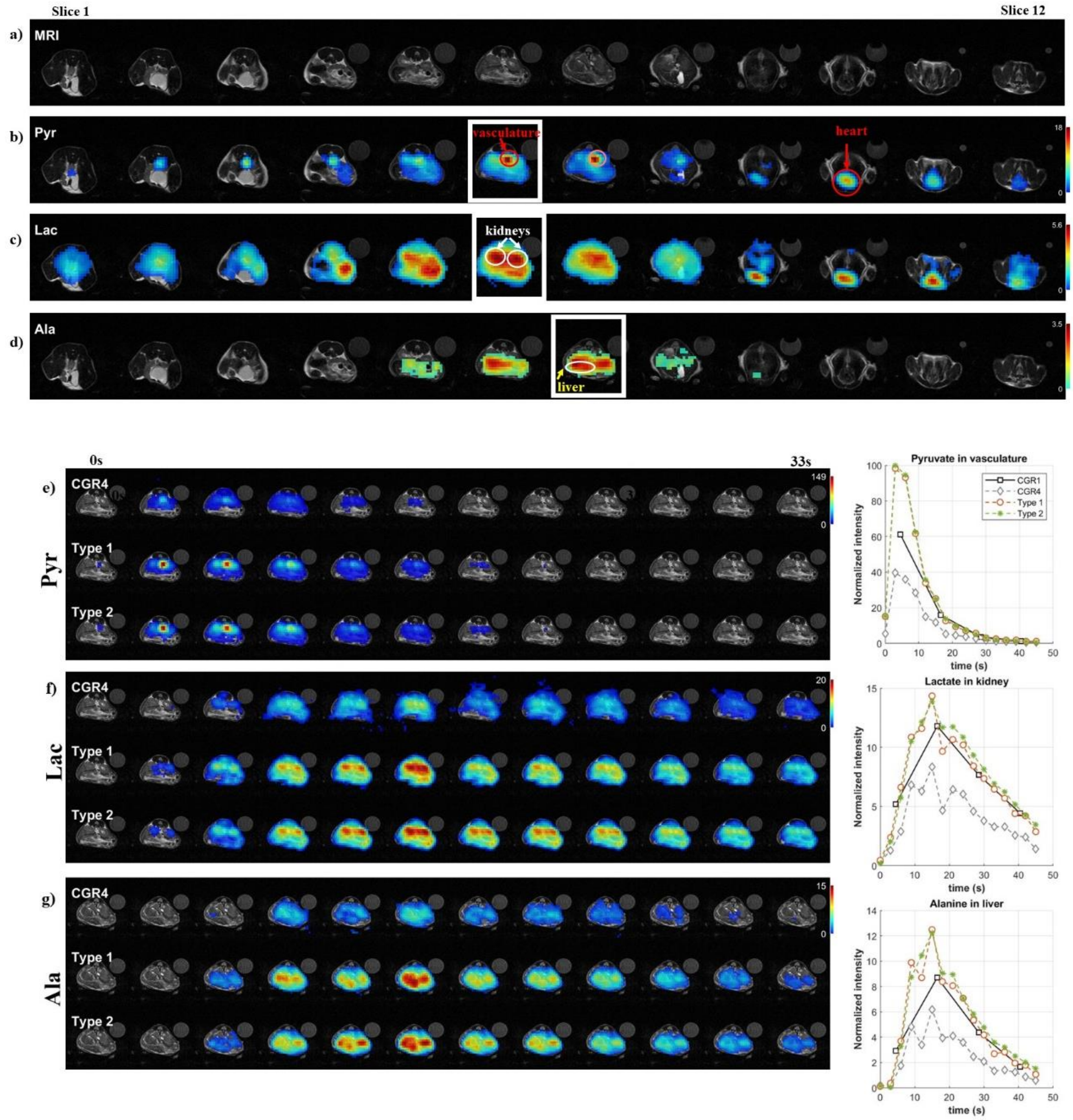

Figure 7-6, data for mouse m4. **(b-d)** Time-averaged metabolic maps **(e-g)** accelerated images.

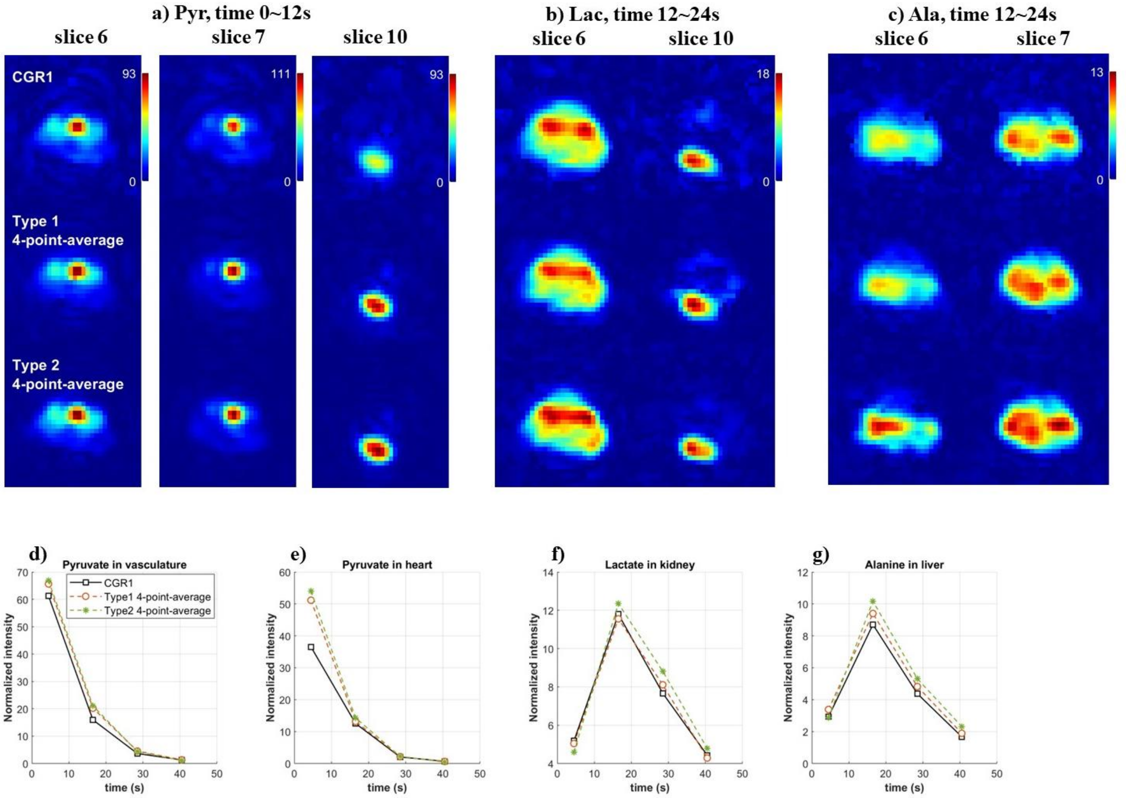

Figure 7-7, Non-accelerated images for m4.

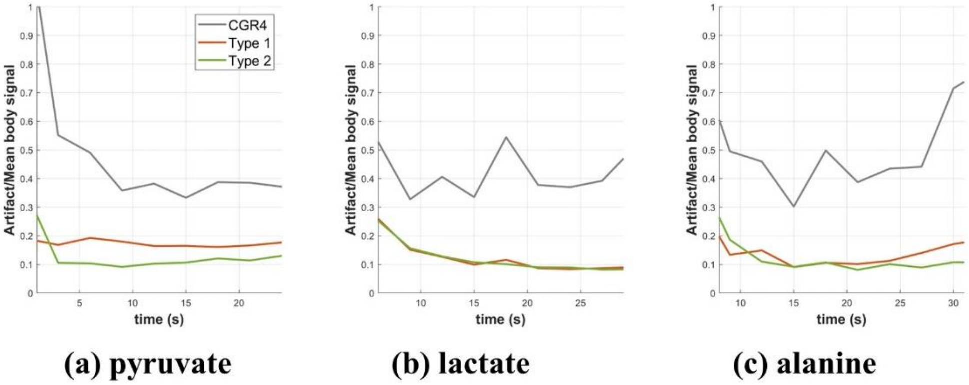

(a) pyruvate (b) lactate (c) alanine

Figure 7-8, Artifact-to-mean body signal ratio for m4

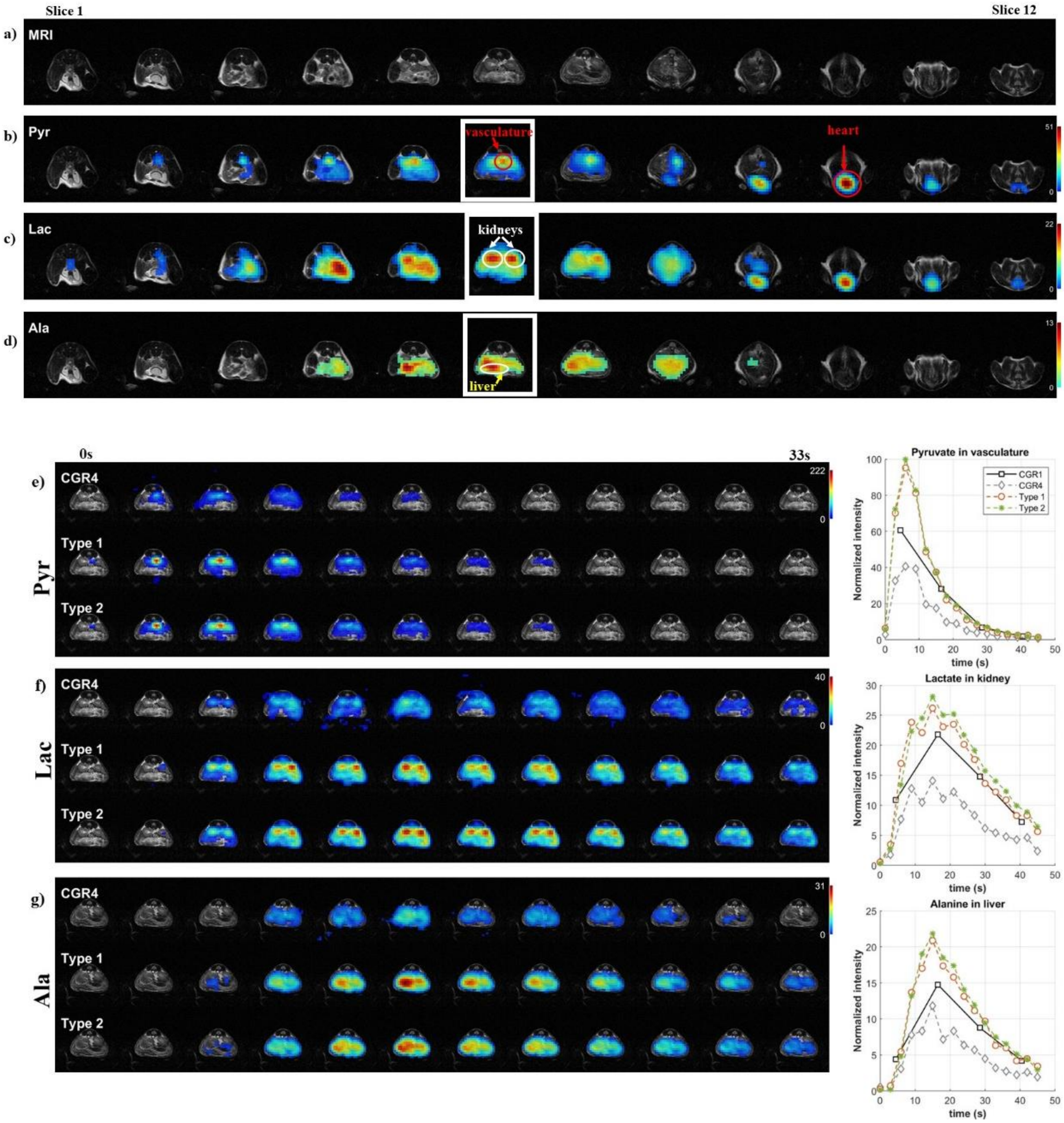

Figure 7-9, data for mouse m5. **(b-d)** Time-averaged metabolic maps **(e-g)** accelerated images.

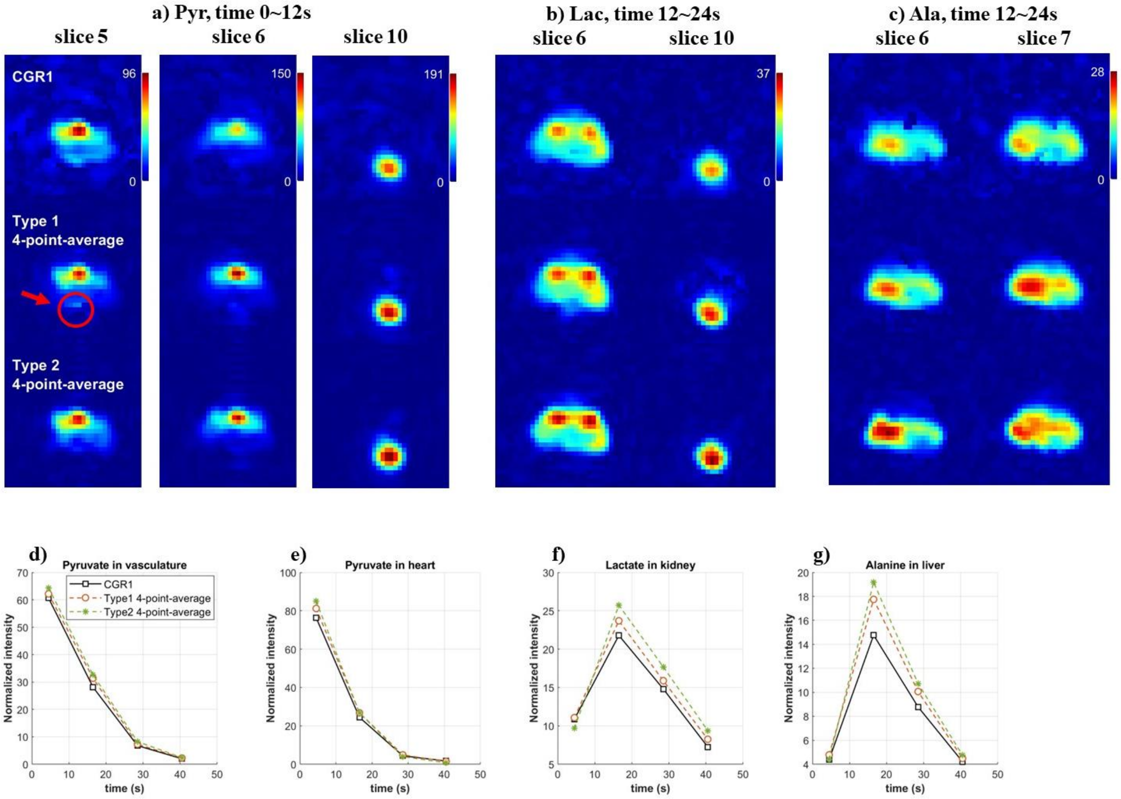

Figure 7-10 Non-accelerated images for m5.

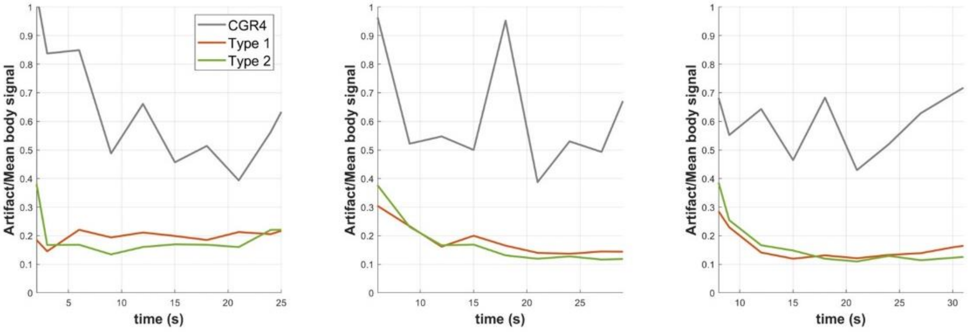

(a) pyruvate (b) lactate (c) alanine

Figure 7-11 Artifact-to-mean body signal ratio for m5

7. 3 Effect of different choice of the threshold parameters

The choice of the soft thresholding parameters (λ_L, λ_S and λ_{Si}) is based on the effectiveness in reduction of the image artifacts and consistency between the reconstructed image and the acquired k-space. In general, a smaller λ_L or λ_S will have slower updates for each iteration, less effective in reducing the artifacts from M_0. On the other hand, a larger λ_L or λ_S will enforce stronger low-rankness/sparsity along the dynamic frames but sacrificing a portion of the data consistency. A proper choice of the threshold parameters should balance the trade-off between artifacts reduction and data consistency.

Simulation with the digital 2D spectroscopic imaging phantom described in section 4.2.3. was conducted with different values of λ_L or λ_S using LLS reconstruction running for 50 iterations for each parameter combination. In each case, λ_{S_i} was set to the same value as λ_S. For each choice of λ_L and λ_S, performance of the reconstruction was evaluated with nRMSE of the reconstructed image after each iteration to monitor speed of convergence, plotted in Figure 7-12. Artifact-to-mean body signal ratio was measured by taking the mean intensity of the artifacts outside the body area (4 discs), normalized to the mean intensity inside the body area. For each choice of the parameter, ASR of the reconstructed image for each metabolite is calculated after each iteration and plotted in Figure 7-13. The residual image, $M_{res} = E' * (d_n - d_0)$, reflects the difference between the reconstructed and acquired k-space at iteration n. For each choice of the parameter, the root mean square of the residual image for the three metabolites after each iteration was normalized to the root mean square of the ground truth image, plotted in Figure 7-14. Reconstructed image after 50 iterations with respective parameter is shown in Figure 7-15. For the given 5 combinations, the combination used in section 4.2.3. is considered optimal in terms of differences from ground truth and artifact reduction overall.

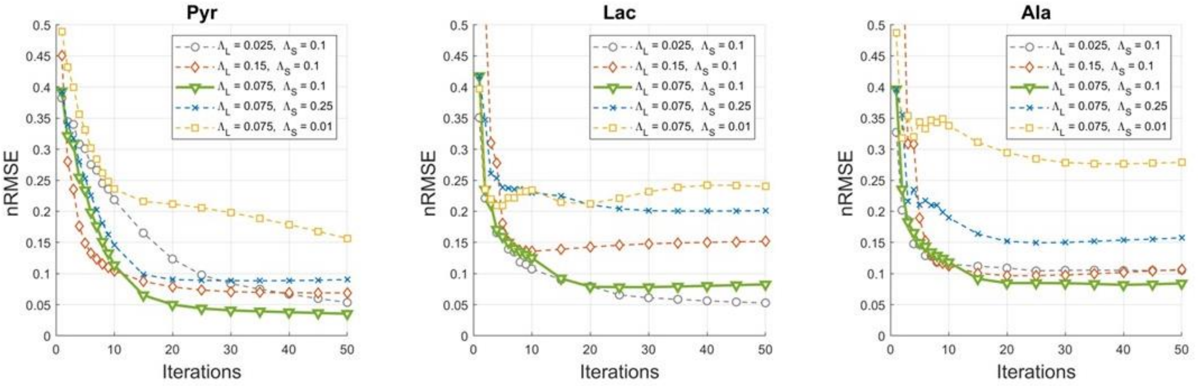

Figure 7-12 nRMSE versus number of iterations for the digital simulation of the 2D phantom using different choice of the threshold parameters. The green line indicates the results using the threshold parameters presented in section 4.2.3.

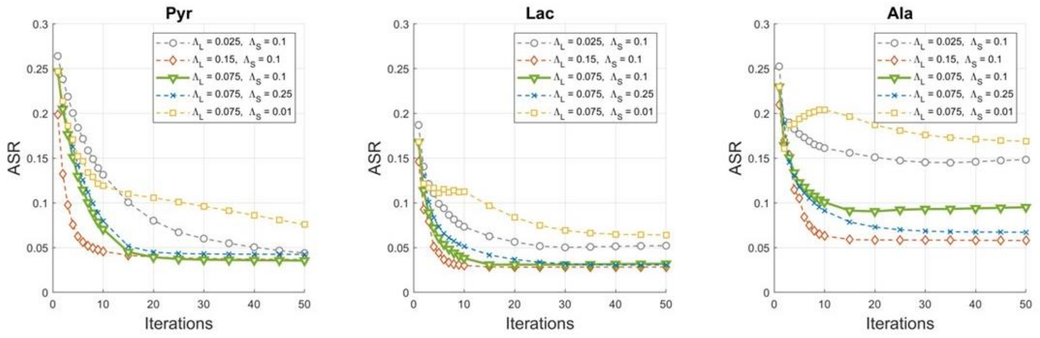

(a) **(b)** **(c)**

Figure 7-13 Artifact-to-mean body signal ratio versus number of iterations for the 2D simulation using different choice of the threshold parameters. The green line indicates the results using the threshold parameters presented in section 4.2.3.

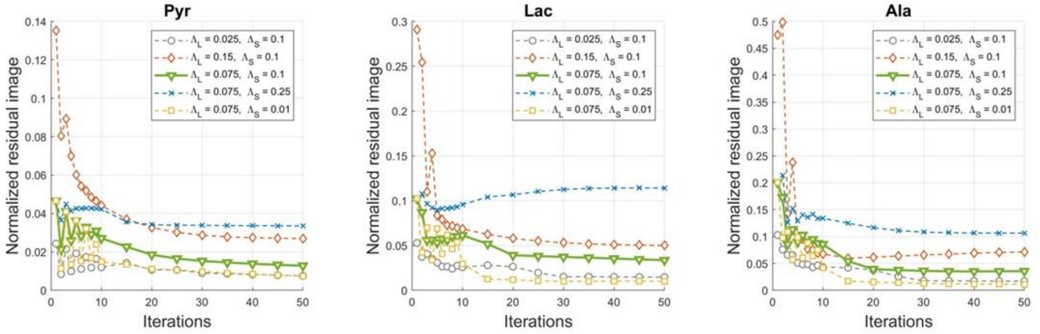

(a) **(b)** **(c)**

Figure 7-14 Normalized residual image versus number of iterations for the 2D simulation using different choice of the threshold parameters. The green line indicates the results using the threshold parameters presented in section 4.2.3.

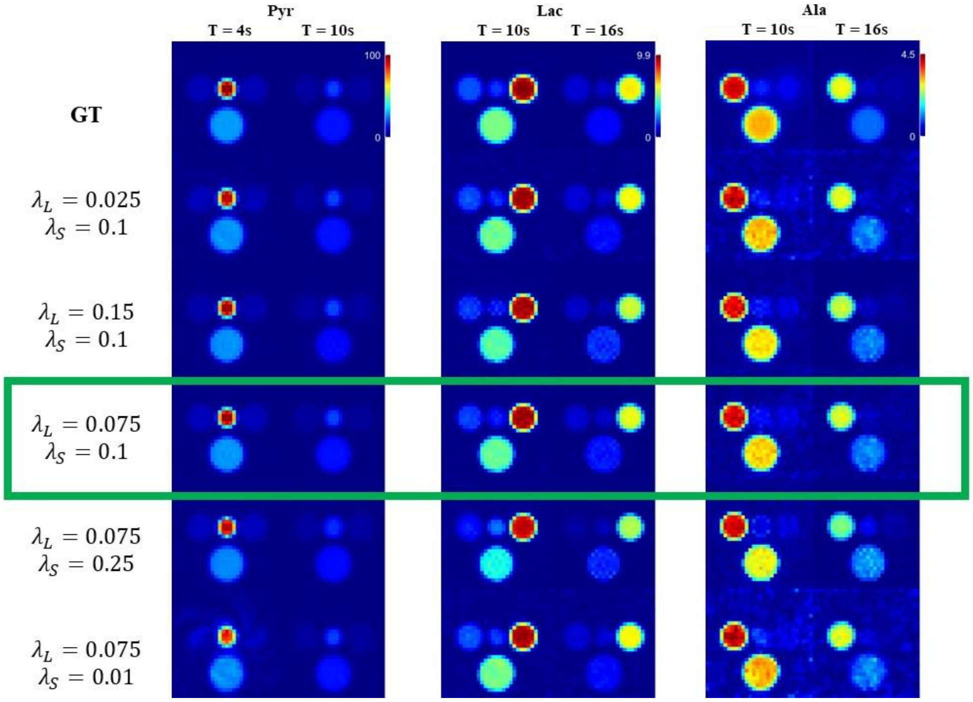

Figure 7-15 Reconstructed images at selected time points for the digital simulation of the 2D phantom using different choice of the threshold parameters at iteration 50. Images in the first row represent the ground truth. Images in the green rectangle represent the results using the threshold parameters presented in section 4.3.1

Reconstruction of the in vivo 2D imaging data described in section 4.3.2 (1st 2D imaging dataset) was conducted with three different values of λ_S $(0.025, 0.25$ and $0.5)$ using LLS reconstruction running 21 iterations each. Accelerated images are displayed in Figure 7-16 and non-accelerated images are displayed in Figure 7-17. ASR of the reconstruction results after each iteration is plotted in Figure 7-18, and normalized residual image after each iteration is plotted in Figure 7-19. Results using the choice of $\lambda_S = 0.25$ (value used in section 4.3.2.) are presented in the 3rd row for each image series, with all measurements plotted with the green line. Similar to the effects seen in simulation, reconstruction results with small λ_S have more artifacts outside the body area, while results with large λ_S have higher residual image intensity due to inconsistencies between reconstructed and measured data.

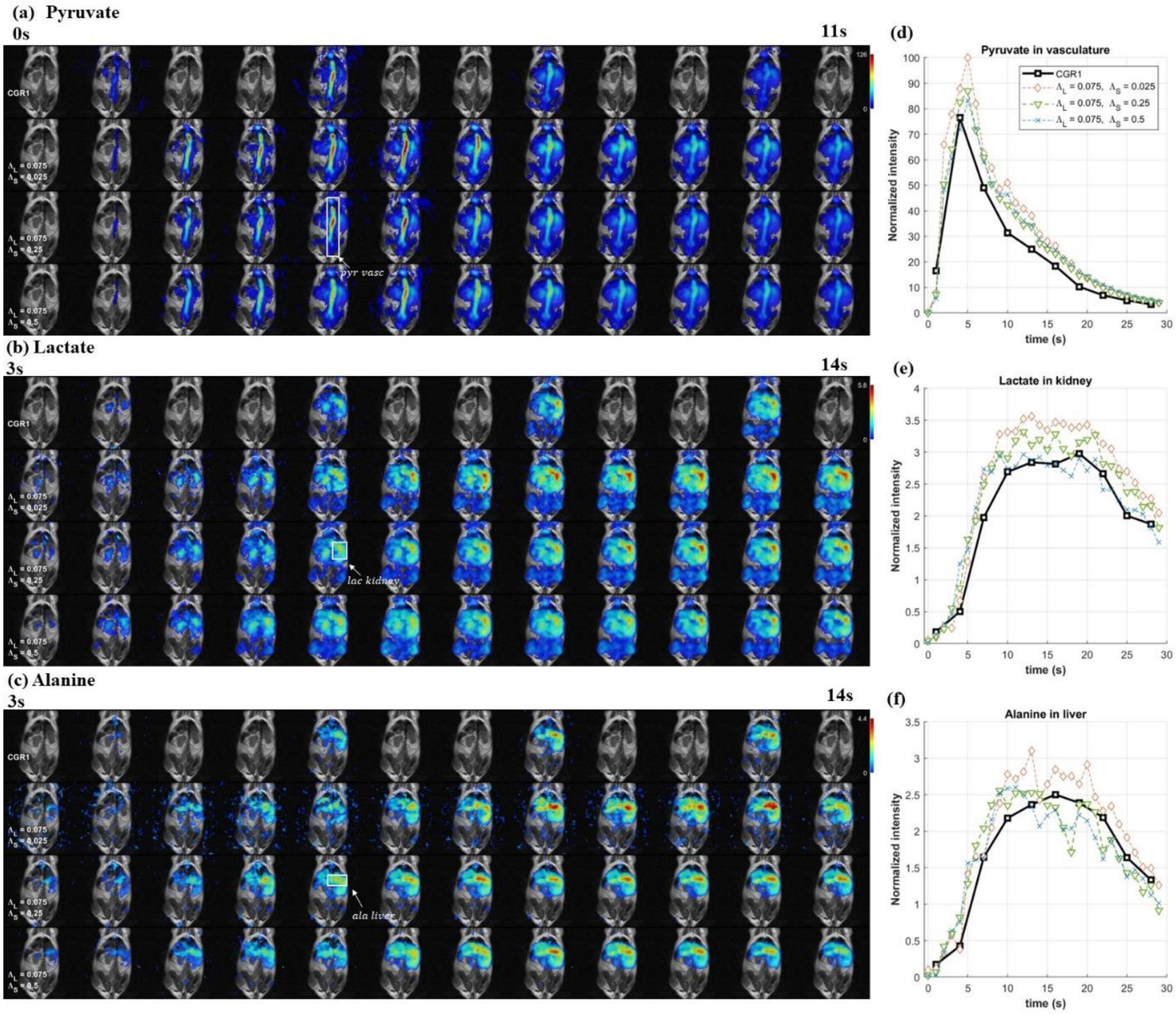

Figure 7-16 Dynamic images of the 2D in vivo imaging data reconstructed with LLS using $\lambda_L = 0.075, \lambda_S = 0.025, 0.25$ (choice in section 4.3.2.) and 0.5. CGR1 represents reference image reconstructed from fully sampled k-space **(a)** Pyruvate dynamic images starting at 0 second after the start of data acquisition. **(b)** Lactate dynamic images starting at 3 seconds after the start of data acquisition. **(c)** Alanine dynamic images starting at 3 seconds after the start of data acquisition. **(d-f)** Dynamic curves for the mean intensity in the ROI indicated by the white rectangle of each metabolite for each reconstruction.

(a) Pyruvate

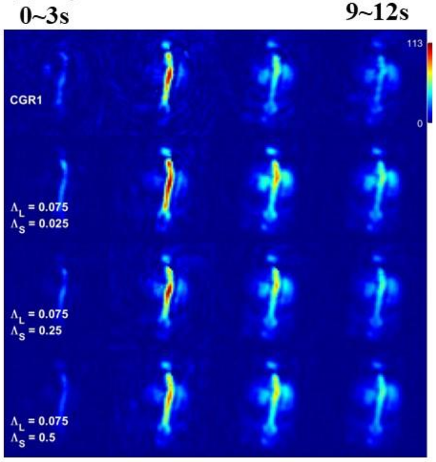

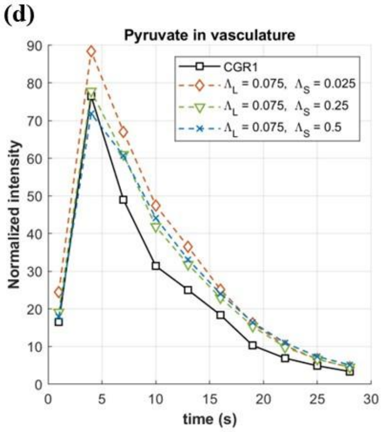

(b) Lactate

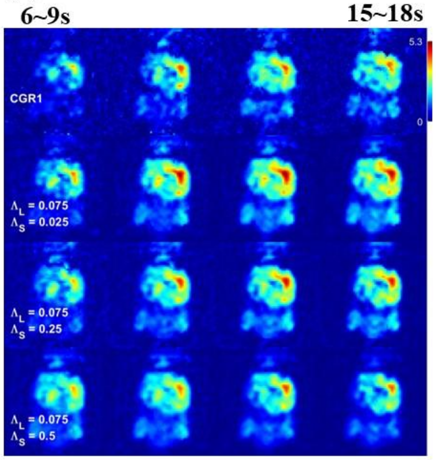

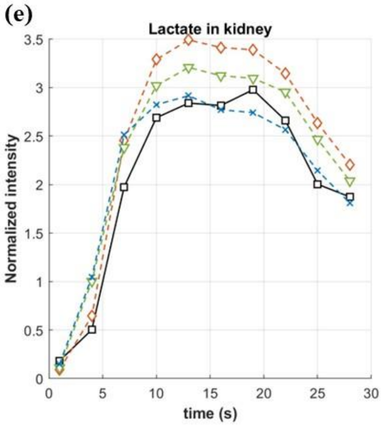

(c) Alanine

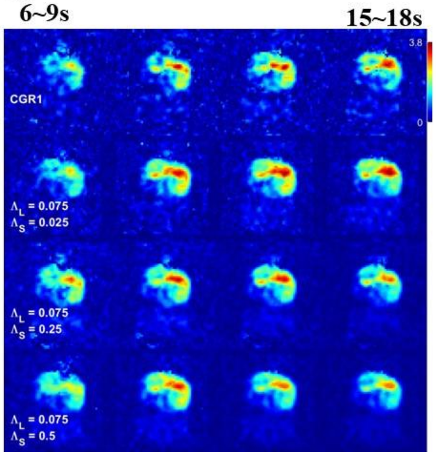

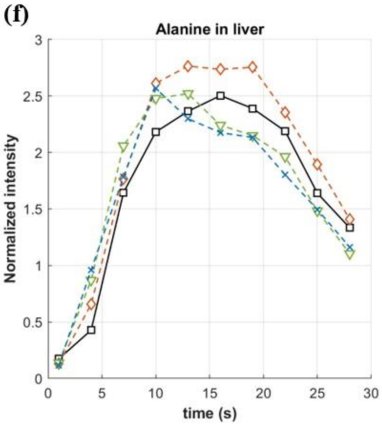

Figure 7-17, Dynamic images reconstructed at 3 seconds temporal resolution for CGR1 and 3-time point-average of the LLS reconstruction with respective choice of λ_S. **(d-f)** Dynamic curves for the mean intensity in the ROI.

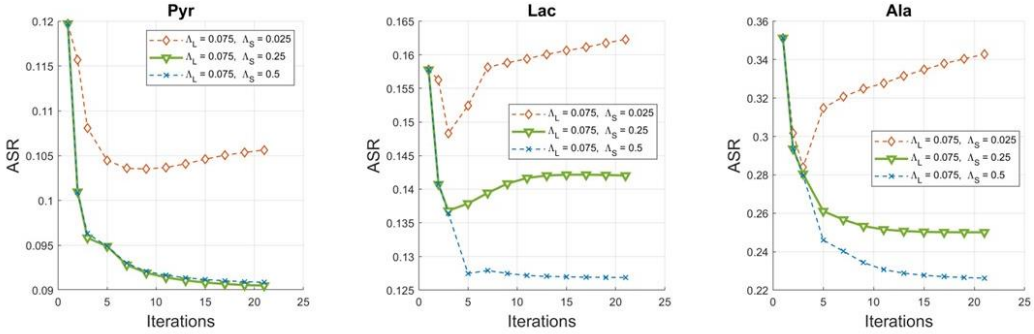

(a) **(b)** **(c)**

Figure 7-18 Artifact-to-mean body signal ratio versus number of iterations for the in vivo imaging data using different choice of the threshold parameters. The green line indicates the results using the threshold parameters presented in section 4.3.2.

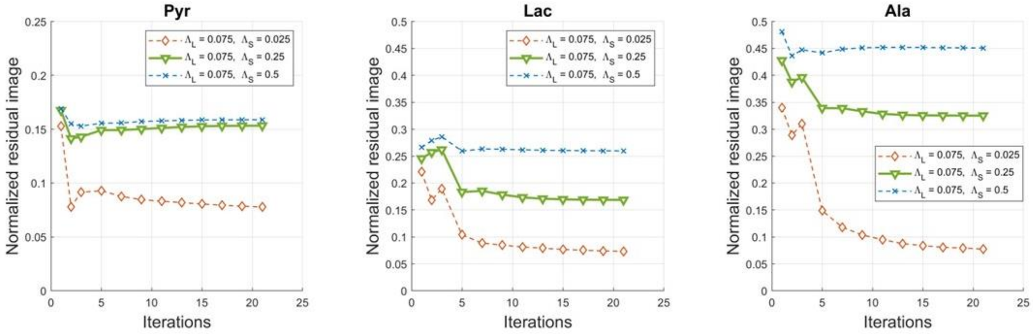

(a) **(b)** **(c)**

Figure 7-19 Normalized residual image versus number of iterations for the in vivo imaging data using different choice of the threshold parameters. The green line indicates the results using the threshold parameters presented in section 4.3.2.

Chapter 8 : Summary and future work

This dissertation focused on developing iterative reconstruction methods to improve the image quality of hyperpolarized ^{13}C MRI. It consists of both verification of the algorithm through simulation and evaluation of the results from in vivo imaging experiments.

In Chapter 3, a model-based reconstruction method was developed to utilize the prior knowledge for quantification of the metabolites. Application of the model-based reconstruction on in vivo data reduced the artifacts caused by a partially overlapped peak. In Chapter 4, a low rank plus local sparse reconstruction method was developed to accurately restore the dynamic images for low intensity metabolites from under-sampled data acquisitions. The method effectively accelerated in vivo 2D spectroscopic ^{13}C imaging by a factor of 3. In Chapter 5, the low rank plus local sparse reconstruction was extended for 3D spectroscopic imaging with proper adaptations and achieved effective 4-fold acceleration. In Chapter 6, hyperpolarized ^{13}C imaging with flow-sensitizing gradients were performed on healthy rats to investigate the origin of the ^{13}C lactate signal in brain after injection of [1-^{13}C]pyruvate. Analysis of the results supported our hypothesis that lactate observed in the brain was predominantly from the metabolic conversion of pyruvate in the brain, not the product from other organs. Chapter 7 provided additional data for chapter 4 and chapter 5, as well as addressing the effects of different choice of the threshold parameters in the low rank plus local sparse reconstruction algorithm.

Future work for the model-based reconstruction may include incorporating additional prior knowledge and regularization terms to further constrain the reconstruction results. For the low rank plus sparse reconstruction, directions for improvement include exploring local sparsity in other dimensions with variable block sizes, utilization of other forms of the NDFT operator for computing efficiency and adapting non-equidistant sampling along spectral dimension.

Bibliography

1. Golman K, Ardenkjaer-Larsen JH, Petersson JS, Mansson S, Leunbach I. Molecular imaging with endogenous substances. *Proceedings of the National Academy of Sciences*. 2003;100(18):10435-10439. doi:10.1073/pnas.1733836100

2. Ardenkjaer-Larsen JH, Fridlund B, Gram A, et al. Increase in signal-to-noise ratio of > 10,000 times in liquid-state NMR. *Proceedings of the National Academy of Sciences*. 2003;100(18):10158-10163. doi:10.1073/pnas.1733835100

3. Kurhanewicz J, Vigneron DB, Brindle K, et al. Analysis of Cancer Metabolism by Imaging Hyperpolarized Nuclei: Prospects for Translation to Clinical Research. *Neoplasia*. 2011;13(2):81-97. doi:10.1593/neo.101102

4. Kurhanewicz J, Vigneron DB, Ardenkjaer-Larsen JH, et al. Hyperpolarized 13C MRI: Path to Clinical Translation in Oncology. *Neoplasia*. 2019;21(1):1-16. doi:10.1016/j.neo.2018.09.006

5. Hurd RE, Yen YF, Chen A, Ardenkjaer-Larsen JH. Hyperpolarized 13C metabolic imaging using dissolution dynamic nuclear polarization. *Journal of Magnetic Resonance Imaging*. 2012;36(6):1314-1328. doi:https://doi.org/10.1002/jmri.23753

6. Nishimura DG. *Principles of Magnetic Resonance Imaging*. Stanford University; 2010.

7. Schröder L, Faber C, eds. *In Vivo NMR Imaging: Methods and Protocols*. Vol 771. Humana Press; 2011. doi:10.1007/978-1-61779-219-9

8. Hu S, Larson PEZ, VanCriekinge M, et al. Rapid sequential injections of hyperpolarized [1-13C]pyruvate in vivo using a sub-kelvin, multi-sample DNP polarizer. *Magnetic Resonance Imaging*. 2013;31(4):490-496. doi:10.1016/j.mri.2012.09.002

9. Golman K, Petersson JS. Metabolic Imaging and Other Applications of Hyperpolarized 13C1. *Academic Radiology*. 2006;13(8):932-942. doi:10.1016/j.acra.2006.06.001

10. Uecker M. Nonlinear Reconstruction Methods for Parallel Magnetic Resonance Imaging.

11. Fessler JA. On NUFFT-based gridding for non-Cartesian MRI. *Journal of Magnetic Resonance*. 2007;188(2):191-195. doi:10.1016/j.jmr.2007.06.012

12. Fessler JA, Sutton BP. Nonuniform fast Fourier transforms using min-max interpolation. *IEEE Transactions on Signal Processing*. 2003;51(2):560-574. doi:10.1109/TSP.2002.807005

13. Jackson JI, Meyer CH, Nishimura DG, Macovski A. Selection of a convolution function for Fourier inversion using gridding (computerised tomography application). *IEEE Transactions on Medical Imaging*. 1991;10(3):473-478. doi:10.1109/42.97598

14. Lasdon L, Mitter S, Waren A. The conjugate gradient method for optimal control problems. *IEEE Transactions on Automatic Control*. 1967;12(2):132-138. doi:10.1109/TAC.1967.1098538

15. Sweedler JV, Lutz NW, Wevers RA, eds. Metabolomic Nuclear Magnetic Resonance Spectroscopy Techniques for Body Tissue Analysis. In: *Methodologies for Metabolomics: Experimental Strategies and Techniques*. Cambridge University Press; 2013:333-584.

16. Maudsley AA, Hilal SK, Perman WH, Simon HE. Spatially resolved high resolution spectroscopy by “four-dimensional” NMR. *Journal of Magnetic Resonance (1969)*. 1983;51(1):147-152. doi:10.1016/0022-2364(83)90113-0

17. Brown TR, Kincaid BM, Ugurbil K. NMR chemical shift imaging in three dimensions. *PNAS*. 1982;79(11):3523-3526. doi:10.1073/pnas.79.11.3523

18. Adalsteinsson E, Irarrazabal P, Topp S, Meyer C, Macovski A, Spielman DM. Volumetric spectroscopic imaging with spiral-based k-space trajectories. *Magnetic Resonance in Medicine*. 1998;39(6):889-898. doi:10.1002/mrm.1910390606

19. Mayer D, Yen YF, Levin YS, et al. In vivo application of sub-second spiral chemical shift imaging (CSI) to hyperpolarized 13C metabolic imaging: Comparison with phase-encoded CSI. *Journal of Magnetic Resonance*. 2010;204(2):340-345. doi:10.1016/j.jmr.2010.03.005

20. Mayer D, Levin YS, Hurd RE, Glover GH, Spielman DM. Fast metabolic imaging of systems with sparse spectra: Application for hyperpolarized 13C imaging. *Magnetic Resonance in Medicine*. 2006;56(4):932-937. doi:https://doi.org/10.1002/mrm.21025

21. Hurd RE, Chen AP. Sampling Strategies in Dynamic Hyperpolarized NMR. In: *Dynamic Hyperpolarized Nuclear Magnetic Resonance*. Handbook of Modern Biophysics. Springer International Publishing; 2021:77-102. doi:10.1007/978-3-030-55043-1_4

22. Warburg O. On the Origin of Cancer Cells. *Science*. 1956;123(3191):309-314.

23. Heiden MGV, Cantley LC, Thompson CB. Understanding the Warburg Effect: The Metabolic Requirements of Cell Proliferation. *Science*. 2009;324(5930):1029-1033. doi:10.1126/science.1160809

24. Nelson SJ, Kurhanewicz J, Vigneron DB, et al. Metabolic Imaging of Patients with Prostate Cancer Using Hyperpolarized [1-13C]Pyruvate. *Science Translational Medicine*. 2013;5(198):198ra108-198ra108. doi:10.1126/scitranslmed.3006070

25. Mayer D, Yen YF, Takahashi A, et al. Dynamic and high-resolution metabolic imaging of hyperpolarized [1-13C]-pyruvate in the rat brain using a high-performance gradient insert. *Magnetic Resonance in Medicine*. 2011;65(5):1228-1233. doi:10.1002/mrm.22707

26. Fessler JA. Model-Based Image Reconstruction for MRI. *IEEE Signal Processing Magazine*. 2010;27(4):81-89. doi:10.1109/MSP.2010.936726

27. Zhu M, Mayer D. Improving Hyperpolarized 13C Spiral Chemical Shift Imaging Using Model-Based Iterative Reconstruction and Prior Knowledge. In: *Proc. Intl. Soc. Mag. Reson. Med. 27 (2019)*. ; 2019. https://index.mirasmart.com/ISMRM2019/PDFfiles/4294.html

28. Lustig M, Donoho D, Pauly JM. Sparse MRI: The application of compressed sensing for rapid MR imaging. *Magnetic Resonance in Medicine*. 2007;58(6):1182-1195. doi:10.1002/mrm.21391

29. Otazo R, Candès E, Sodickson DK. Low-rank and Sparse Matrix Decomposition for Accelerated Dynamic MRI with Separation of Background and Dynamic Components. *Magn Reson Med*. 2015;73(3):1125-1136. doi:10.1002/mrm.25240

30. DeVience SJ, Mayer D. Speeding up dynamic spiral chemical shift imaging with incoherent sampling and low-rank matrix completion. *Magnetic Resonance in Medicine*. 2017;77(3):951-960. doi:https://doi.org/10.1002/mrm.26170

31. Milshteyn E, von Morze C, Reed GD, et al. Using a local low rank plus sparse reconstruction to accelerate dynamic hyperpolarized 13C imaging using the bSSFP sequence. *Journal of Magnetic Resonance*. 2018;290:46-59. doi:10.1016/j.jmr.2018.03.006

32. Lin CY, Fessler JA. Efficient Dynamic Parallel MRI Reconstruction for the Low-Rank Plus Sparse Model. *IEEE TRANSACTIONS ON COMPUTATIONAL IMAGING*. 2019;5(1).

33. Hu S, Lustig M, Balakrishnan A, et al. 3D compressed sensing for highly accelerated hyperpolarized 13C MRSI with in vivo applications to transgenic mouse models of cancer. *Magnetic Resonance in Medicine*. 2010;63(2):312-321. doi:10.1002/mrm.22233

34. Josan S, Spielman D, Yen YF, Hurd R, Pfefferbaum A, Mayer D. Fast volumetric imaging of ethanol metabolism in rat liver with hyperpolarized [1-13C]pyruvate. *NMR in Biomedicine*. 2012;25(8):993-999. doi:10.1002/nbm.2762

35. Larson PEZ, Kerr AB, Chen AP, et al. Multiband excitation pulses for hyperpolarized 13C dynamic chemical-shift imaging. *Journal of Magnetic Resonance*. 2008;194(1):121-127. doi:10.1016/j.jmr.2008.06.010

36. Hurd RE, Yen YF, Mayer D, et al. Metabolic imaging in the anesthetized rat brain using hyperpolarized [1-13C] pyruvate and [1-13C] ethyl pyruvate. *Magnetic Resonance in Medicine*. 2010;63(5):1137-1143. doi:10.1002/mrm.22364

37. Hurd RE, Yen YF, Tropp J, Pfefferbaum A, Spielman DM, Mayer D. Cerebral Dynamics and Metabolism of Hyperpolarized [1-13C]pyruvate Using Time-Resolved MR Spectroscopic Imaging. *J Cereb Blood Flow Metab*. 2010;30(10):1734-1741. doi:10.1038/jcbfm.2010.93

38. Park JM, Josan S, Grafendorfer T, et al. Measuring mitochondrial metabolism in rat brain in vivo using MR Spectroscopy of hyperpolarized [2-13C]pyruvate. *NMR in Biomedicine*. 2013;26(10):1197-1203. doi:10.1002/nbm.2935

39. Marjańska M, Iltis I, Shestov AA, et al. In vivo 13C spectroscopy in the rat brain using hyperpolarized [1-13C]pyruvate and [2-13C]pyruvate. *Journal of Magnetic Resonance*. 2010;206(2):210-218. doi:10.1016/j.jmr.2010.07.006

40. Park I, Larson PEZ, Zierhut ML, et al. Hyperpolarized 13C magnetic resonance metabolic imaging: application to brain tumors. *Neuro-Oncology*. 2010;12(2):133-144. doi:10.1093/neuonc/nop043

41. Day SE, Kettunen MI, Cherukuri MK, et al. Detecting response of rat C6 glioma tumors to radiotherapy using hyperpolarized [1-13C]pyruvate and 13C magnetic resonance spectroscopic imaging. *Magnetic Resonance in Medicine*. 2011;65(2):557-563. doi:10.1002/mrm.22698

42. Park JM, Josan S, Jang T, et al. Metabolite kinetics in C6 rat glioma model using magnetic resonance spectroscopic imaging of hyperpolarized [1-13C]pyruvate. *Magnetic Resonance in Medicine*. 2012;68(6):1886-1893. doi:10.1002/mrm.24181

43. Chaumeil MM, Ozawa T, Park I, et al. Hyperpolarized 13C MR spectroscopic imaging can be used to monitor Everolimus treatment in vivo in an orthotopic rodent model of glioblastoma. *NeuroImage*. 2012;59(1):193-201. doi:10.1016/j.neuroimage.2011.07.034

44. Park JM, Recht LD, Josan S, et al. Metabolic response of glioma to dichloroacetate measured in vivo by hyperpolarized 13C magnetic resonance spectroscopic imaging. *Neuro-Oncology*. 2013;15(4):433-441. doi:10.1093/neuonc/nos319

45. Park JM, Spielman DM, Josan S, et al. Hyperpolarized 13C-lactate to 13C-bicarbonate ratio as a biomarker for monitoring the acute response of anti-vascular endothelial growth factor (anti-VEGF) treatment. *NMR in Biomedicine*. 2016;29(5):650-659. doi:10.1002/nbm.3509

46. Guglielmetti C, Chou A, Krukowski K, et al. In vivo metabolic imaging of Traumatic Brain Injury. *Sci Rep*. 2017;7(1):17525. doi:10.1038/s41598-017-17758-4

47. DeVience SJ, Lu X, Proctor J, et al. Metabolic imaging of energy metabolism in traumatic brain injury using hyperpolarized [1-13C]pyruvate. *Sci Rep*. 2017;7(1):1907. doi:10.1038/s41598-017-01736-x

48. Le Page LM, Guglielmetti C, Najac CF, Tiret B, Chaumeil MM. Hyperpolarized 13C magnetic resonance spectroscopy detects toxin-induced neuroinflammation in mice. *NMR in Biomedicine*. 2019;32(11):e4164. doi:10.1002/nbm.4164

49. Miller JJ, Grist JT, Serres S, et al. 13C Pyruvate Transport Across the Blood-Brain Barrier in Preclinical Hyperpolarised MRI. *Sci Rep*. 2018;8(1):15082. doi:10.1038/s41598-018-33363-5

50. Ye FQ, Mattay VS, Jezzard P, Frank JA, Weinberger DR, McLaughlin AC. Correction for vascular artifacts in cerebral blood flow values measured by using arterial spin tagging techniques. *Magnetic Resonance in Medicine*. 1997;37(2):226-235. doi:10.1002/mrm.1910370215

51. Pell GS, Lewis DP, Branch CA. Pulsed arterial spin labeling using TurboFLASH with suppression of intravascular signal. *Magnetic Resonance in Medicine*. 2003;49(2):341-350. doi:10.1002/mrm.10373

52. Gordon JW, Niles DJ, Adamson EB, Johnson KM, Fain SB. Application of flow sensitive gradients for improved measures of metabolism using hyperpolarized 13c MRI. *Magnetic Resonance in Medicine*. 2016;75(3):1242-1248. doi:https://doi.org/10.1002/mrm.25584

53. Lau AZ, Miller JJ, Robson MD, Tyler DJ. Cardiac perfusion imaging using hyperpolarized 13c urea using flow sensitizing gradients. *Magnetic Resonance in Medicine*. 2016;75(4):1474-1483. doi:https://doi.org/10.1002/mrm.25713

54. Lee H, Lee J, Joe E, et al. Flow-suppressed hyperpolarized 13C chemical shift imaging using velocity-optimized bipolar gradient in mouse liver tumors at 9.4 T. *Magnetic Resonance in Medicine*. 2017;78(5):1674-1682. doi:https://doi.org/10.1002/mrm.26578

55. Mayer D, Yen YF, Tropp J, Pfefferbaum A, Hurd RE, Spielman DM. Application of subsecond spiral chemical shift imaging to real-time multislice metabolic imaging of the rat in vivo after injection of hyperpolarized 13C1-pyruvate. *Magnetic Resonance in Medicine*. 2009;62(3):557-564. doi:10.1002/mrm.22041

56. Lapergue B, Deroide N, Pocard M, Michel JB, Meilhac O, Bonnin P. Transcranial duplex sonography for monitoring circle of Willis artery occlusion in a rat embolic stroke model. *Journal of Neuroscience Methods*. 2011;197(2):289-296. doi:10.1016/j.jneumeth.2011.02.016

57. Larkin JR, Simard MA, Khrapitchev AA, et al. Quantitative blood flow measurement in rat brain with multiphase arterial spin labelling magnetic resonance imaging. *J Cereb Blood Flow Metab*. 2019;39(8):1557-1569. doi:10.1177/0271678X18756218

58. Wang Y, Zhang T, Zhang Y, et al. Effects of inverted photoperiods on the blood pressure and carotid artery of spontaneously hypertensive rats and Wistar–Kyoto rats. *Journal of Hypertension*. 2021;39(5):871-879. doi:10.1097/HJH.0000000000002732

59. Ivanov KP, Kalinina MK, Levkovich YuI. Blood flow velocity in capillaries of brain and muscles and its physiological significance. *Microvascular Research*. 1981;22(2):143-155. doi:10.1016/0026-2862(81)90084-4

60. Seylaz J, Charbonné R, Nanri K, et al. Dynamic In Vivo Measurement of Erythrocyte Velocity and Flow in Capillaries and of Microvessel Diameter in the Rat Brain by Confocal Laser Microscopy. *J Cereb Blood Flow Metab*. 1999;19(8):863-870. doi:10.1097/00004647-199908000-00005